A Provably Stable and High-Order Accurate Finite Difference Approximation for the Incompressible Boundary Layer Equations

Presented by

Mojalefa Prince Nchupang

Under the supervision of

Prof. Arnaud G. Malan
Department of Mechanical Engineering
University of Cape Town, *South Africa*

Prof. Jan Nordström
Department of Mathematics, Applied Mathematics
Linköping University, *Sweden*
Department of Mathematics and Applied Mathematics
University of Johannesburg, *South Africa*

A thesis submitted to the University of Cape Town in fulfillment of the requirements for the degree of Doctor of Philosophy in Mechanical Engineering

12 February 2024

Declaration of authorship

I, Mojalefa Prince Nchupang, declare that this dissertation titled 'A provably stable and high-order accurate finite difference approximation for the incompressible boundary layer equations' and the work presented in it are my own. I can confirm that:

- This work was done wholly or mainly while in candidature for a doctoral degree at the University of Cape Town (UCT);
- Where any part of this dissertation has previously been submitted for a degree or any other academic qualification at UCT or any other institution, this has been clearly stated;
- Where I have consulted the published work of others, this is always clearly attributed;
- Where I have quoted from the work of others, the source is always given. With the exception of such quotations, this dissertation is entirely my own work;
- I have acknowledged all main sources of help;

Signed: .....

Date: .....

Abstract

A Provably Stable and High-Order Accurate Finite Difference Approximation for the Incompressible Boundary Layer Equations

Mojalefa Prince Nchupang

In recent years, there has been considerable interest in numerical simulations of incompressible flows due to their numerous industrial applications. These include weather forecasting, modeling blood circulation, and analysing airflow around vehicles. Traditional second order numerical schemes have been widely used to analyse and predict flow parameters such as velocities and pressure. However, these second order accurate approaches numerically damp flow vortexes while requiring excessive element numbers in the boundary layers. Further, mainstream incompressible flow solution schemes augment the incompressible mass conservation equation to avoid the resulting singular coefficient matrix.

The two main augmentation approaches are the so-called pressure-based (projection scheme) and density-based (artificial compressibility) methods. These approaches introduce the need for more boundary conditions which place additional constraints on pressure gradients at boundaries. Finally, the ubiquitous practice of upwinding convective terms when solving incompressible flows adds both complexity and non-physical dissipation to the flow solution. The key contributions of this study address these concerns. For this purpose we employ the celebrated incompressible boundary layer equations as a model problem and endeavour to prove the existence of a stable and high order accurate solution without any need for additional augmented pressure/density based equations and without the use of upwinding.

We develop a high order accurate method to solve the incompressible boundary layer equations in a provably stable manner. We will derive continuous energy estimates, and then we will proceed to the discrete setting. We formulate the discrete approximation using high-order finite difference methods on summation-by-parts form and implement the boundary conditions weakly using the simultaneous approximation term method. By applying the discrete energy method and imitating the continuous analysis, the discrete estimate that resembles the continuous counterpart is obtained thus proving stability. We also show that these newly derived boundary conditions remove the singularities associated with the nullspace of the nonlinear discrete spatial operator. Numerical experiments that verify the high-order accuracy of the scheme and coincide with the theoretical results are presented. The numerical results are compared with the well-known Blasius similarity solution, as well as that resulting from the solution of the incompressible Navier-Stokes equations.

Acknowledgment

This work is the epitome of resilience, determination, and hard work. I would like to express my sincere gratitude to my supervisors, Prof. Arnaud Malan and Prof. Jan Nordström, for their guidance, unwavering support, and encouragements during this journey. I can confidently say that this work would not have been possible without their invaluable advice and constructive feedback. I am grateful to Prof. Malan for financial and administrative support.

I would also like to extend my heartfelt gratitude to Dr. Fredrik Laurén for his kindness and willingness to help with coding and providing editorial support.

I had the privilege to call the InCFD group home for the past six years. I would like to thank my colleagues, both past and present, for the fruitful discussions and conversations during tea time and occasional outings.

Lastly, to my dearest family and friends, I appreciate your continuous support, unending love, and prayers. To God be the Glory. Ke a leboga!

Funding statement

This work is based on research supported by the National Research Foundation of South Africa (Grant Numbers: 89916). The opinions, findings and conclusions or recommendations expressed are that of the authors alone, and the NRF accepts no liability whatsoever in this regard. The research leading to these results has also received funding from the European Union's Horizon 2020 research and innovation programme under grant agreement No 815044, the SLOshing Wing Dynamics (SLOWD) project. The statements made herein do not necessarily have the consent or agreement of the SLOWD consortium and represent the opinion and findings of the author(s).

To my late parents Patrick and Kehilwe Nchupang

Contents

Nomenclature

Abbreviations

CFD	Computational Fluid Dynamics
IBL	Incompressible Boundary Layer
IBP	Integration-By-Parts
IBVP	Initial-Boundary Value Problem
INS	Incompressible Navier-Stokes
LHS	Left Hand Side
MMS	Method of Manufactured Solution
ODE	Ordinary Differential Equation
PDE	Partial Differential Equation
RHS	Right Hand Side
SAT	Simultaneous Approximation Term
SBP	Summation-By-Parts

Greek Symbol

Γ	Boundary of domain Ω
Λ	Eigenvalue matrix
λ	Eigenvalue
μ	Dynamical viscosity
ν	Kinematic viscosity
Ω	Domain
ρ	Density

Mathematical operators and symbols

$\frac{d}{dt}(\cdot),\ (\cdot)_t$	Temporal derivative

$\int\limits_{\Omega}(\cdot)d\Omega$	Volume integral
$\mathcal{O}$	Order
∇	Gradient operator
$\oint\limits_{\Gamma}(\cdot)ds$	Boundary integral
$\otimes$	Kronecker product
$\partial_x(\cdot)$	Partial derivative of x
$\triangle$	Laplace operator
$\det(\cdot)$	Determinant

Roman Symbol

nD	n dimensions
p	Pressure
u	Horizontal component of velocity
$U_\infty,\ V_\infty$	Freestream velocity
v	Vertical component of velocity

Figures

Tables

Chapter 1

Introduction

1.1 Background

In recent years, there has been considerable interest in the numerical simulations of incompressible flows due to their numerous industrial applications. These include weather forecasting [1], modeling blood circulations [2], and analysing airflow around vehicles [3]. Fluid flows are classified as incompressible if the material density in the fluid parcel is invariant with respect to pressure i.e. $d\rho/dp = 0$ [4]. The amount of compression of fluid flows can also be determined using Mach number ($M = u/c$), where u is the local flow velocity field and c is the speed of sound. Although all fluids in general are compressible to some extent, it is widely accepted that external flows (such as aerodynamics) at Mach number less than 0.3 can be treated as incompressible [5] (since $d\rho/dp = c^{-2}$ and $c \ll 1$, using Bernoulli's principle) [6]. This implies that for low-speed external flows, density variation is negligibly small irrespective of the pressure change. In fluid dynamics, the incompressible Navier-Stokes (INS) equations are regularly used to model a wide range of industrial problems. The INS model is a system of nonlinear partial differential equations (PDEs) consisting of the conservation of mass and momentum equations. Despite being used regularly, this model has no closed-form solution and is one of the unsolved *Millennium prize problems* [7]. As a result, numerical methods are used to approximate the evolution of flow variables.

The main challenge of approximating the solution of the INS equations with finite digit arithmetic computing is the decoupling between the flow density and pressure, which leads to a divergence-free velocity field in the continuity equation. Naive discretization (today the norm) of $\nabla \cdot \mathbf{u} = 0$ leads to a singular coefficient matrix in the differential operator, causing non-physical oscillations in the solution field. This phenomenon is known as the saddle-point problem [8]. Mainstream incompressible flow solution schemes such as nek5000 [9] and gridap [10] circumvent this by augmenting the incompressible mass conservation equation as $\nabla \cdot \mathbf{u} = \epsilon_{incomp}$, to remove the nullspace of the incompressible differential operator. The two main augmentation approaches are the so-called pressure-based (projection scheme) [11] and density-based (artificial compressibility) methods [12]. In addition, the convective term is computed using upwind schemes [13] to avoid spurious solutions arising from the central approximation methods.

In this study, we employ the celebrated incompressible boundary layer (IBL) equations as a model problem and prove the existence of a stable and high order accurate solution without any need for additional augmented pressure/density based equations and without the use of upwind-

ing. The discretization method is finite difference on summation-by-parts (SBP) form [14–16] which is used in combination with simultaneous approximation term (SAT) [17] boundary condition imposition. The augmentation of the SBP operators with the SAT technique allows the proofs of stability to be straightforwardly attainable. This is especially the case when two apparently conflicting boundary conditions are to be applied at a specific location e.g. where in- and outflow conditions meet. Note that as per [18], the methodology employed in this work proves stability first for the continuous equations followed by its mimicking in discrete form. The energy method [19] is used for this purpose and allows derivation of the desired boundary conditions that yields an estimate. Furthermore, the stable imposition of these boundary conditions using SAT eliminates the saddle point problem typically associated with the spatial operator of the incompressible flow equations leading to unique solutions [8, 20, 21]. Importantly, this is without the use of so-called upwinding for discretization. Note that though this work employs high-order finite difference approximations, the analysis also holds for any numerical approximations that can be written on SBP form. Examples include discontinuous Galerkin method [22, 23], spectral element method [24], finite element method [25], and finite volume method [26, 27].

1.2 Problem statement

Mainstream INS solvers employ augmentation methods to remove the nullspace of the continuity equation's differential operator while enforcing divergence-free velocity. To motivate the rationale for our investigation, we point out the following shortcomings of these augmentation methods:

i. Additional boundary conditions which place additional constraints on pressure gradients at boundaries are required [28, 29]. The physical correctness of these boundary conditions is unclear.

ii. They introduce an artificial error-term, which may degenerate high order accuracy.

iii. They introduce additional equations which make proofs of stability less straightforward. For example, see [30].

iv. The ubiquitous practice of upwinding convective terms when solving incompressible flows adds both complexity and nonphysical dissipation to the flow solution [13].

1.3 The aim and objectives

The objective of this study sought to address the aforementioned drawbacks by developing a provably stable and high order accurate approximation that bypasses the need to augment $\nabla \cdot \mathbf{u} = 0$ or upwind the convective terms. To achieve this, we follow the guideline for constructing a well-posed continuous problem provided in [18] and further exemplified on the fully incompressible Navier-Stokes equations in [31, 32], Euler's equations [33, 34] and the shallow water equations [35, 36]. The aims and objectives of this work are summarized as follows:

i. To derive a new set of energy stable boundary conditions for the IBL equations using the energy method and to obtain a continuous energy estimate.

ii. To formulate a provably stable approximation for the IBL equations using high-order finite difference methods on SBP form and implement the boundary conditions weakly using the SAT method. This is done by mimicking the continuous analysis in i.

iii. To show that the newly derived boundary conditions remove the singularities associated with the nullspace of the nonlinear discrete spatial operator.

iv. To verify the developed approximation scheme for high-order accuracy using numerical experiments.

v. Finally, to compare the numerical results with the well-known Blasius similarity solution, as well as that resulting from the solution of the incompressible Navier Stokes equations.

1.4 Hypothesis

Stable implementation of the energy stable boundary conditions using the SAT technique can remove the nullspace of the IBL equations' differential operator. The resulting scheme is provably stable and high-order accurate.

1.5 Published work

M. P. Nchupang, A. G. Malan, F Laurén, J. Nordström, *A provably stable and high-order accurate finite difference approximation for the incompressible boundary layer equations.* Journal of Computers and Fluids 2023. Available Online

1.6 Thesis outline

This document consists of eight chapters including introduction and conclusion. The following is the summary of each.

- Chapter 1: Introduction. This chapter provides a background and motivation for the present study. It also highlights the aims and objectives of this thesis. The chapter closes with the organization and summary of chapters.

- *Chapter 2: Preliminaries: Concepts and Definitions.* In this chapter, mathematical concepts and definitions used in the present study are presented. In particular, well-posedness of the continuous problems and the stability of the corresponding discrete problems. The energy method which is used as a tool to construct well-posed problems is introduced and further exemplified using a one-dimensional linear advection equation. This is followed by the finite difference operators on SBP form. The chapter is concluded with the procedure to extend the SBP framework to curved domains.

- *Chapter 3: Incompressible flow.* This chapter is devoted to setting the stage for the continuous analysis. Starting with the INS equations as an original model to the problem, IBL equations specific to laminar flows are derived.

- *Chapter 4: Stable boundary conditions for the IBL equations.* In this chapter, the conditions for energy stability of the IBL equations are derived following the *roadmap* [18]. By inspecting the boundary terms emanating from the energy method, a new set of energy stable boundary conditions for the IBL equations specific to the flat-plate laminar flow problem are derived. It is further shown that both the strong and weak imposition of these boundary conditions lead to boundedness.

- *Chapter 5: SBP-SAT approximation for the IBL equations.* The continuous analysis presented in the previous chapter is mimicked in this chapter to develop a provably stable SBP-SAT numerical scheme for the IBL equations. The newly derived boundary conditions are implemented weakly using the SAT method and the discrete energy estimates that resemble the continuous counterparts are obtained. A key contribution of this work is presented in this chapter. That is, it is proved that the newly derived boundary conditions eliminate the saddle-point problem associated with the differential operator of the IBL equations. The chapter concludes with the temporal discretization using Backward Euler method, and Newton's iteration method for solving nonlinear systems.

- *Chapter 6: Numerical experiments and convergence rates.* In this chapter, the approximation developed in the previous chapter is verified for high-order accuracy using the method of manufactured solution. This is followed by computing the numerical solution of the Blasius boundary layer problem. Furthermore, the results are compared with the well-known similarity solution. A similar problem is considered on a truncated domain where the analytical solution is injected as inflow data.

- *Chapter 7: The fully incompressible Navier-Stokes equations.* A brief summary of the continuous and discrete formulations of the INS equations is presented in this chapter. The SBP-SAT approximation for the INS equations is then validated using the benchmark lid-driven cavity problem. Lastly, the INS equations' solution is compared with the Blasius similarity solution to numerically corroborate the assumptions made in Chapter 3 when deriving the IBL equations.

- *Chapter 8: Conclusions and Future Work.* In this chapter, the summary and conclusions of the thesis are presented. This is followed by a list of research work earmarked for the future.

Chapter 2

Preliminaries: Concepts and Definitions

Most PDEs describing physical phenomena do not have closed-form solutions, which prompts the use of numerical methods. The credibility of a numerical approximation depends on the ability to guarantee stability and convergence. The former is analogous to well-posedness of the underlying initial-boundary value problem (IBVP), which is characterized by the existence of a unique and bounded solution [37]. Moreover, such a solution relies almost entirely on the choice of boundary conditions [38–40]. In particular, the correct number and form of the boundary conditions guarantee boundedness and existence. For linear problems, uniqueness follows directly from boundedness [37] and the two are sufficient for stability. However, proving existence and uniqueness for nonlinear PDEs is non-trivial, and in general only boundedness is achievable. The energy method [19, 38] which involves multiplying IBVP with the solution and integrating the resulting product, is powerful in constructing such boundary conditions (see [38–40]). It relies on the principle of integration-by-parts (IBP), inner products and the corresponding norms in order to derive continuous estimates in terms of external data. Once equipped with a continuous estimate, stability follows by discretely imitating the continuous analysis. The finite difference method on SBP form [41] augmented with weakly implemented boundary conditions using SAT [17, 42] technique, provides a suitable framework for producing discrete estimates. The link between well-posedness and stability will be demonstrated in this chapter using a one-dimension (1D) advection problem. More details can be found in [43, 44].

2.1 Integration rules, inner products and norms

In this section, we introduce the mathematical tools that will be used later. Let $\mathbb{R}$ be a field of real numbers equipped with standard operations and $\Omega \subset \mathbb{R}$ denote a 1D finite domain with boundary Γ. We consider $\Omega = [0, 1]$ for ease of presentation. For two square-integrable functions u, v on Ω, the inner product and the corresponding norm are respectively

$$(u, v) = \int_0^1 uv dx, \quad ||u||^2 = (u, u). \tag{2.1a}$$

To present the discrete version of (2.1a), we first discretize Ω with $N + 1$ evenly spaced points, where each grid point is given by $x_i = x_0 + ih$ and $h = 1/N$ is the distance between any two consecutive points. A scalar function $u(x)$ evaluated at grid point x_i is denoted by

$u_i = u(x_i)$. Further, we package these as the $(N+1) \times 1$ vector $\mathbf{u} = (u_0, u_1, u_2, \dots u_N)^\mathsf{T}$. The discrete analogue of (2.1a) is

$$(\mathbf{u}, \mathbf{v})_\mathsf{H} = \sum_{i=0}^{N} u_i v_i h = \mathbf{u}^\mathsf{T} \mathsf{H} \mathbf{v}, \qquad ||\mathbf{u}||_\mathsf{H}^2 = (\mathbf{u}, \mathbf{u})_\mathsf{H}, \tag{2.1b}$$

where H is symmetric and positive definite.

Next, we state the IBP rule [45] for two functions u, v

$$\int_0^1 u v_x dx = uv\big|_{x=1} - uv\big|_{x=0} - \int_0^1 u_x v dx, \tag{2.2a}$$

where subscript x denotes a derivative operator in the x direction. Alternatively, (2.2a) can be written in inner product notation (2.1) as

$$(u, v_x) = uv\big|_{x=1} - uv\big|_{x=0} - (u_x, v).$$

The discrete analogue of (2.2a) is called the summation-by-parts (SBP) rule [41]

$$(\mathbf{u}, D\mathbf{v})_\mathsf{H} = u_N v_N - u_0 v_0 - (D\mathbf{u}, \mathbf{v})_\mathsf{H}, \tag{2.2b}$$

where D is the discrete differential operator.

2.2 Well-posed problems

Consider the following IBVP defined on a 1D domain Ω with boundary Γ

$$\begin{aligned} w_t + \mathcal{D}(x, \partial_x) w &= F(t, x), \qquad x \in \Omega, \quad t > 0, \\ \mathcal{B} w &= g(t, x), \qquad x \in \Gamma, \quad t \geq 0, \\ w &= f(0, x), \qquad x \in \Omega, \quad t = 0, \end{aligned} \tag{2.3}$$

where w is the unknown solution, $\mathcal{D}$ denotes the linear differential operator while $\mathcal{B}$ is the boundary operator. The continuous functions F, g and F respectively denotes the forcing function, boundary and initial data. Further, they are assumed to be compatible such that w is sufficiently smooth.

Definition 2.1. The IBVP (2.3) with nonzero data and forcing function is *strongly well-posed* if a unique solution w exists and satisfies

$$||w(t,x)||_\Omega^2 \leq \kappa(t) \left(||f(0,x)||_\Omega^2 + \int_0^t \left(||F(\tau, x)||_\Omega^2 + ||g(\tau, x)||_\Gamma^2 \right) d\tau \right), \tag{2.4}$$

where κ is a bounded function that is independent of the solution and data. It is said to be *well-posed* if a unique solution w of (2.3) exists which satisfies (2.4) with $F = g = 0$ [37]. In (2.4), $||\cdot||_\Omega$, $||\cdot||_\Gamma$ are the norms defined on Ω and Γ, respectively.

Equation (2.4) is called the energy estimate and describes the boundedness of w. Further, for linear problems such as (2.3), boundedness implies uniqueness [37]. Suppose that another solution v of (2.3) satisfying (2.4) exists. Then by linearity of (2.3), the difference $\delta w = w - v$ is also a solution and satisfies

$$||\delta w||_{\Omega}^2 = ||w - v||_{\Omega}^2 \leq \kappa(t) \left(||\delta f||_{\Omega}^2 + \int_0^t \left(||\delta F||_{\Omega}^2 + ||\delta g||_{\Gamma}^2 \right) d\tau \right), \tag{2.5}$$

where δF, δf, δg are perturbed data. However, as δF, δf, $\delta g \to 0$, $\delta w \to 0$ it infers that $w = v$ i.e. the solution of (2.3) is unique. Therefore, we characterize well-posedness of an IBVP by the existence of a unique and bounded solution.

Remark 2.1. *For nonlinear IBVP problems, the relation (2.5) does not hold, which makes the proof of uniqueness more challenging. In addition, the existence is in general not known. In such cases, we will not refer to the IBVP as well-posed.*

2.3 Stability

Consider the semi-discrete formulation of (2.3)

$$\begin{aligned} \mathbf{w}_t + \boldsymbol{\mathcal{D}}\mathbf{w} &= \mathbf{F}, \quad t > 0, \\ \boldsymbol{\mathcal{B}}\mathbf{w} &= \mathbf{g}, \quad t > 0, \\ \mathbf{w} &= \mathbf{f}, \quad t = 0, \end{aligned} \tag{2.6}$$

where $\mathbf{w} = (w_0, w_1, \ldots, w_N)^{\mathsf{T}}$ with $w_i = w(t, x_i)$ is a vector containing the pointwise values of w in (2.3) evaluated at grid x_i. Here, as before, x_i denote equispaced grid points given by $x_i = x_0 + ih$, $i = 0, 1, 2, \ldots, N$ where h is the distance between any two neighbouring points. The discrete operators $\boldsymbol{\mathcal{D}}$, $\boldsymbol{\mathcal{B}}$ respectively mimic the differential and boundary operators $\mathcal{D}$, $\mathcal{B}$ in (2.3). Further, the vectors $\mathbf{F}$, $\mathbf{g}$ and $\mathbf{f}$ contains the pointwise values of data F, g, f projected on the computational grid x_i, respectively. Similar to Definition 2.1, we define stability.

Definition 2.2. The approximation (2.6) with nonzero vectors $\mathbf{F}$, $\mathbf{g}$, $\mathbf{f}$ is *strongly stable* if

$$||\mathbf{w}||_{\Omega_h}^2 \leq \kappa(t) \left(||\mathbf{f}||_{\Omega_h}^2 + ||\mathbf{F}||_{\Omega_h}^2 + ||\mathbf{g}||_{\Gamma_h}^2 \right), \tag{2.7}$$

where $\kappa(t)$ is bounded, and independent of the solution and data. The approximation (2.6) is *stable* if $\mathbf{w}$ satisfies (2.7) with $\mathbf{g} = \mathbf{F} = \mathbf{0}$ [37].

Equation (2.7) infers that a small disturbance on the data of the problem will result in a small change of the numerical solution. Stability is the discrete correspondence of well-posedness for linear problems, provided that the approximation is sufficiently accurate. Therefore, one needs to first obtain the continuous estimates before considering the discrete formulation.

Remark 2.2. *For the nonlinear case, stability is a necessary but not sufficient condition for continuous dependence of the numerical solution on the data.*

2.4 The energy method

To obtain the estimates (2.4) and (2.7), the correct number and form of the boundary conditions must be imposed at the correct position on the boundary [46]. In this section, we demonstrate how the energy method can be used to provide this information using a 1D advection problem [43].

2.4.1 Strongly imposed boundary conditions

Consider the 1D linear advection equation with constant coefficient

$$\begin{aligned} w_t + aw_x &= 0, \qquad x \in [0,1], \quad t > 0, \\ \mathcal{B}w &= g(t), \quad x = [0,1], \quad t \geq 0, \\ w(0,x) &= f(x), \quad x \in [0,1], \quad t = 0, \end{aligned} \tag{2.8}$$

where $a > 0$ is the advection speed and $\mathcal{B}$ denotes the boundary operator. The continuous functions g, f are the boundary and initial data, respectively. The energy method and IBP (2.2a) applied to (2.8) yields

$$\frac{d}{dt}||w||^2 = aw(t,0)^2 - aw(t,1)^2. \tag{2.9}$$

Equation (2.9) describes the rate of change of the energy estimate. Further, it requires the boundary terms on the right-hand side (RHS) to be bounded such that the temporal integration leads to a bounded energy. In (2.9), the right boundary term has an appropriate sign since $a > 0$ while the left boundary term is positive and adds growth to the energy rate. Therefore, to cap this growth, one boundary condition must be prescribed at $x = 0$. Moreover, it must be of the Dirichlet type i.e. $w(t,0) = g(t)$ since the boundary terms in (2.9) involve the solution only, and hence yields $\mathcal{B} = 1$ in (2.8). Therefore, by strongly imposing this boundary condition in (2.9), the energy rate becomes

$$\frac{d}{dt}||w||_{\mathsf{I}}^2 = ag(t)^2 - aw(t,1)^2 \leq ag(t)^2. \tag{2.10}$$

Lastly, integrating (2.10) in time over a finite time-domain $t \in [0,T]$ leads to the estimate

$$\int_0^T \frac{d}{dt}||w||^2 dt \leq a\int_0^T g(t)^2 dt \quad \Rightarrow \quad ||w(T,x)||^2 \leq ||f||^2 + a\int_0^T g(t)^2 dt. \tag{2.11}$$

Therefore, (2.8) is well-posed using Definition 2.1. Next, we summarize the key steps for constructing a well-posed problem using the energy method:

i Multiply the IBVP with the solution and integrate it over the domain to derive the energy rate equation.

ii Identify the boundary growth terms.

iii Prescribe the minimal number of boundary conditions (equal to the number of the growth terms) with the appropriate form to derive a bounded energy estimate.

iv Integrate in time to find the estimate.

Remark 2.3. *The energy method is by no means the only method available to construct well-posed problems. Other techniques include the Fourier method and Laplace transform analysis [15, 16]. However, unlike the energy method, these have specific limitations. For example, the Fourier technique is limited to a certain class of PDEs such as Cauchy or periodic problems. The Laplace transform method is more technically complicated and essentially limited to 1D problems.*

2.4.2 Weakly imposed boundary conditions

In (2.10), the boundary condition at the left boundary was strongly implemented. However, imposing boundary conditions this way can lead to stability issues in the discrete setting [47, 48]. To remedy this, the boundary condition in (2.8) can be implemented weakly by combining it with the PDE as a penalty term. To exemplify this, we return to consider a 1D advection problem

$$\begin{aligned} w_t + aw_x &= \mathcal{L}\left(\sigma(w-g)\right), \qquad x \in [0,1], \quad t \geq 0, \\ w(0,x) &= f(x), \qquad\qquad\quad x \in [0,1], \quad t = 0, \end{aligned} \tag{2.12}$$

where σ is the penalty coefficient and will be determined such that we have an estimate. The function $\mathcal{L}(\cdot)$ is called the *lifiting operator* [49, 50] and is defined for functions u, v as

$$\int_0^1 u\mathcal{L}\left(v\right) dx = uv\big|_{x=0}. \tag{2.13}$$

In (2.12), the solution is pulled towards data by penalizing the deviation between them, weighted with σ. Moreover, σ is determined to guarantee stability by applying the energy method to (2.12)

$$\frac{d}{dt}||w||^2 = (a+2\sigma)w(t,0)^2 - aw(t,1)^2 - 2\sigma w(t,0)g(t). \tag{2.14}$$

Similar to (2.19), the boundary term at $x = 1$ in (2.14) has the correct sign and σ must be chosen such that the boundary terms at $x = 0$ are negative. The choice $\sigma = -a$ [43] simplifies (2.14) to

$$\frac{d}{dt}||w||^2 = -aw(t,1)^2 - a\left(w(t,0) - g(t)\right)^2 + ag(t)^2 \leq ag(t)^2, \tag{2.15}$$

which is identical to (2.10) with an additional dissipation term. Therefore, temporal integration leads to the estimate (2.11).

2.5 Summation-By-Parts operators

The discrete energy method imitates the continuous energy method discretely in a sense that it relies on the SBP rule (2.2b) to produce discrete estimates that resemble those of the continuous IBVPs. This method involves multiplying a numerical scheme on the left with a quadrature matrix followed by the transpose of an approximation vector. In addition, a discretization method must have a specific form such that an SBP rule can be used. The intent of this section is to introduce the finite difference methods on SBP form which were first derived in [51] and later developed in [52].

Definition 2.3. A matrix $D = P^{-1}Q$ is a first derivative SBP operator of order s if it is an accurate approximation of $\frac{d}{dx}$ with

i. $D\mathbf{x}^j = j\mathbf{x}^{j-1}, \quad j \in 1, \dots, s \qquad \mathbf{x} = (x_0, x_1, \dots, x_N)^\mathsf{T},$

ii. $D\mathbf{1} = \mathbf{0}, \qquad \mathbf{1} = (1, \dots, 1)^\mathsf{T}, \quad \mathbf{0} = (0, \dots, 0)^\mathsf{T},$

iii. P is symmetric and positive definite,

iv. Q is almost skew-symmetric and satisfies $Q + Q^\mathsf{T} = E = \text{diag}(-1, 0, \dots, 0, 1)$.

The exponentiation in $\mathbf{x}^j$ should be interpreted pointwise. Further, D satisfies the SBP rule (2.2b) since for any two nonzero vectors $\mathbf{w}$, $\mathbf{u}$, we have

$$\begin{aligned}(\mathbf{w}, D\mathbf{u})_P &= \mathbf{w}^\mathsf{T} P P^{-1} Q \mathbf{u} \\ &= \mathbf{w}^\mathsf{T}(Q + Q^\mathsf{T} - Q^\mathsf{T})\mathbf{u} \\ &= \mathbf{w}^\mathsf{T}(Q + Q^\mathsf{T})\mathbf{u} - \mathbf{w}^\mathsf{T} Q^\mathsf{T} P^{-1} P \mathbf{u} \\ &= \mathbf{w}^\mathsf{T} E \mathbf{u} - (D\mathbf{w})^\mathsf{T} P \mathbf{u} \\ &= w_N u_N - w_0 u_0 - (D\mathbf{w}, \mathbf{u})_P,\end{aligned} \tag{2.16}$$

which discretely mimics IBP (2.2a). Since $P = P^\mathsf{T} > 0$, it defines the norm $||\mathbf{w}||_P^2 = \mathbf{w}^\mathsf{T} P \mathbf{w}$ (see (2.1b)) which is discretely equivalent to the L_2-norm (2.1b). Further, P is a quadrature rule approximating the continuous integral $\mathbf{1}^\mathsf{T} P \mathbf{w} \approx \int_\Omega w dx$ [53]. Henceforth, we will refer to the matrix P as the P-norm.

Remark 2.4. *Definition 2.3 is independent of a discretization method. This enables the SBP framework to be extended to a wide range of discretization methods including Galerkin methods [22, 23, 54], spectral element methods [24] and finite volume methods [26, 27].*

2.5.1 The structure of finite difference operators on SBP form

Initially, SBP operators were introduced as a framework to derive high order-accurate finite difference approximations which are based on central difference stencils [51, 52]. The challenge, however with using central difference arises near boundary regions where the stencil protrudes the boundary. This drawback is circumvented by modifying the stencil near the boundaries to so-called non-centered difference stencils [55–57]. However, the trade-off with the latter approach is that in order to keep the SBP property, a drop in accuracy near the boundaries must be accepted. To illustrate this, and subsequently present the general structure of finite difference operators on SBP form, we revisit the model problem (2.8) with a unit advection speed.

Consider a unit domain $x \in [0, 1]$, discretized with $N + 1$ evenly spaced grid points. Each grid point is defined by $x_i = x_0 + ih$, $i = 0, 1, \dots, N$, where $h = 1/N$ is the distance between any two consecutive grid points and $x_0 = 0$, $x_N = 1$ are the boundary points. As before, the notation $w(x_i) = w_i$ denotes the solution projected on the grid points x_i. The central difference approximation of w_x in (2.8) is

$$\frac{w_{i+1} - w_{i-1}}{2h} = w_x + \mathcal{O}(h^2), \tag{2.17a}$$

where $\mathcal{O}(h^2)$ is the order of the truncation error. Equation (2.17a) is evaluated at all internal grid points x_i, however, at the boundary points x_0, x_n, (2.17a) make use of w_{-1} and w_{N+1} which lies outside the computational domain. The modified one-sided stencil via Euler's methods gives

$$\begin{aligned} \frac{w_1 - w_0}{h} &= w_x + \mathcal{O}(h), \quad i = 0, \\ \frac{w_N - w_{N-1}}{h} &= w_x + \mathcal{O}(h), \quad i = N, \end{aligned} \tag{2.17b}$$

which both have the truncation error of order one, a drop from order two in (2.17a). Approximation (2.17) can be written in matrix-vector form as

$$D\mathbf{w} = \frac{1}{2h}\begin{bmatrix} -2 & 2 & & & \\ -1 & 0 & 1 & & \\ & \ddots & \ddots & \ddots & \\ & & -1 & 0 & 1 \\ & & & -2 & 2 \end{bmatrix}\begin{bmatrix} w_0 \\ w_1 \\ \vdots \\ w_{N-1} \\ w_N \end{bmatrix} = \mathbf{w}_x + \mathbf{t}, \tag{2.18}$$

where $\mathbf{w}_x$ is the vector containing point-wise values of w_x while vector $\mathbf{t} = \big(\mathcal{O}(h), \mathcal{O}(h^2), \ldots, \mathcal{O}(h^2), \mathcal{O}(h)\big)^{\mathsf{T}}$ contains the truncation errors. Following Definition 2.3, the operator D can be written on SBP form $D = P^{-1}Q$, where

$$P = h\begin{bmatrix} \frac{1}{2} & & & & \\ & 1 & & & \\ & & \ddots & & \\ & & & 1 & \\ & & & & \frac{1}{2} \end{bmatrix}, \quad Q = \frac{1}{2}\begin{bmatrix} -1 & 1 & & & \\ -1 & 0 & 1 & & \\ & \ddots & \ddots & \ddots & \\ & & -1 & 0 & 1 \\ & & & -1 & 1 \end{bmatrix}. \tag{2.19}$$

Further, matrices P, Q satisfy the SBP properties $P = P^{\mathsf{T}} > 0$ and $Q + Q^{\mathsf{T}} = E$. A close inspection of these matrices reveals that P is a diagonal matrix with *special elements* near the boundary regions which emanate from the one-sided stencils enclosing the operator (see (2.17b)). Furthermore, the diagonal elements of P are the weights of the composite Trapezoidal rule [58], and hence as mentioned before, is a quadrature rule. In (2.19), Q is a banded matrix with block-like structures near the boundaries. The interior band consists of the coefficients of the repeated central difference stencil (2.17a) and has a bandwidth of 3. Meanwhile, the block structure near the boundaries consists of the coefficients of the one-sided stencil (2.17b). Next, we present the general form of P and Q for arbitrary order of accuracy in 1D [41]

$$P = h\left[\begin{array}{c|c|c} \mathsf{P}_0 & & \\ \hline & 1 & \\ & \ddots & \\ & & 1 \\ \hline & & \tilde{\mathsf{P}}_0 \end{array}\right], \quad Q = \left[\begin{array}{c|c|c} \mathsf{Q}_0 & \mathsf{M} & 0 \\ \hline -\mathsf{M}^{\mathsf{T}} & \mathsf{A} & \widetilde{\mathsf{M}}^{\mathsf{T}} \\ \hline 0 & -\widetilde{\mathsf{M}} & -\widetilde{\mathsf{Q}}_0 \end{array}\right], \tag{2.20}$$

where $P_0 = \mathrm{diag}(p_0, p_1, \ldots, p_r)$, Q_0, M, and A are

$$\mathsf{Q}_0 = \begin{bmatrix} -\frac{1}{2} & q_{0,1} & \cdots & q_{0,r} \\ -q_{0,1} & 0 & & \vdots \\ \vdots & & \ddots & \vdots \\ -q_{0,r} & \cdots & \cdots & 0 \end{bmatrix}, \quad \mathsf{M} = \begin{bmatrix} & & \\ a_s & & \\ \vdots & \ddots & \\ a_1 & \cdots & a_s \end{bmatrix},$$

$$\mathsf{A} = \begin{bmatrix} 0 & a_1 & \cdots & a_s & & & & & \\ -a_1 & 0 & a_1 & \cdots & a_s & & & & \\ \vdots & \ddots & \ddots & \ddots & & \ddots & & & \\ -a_s & \cdots & -a_1 & 0 & a_1 & \cdots & a_s & & \\ & \ddots & & \ddots & \ddots & \ddots & & \ddots & \\ & & -a_s & \cdots & -a_1 & 0 & a_1 & \cdots & a_s \\ & & & \ddots & & \ddots & \ddots & \ddots & \vdots \\ & & & & -a_s & \cdots & -a_1 & 0 & a_1 \\ & & & & & -a_s & \cdots & -a_1 & 0 \end{bmatrix}.$$

In (2.20), the *tilde* sign denotes the matrix transposed along the anti-diagonal. The index $0, \ldots, r$ indicate the nodes near the boundaries where a one-sided stencil is used, yielding the block-matrix Q_0. For an arbitrary order of accuracy $2s$ at the interior points, the coefficients of the repeated central difference stencil $-\mathsf{M}^\mathsf{T}\mathsf{A}\tilde{\mathsf{M}}^\mathsf{T}$ are given by

$$\frac{1}{h}\sum_{k}^{s} a_k \left(w_{i+k} - w_{i-k}\right) = \mathbf{w}_x + \mathcal{O}\left(h^{2s}\right), \quad a_k = \frac{(-1)^{k+1}(s!)^2}{(s+k)!(s-k)!}, \tag{2.21}$$

and the bandwidth of the interior stencil is $2s+1$ where $2s$ ($s > 0$) is the order of accuracy of the interior points [59]. For the 2^{nd}-order ($s = 1$) case (2.19), the bandwidth of the central difference stencil is $2(1) + 1 = 3$. Similarly, for the 4^{th}-order operators

$$P = h \begin{bmatrix} \frac{17}{48} & & & & & & \\ & \frac{59}{48} & & & & & \\ & & \frac{43}{48} & & & & \\ & & & \frac{49}{48} & & & \\ & & & & 1 & & \\ & & & & & \ddots & \end{bmatrix},$$

$$Q = \begin{bmatrix} -\frac{1}{2} & \frac{59}{96} & -\frac{1}{12} & -\frac{1}{32} & & & & \\ -\frac{59}{96} & 0 & \frac{59}{96} & 0 & & & & \\ \frac{1}{12} & -\frac{59}{96} & 0 & \frac{59}{96} & -\frac{1}{12} & & & \\ \frac{1}{32} & 0 & -\frac{59}{96} & 0 & \frac{2}{3} & -\frac{1}{12} & & \\ & & \frac{1}{12} & -\frac{2}{3} & 0 & \frac{2}{3} & -\frac{1}{12} & \\ & & & \ddots & \ddots & \ddots & \ddots & \ddots \end{bmatrix},$$

the bandwidth of the interior stencil is 5.

Remark 2.5. *The finite difference SBP operators of the form (2.19) have been derived up to 8^{th}-order and can be found in [16].*

2.5.1.1 Second derivatives SBP operators

Finite difference methods approximating higher derivatives can also be written on SBP form [60]. These operators can either be constructed directly from the stencil or by applying the first derivative operator repeatedly up to the order of the continuous derivative. The former results in a compact difference stencil while the latter results in a wide stencil. The PDEs considered in the present study contain the first and second derivatives where we will use a wide stencil. The general form of the SBP operators approximating the second derivatives is

$$D_2 = P^{-1}R, \quad P = P^{\mathsf{T}} > 0, \quad R = -C + S, \tag{2.22}$$

where C is often, but not necessarily symmetric and it consists of the coefficients of the repeated central difference stencil. In (2.22), S is a sparse matrix with the coefficients of a one-sided stencil on the first and last row [61–63]. The first derivative SBP operator applied twice in the form (2.22) yields

$$D_2 = DD = P^{-1}QP^{-1}Q = P^{-1}\left(B - Q^{\mathsf{T}}\right)P^{-1}Q = P^{-1}\left(-C + S\right), \tag{2.23}$$

where $C = D^{\mathsf{T}}PD$ and $S = BD$. In (2.23), we used the SBP property $Q + Q^{\mathsf{T}} = E$. We remark that if a PDE contains the first and second derivatives then the SBP operators D and D_2 approximating these terms must have the same P-norm.

2.5.2 The discrete energy estimate

Next, we formulate the semi-discrete approximation of (2.12) by keeping the temporal derivative continuous and discretizing the spatial term with finite difference SBP operators.

$$\begin{aligned} \mathbf{w}_t + aD\mathbf{w} &= \sigma P^{-1}E_0\left(\mathbf{w} - \mathbf{g}\right), \quad && t \geq 0, \\ \mathbf{w} &= \mathbf{f}, && t = 0. \end{aligned} \tag{2.24}$$

Here, $\mathbf{w} = (w_0, w_1, \ldots, w_N)^{\mathsf{T}}$ and $D = P^{-1}Q$ is a first derivative SBP operator. The term on the RHS of (2.24) is called the simultaneous approximation term (SAT) [17] and discretely mimics the boundary penalty term in (2.12). Further, $P^{-1}E_0$ plays the role of the lifting operator $\mathcal{L}(\cdot)$ in

(2.13) discretely where $E_0 = \text{diag}(1, 0, \dots, 0)$. The penalty coefficient σ is yet to be determined for stability and the vectors $\mathbf{g}$, $\mathbf{f}$ contain the boundary and initial data, respectively.

Next, we apply the discrete energy method. Since P is a quadrature matrix, we analogously to the continuous case, multiply (2.24) on the left with $2\mathbf{w}^\mathsf{T}P$ to obtain

$$2\mathbf{w}^\mathsf{T}P\mathbf{w}_t + 2a\mathbf{w}^\mathsf{T}Q\mathbf{w} = 2\sigma w_0 \left(w_0 - g_0\right). \tag{2.25}$$

Note that $\mathbf{w}^\mathsf{T}P\mathbf{w}_t$ in (2.25) can be rewritten as $\frac{1}{2}\frac{d}{dt}(\mathbf{w}^\mathsf{T}P\mathbf{w}) = \frac{1}{2}\frac{d}{dt}||\mathbf{w}||_P^2$. Similarly, we replace $\mathbf{u}$ with $\mathbf{w}$ in (2.16) and reuse the results to simplify $2\mathbf{w}^\mathsf{T}Q\mathbf{w}$ as $2\mathbf{w}^\mathsf{T}Q\mathbf{w} = w_N^2 - w_0^2$. Therefore, (2.25) becomes

$$\frac{d}{dt}||\mathbf{w}||_P^2 = (a + 2\sigma)w_0^2 - aw_N^2 - 2\sigma w_0 g_0, \tag{2.26}$$

which corresponds to (2.14) discretely. Therefore, by making the similar choice $\sigma = -a$, we simplify it to

$$\frac{d}{dt}||\mathbf{w}||_P^2 = -aw_N^2 - a(w_0 - g_0)^2 + ag_0^2 \leq ag_0^2, \tag{2.27}$$

which imitates (2.15). Lastly, we integrate the temporal term over a finite domain $[0, T]$ and apply the initial data in (2.24) to obtain the estimate

$$||\mathbf{w}||_P^2 \leq ||\mathbf{f}||_P^2 + a\int_0^T g_0^2 dt,$$

which proves stability.

Remark 2.6. *In (2.27), we reused the choice of σ deduced in the continuous setting (2.14). That is, imposing the boundary condition in (2.12) weakly, prepared us for the discrete formulation. In the upcoming analysis, we will split the procedure for constructing a provably stable approximation scheme into three steps. Firstly, we derive the energy stable boundary conditions using the energy method and subsequently impose them strongly to derive an estimate. Secondly, we impose the derived boundary conditions weakly and deduce the appropriate penalty coefficients. Finally, by imitating the second step discretely, we derive a stable approximation [38].*

2.6 Convergence rates

By design, the central finite difference SBP operator D is more accurate in the interior stencil than near the boundaries, see for example (2.18). This is generalized as a theorem in [14] which states that, for diagonal P in (2.20), D exists with order of accuracy $2s$ in the interior and order of accuracy s near the boundaries. Further, a discretization of first order hyperbolic PDEs with these operators have a $s+1$ convergence rate, and $s+2$ for parabolic or second order hyperbolic PDEs, provided that they are linear and well-posed with a smooth solution. Moreover, the scheme must be consistent, nullspace consistent, nullspace invariant and energy stable. For explanations of these concepts and all details, see [64]. To demonstrate this, we consider the hyperbolic case (2.8) which has an analytical solution of the form $w(t, x) = k(x - at)$. For simplicity, we consider a cosine wave passing the domain $x \in [0, 1]$ from left to right at speed a

$$w(t, x) = \cos(3\pi(x - at)). \tag{2.28}$$

The boundary and initial data in (2.8) are sourced from (2.28) i.e. $g(t) = w(t, 0)$ while $f(x) = w(0, x)$. We further denote a vector containing the pointwise values of (2.28) with $\mathbf{w}_e$. To approximate the temporal derivative in (2.24) and finally compute $\mathbf{w}$, we extend the SBP-SAT framework to the time domain [65, 66] (see the fully discrete formulation in Appendix *A*). The rate at which the computed solution converges to the analytical solution (2.28) is

$$\mathsf{q} = \log_{10}\left(\frac{||\mathbf{w}_e - \mathbf{w}^{h_1}||_P}{||\mathbf{w}_e - \mathbf{w}^{h_2}||_P}\right) \Big/ \log_{10}\left(\frac{h_1}{h_2}\right), \tag{2.29}$$

where $||\mathbf{w}_e - \mathbf{w}||_P$ is the discrete equivalence of the L_2 of the solution error, and h_1, h_2 denote the coarse and fine mesh sizes respectively. The convergence rates are presented in (2.1) and they agree with the theoretical predictions.

N	SBP(2,1)		SBP(4,2)		SBP(6,3)		SBP(8,4)	
	L_2	q	L_2	q	L_2	q	L_2	q
41	0.0378	-	0.0020	-	0.0018	-	3.1597e-04	-
81	0.0095	2.0273	2.5740e-04	3.0372	1.1769e-04	4.0150	9.8666e-06	5.0912
121	0.0042	2.0087	7.6908e-05	3.0100	2.3209e-05	4.0452	1.3184e-06	5.0149
161	0.0024	2.0040	3.2608e-05	3.0043	7.3230e-06	4.0387	3.1614e-07	4.9999
201	0.0015	2.0027	1.6749e-05	3.0022	2.9939e-06	4.0309	1.0447e-07	4.9900
Theoretical order		2		3		4		5

Table 2.1: The L_2 norm of errors and the global order of accuracy of the approximation (2.24) using SBP operators with different orders of accuracy.

2.7 SBP operators in two dimensions

The 1D SBP operators can be extended to multi-dimensional space using Kronecker products [43]. Let A, B be invertible matrices of sizes $M \times M$ and $N \times N$, respectively. The Kronecker product of A and B, denoted by $\otimes$, is a block matrix of size $MN \times MN$

$$A \otimes B = \begin{bmatrix} a_{11}B & \dots & a_{1M}B \\ \vdots & \ddots & \vdots \\ a_{M1}B & \dots & a_{MM}B \end{bmatrix}, \tag{2.30}$$

where a_{ij} are the matrix elements of A. Furthermore, (2.30) satisfies the following properties $(A \otimes B)^{\mathsf{T}} = A^{\mathsf{T}} \otimes B^{\mathsf{T}}$, $(A \otimes B)^{-1} = A^{-1} \otimes B^{-1}$, $(A \otimes B)(C \otimes D) = AC \otimes BD$. Here, C, D are matrices with appropriate dimensions such that the matrix multiplications AC, BD are defined.

To present SBP operators in 2D, we consider the domain $\Omega = [0, 1]^2$ with boundary Γ. Further, we split the boundary as $\Gamma_{n,s,e,w}$ where the subscripts n, s, e, w denote the north, south, east and west boundaries respectively. We discretize Ω using $N+1$ and $M+1$ equidistant points. Each grid point is given by a pair (x_i, y_i) as illustrated in Figure 2.1 where $x_i = i/N$, $i = 0, 1, 2, \dots, N$ and $y_j = j/M$, $j = 0, 1, 2, \dots, M$. We package the pointwise values of a scalar function

$w_{ij} = w(x_i, y_j)$ as a $(N+1)(M+1) \times 1$ vector, following columnwise orientation as depicted in Figure 2.1:

$$\mathbf{w} = \begin{bmatrix} \vdots \\ \big[\mathbf{w}\big]_i \\ \vdots \end{bmatrix}, \quad \big[\mathbf{w}\big]_i = \begin{bmatrix} \vdots \\ w_{ij} \\ \vdots \end{bmatrix}.$$

Let I_N, I_M be unit matrices of size $(N+1)^2$ and $(M+1)^2$, respectively. The SBP operators in 2D are defined as

$$\mathbf{D}_x = P_x^{-1} Q_x \otimes \mathsf{I}_M, \quad \mathbf{D}_y = \mathsf{I}_N \otimes P_y^{-1} Q_y, \quad \mathbf{P} = P_x \otimes P_y, \tag{2.31a}$$

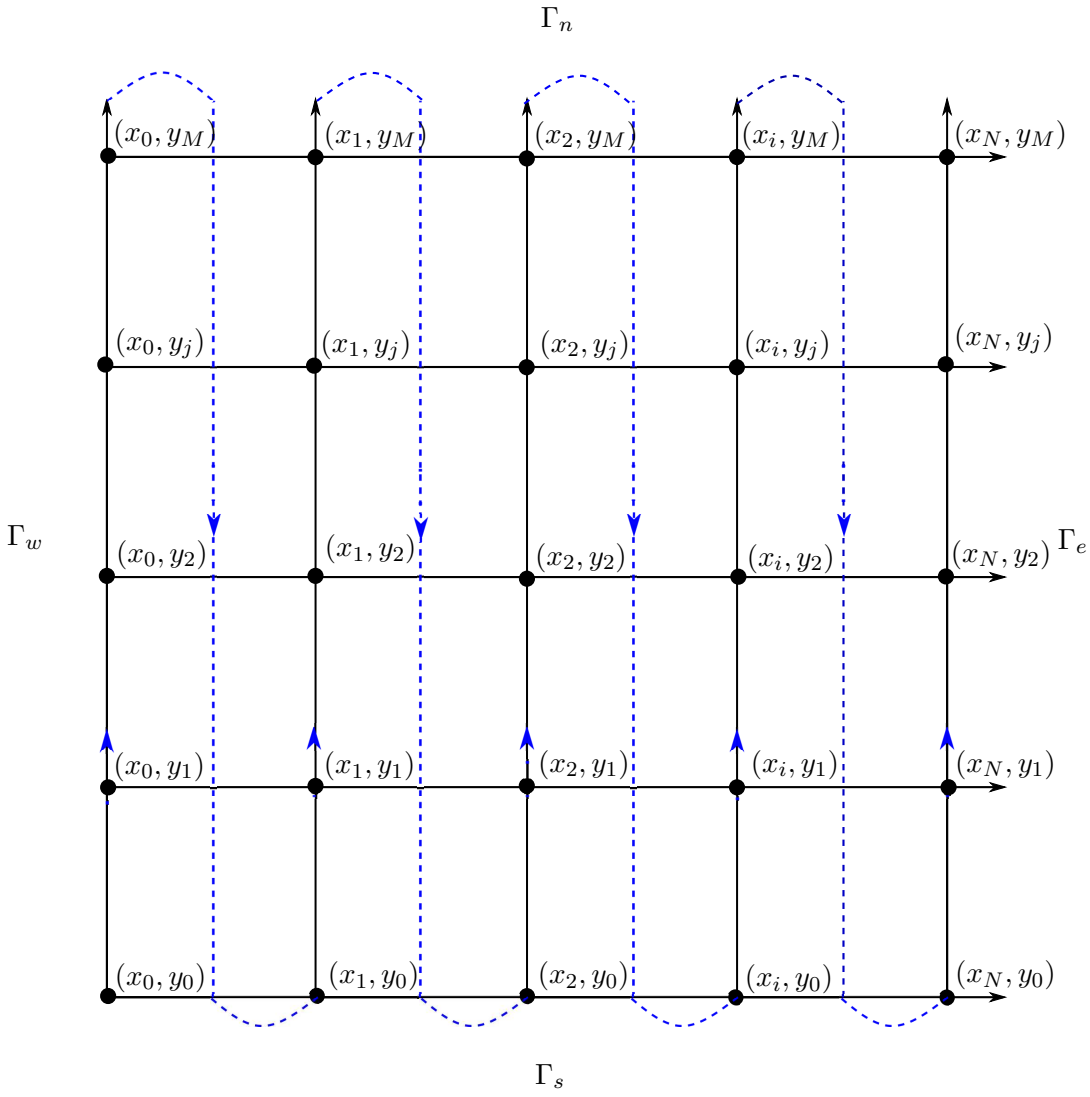

Figure 2.1: A schematic representation of the discretized domain using equidistant Cartesian grid. The grid points are denoted by black *dots* while the dotted lines show the columnwise orientation.

where subscripts x, y, respectively denote the operators acting in the x- and y-directions. Similar to the 1D case, $\mathbf{P} = \mathbf{P}^\mathsf{T} > 0$ in (2.31a) defines the 2D discrete norm $||\mathbf{w}||_\mathbf{P}^2 = \mathbf{w}^\mathsf{T}\mathbf{P}\mathbf{w} \approx$

$\iint_\Omega w^2 dxdy$. The 2D versions of Q_x, Q_y may be obtained respectively by multiplying $\mathbf{D}_x$, $\mathbf{D}_y$ in (2.31a) with $\mathbf{P}$

$$\mathbf{PD}_x = (Q_x \otimes P_y) = \mathbf{Q}_x, \quad \mathbf{PD}_y = (P_x \otimes Q_y) = \mathbf{Q}_y. \tag{2.31b}$$

Further, they satisfy the SBP property

$$\begin{aligned} \mathbf{Q}_x + \mathbf{Q}_x^\mathsf{T} &= (Q_x + Q_x^\mathsf{T}) \otimes P_y = (E_0 - E_N) \otimes P_y, \\ \mathbf{Q}_y + \mathbf{Q}_y^\mathsf{T} &= P_x \otimes (Q_y + Q_y^\mathsf{T}) = P_x \otimes (E_M - E_0)\,, \end{aligned} \tag{2.31c}$$

where the matrices $E_0 = \mathrm{diag}(1, 0, \ldots, 0)$, $E_N = \mathrm{diag}(0, \ldots, 0, 1)$, $E_M = \mathrm{diag}(0, \ldots, 0, 1)$ with appropriate sizes restrict the solution to the boundary points. Further, the matrices (2.31c) are the boundary quadrature rules approximating the continuous boundary line integral i.e. $\mathbb{P} \approx \oint_\Gamma (\cdot) ds$ in 2D where

$$\mathbb{P}_k = \begin{cases} P_x \otimes E_M & \text{north boundary}, \\ P_x \otimes E_0 & \text{south boundary}, \\ E_N \otimes P_y & \text{east boundary}, \\ E_0 \otimes P_y & \text{west boundary}. \end{cases} \tag{2.31d}$$

2.8 SBP operators on curvilinear domains

The finite difference operators on SBP form (2.20) are designed for equispaced rectangular meshes. They can however be extended to curvilinear meshes using a coordinate transformation [67–71]. Thus, an IBVP is mapped onto an isometric configuration which leads to tedious and convoluted discrete formulations. To overcome this, a framework that encapsulates the transformation metrics into the SBP operators was introduced in [70, 71]. To demonstrate this, we follow [70] closely. Consider a curvilinear domain Ω with coordinates $(x, y) = (x(\xi, \eta), y(\xi, \eta))$ and boundary Γ. Moreover, $(\xi, \eta) = [0, 1]^2$ are the coordinates of the isometric domain $\widehat{\Omega}$, with boundary $\widehat{\Gamma}$ as depicted in Figure 2.2. The mapping between Ω and $\widehat{\Omega}$ is facilitated by the coordinate transformation $(x, y) \mapsto (\xi, \eta)$ with the invertible Jacobian matrix

$$\frac{\partial(x, y)}{\partial(\xi, \eta)} = \begin{bmatrix} x_\xi & x_\eta \\ y_\xi & y_\eta \end{bmatrix}, \quad \mathsf{J} = \det\left(\frac{\partial(x, y)}{\partial(\xi, \eta)}\right) = x_\xi y_\eta - x_\eta y_\xi > 0, \tag{2.32}$$

where subscripts ξ, η denote the partial derivatives. Similarly, the reverse map is given by $(\xi, \eta) \mapsto (x, y)$ with the Jacobian matrix

$$\frac{\partial(\xi, \eta)}{\partial(x, y)} = \begin{bmatrix} \xi_x & \xi_y \\ \eta_x & \eta_y \end{bmatrix}. \tag{2.33}$$

The Jacobian matrices (2.32) and (2.33) are related by the *inverse function theorem* which states that for some invertible function f, the Jacobain matrix of f^{-1} is equal to the inverse of the Jacobian matrix of f. That is

$$\frac{\partial(\xi, \eta)}{\partial(x, y)} = \left(\frac{\partial(x, y)}{\partial(\xi, \eta)}\right)^{-1} \quad \Rightarrow \quad \begin{bmatrix} \xi_x & \xi_y \\ \eta_x & \eta_y \end{bmatrix} = \frac{1}{\mathsf{J}} \begin{bmatrix} y_\eta & -x_\eta \\ -y_\xi & x_\xi \end{bmatrix}, \tag{2.34}$$

where the determinant J is given in (2.32). Further, equating the matrix entries in (2.34) leads to the so-called metric relations

$$\xi_x = \mathsf{J}^{-1} y_\eta, \quad \xi_y = -\mathsf{J}^{-1} x_\eta, \quad \eta_x = -\mathsf{J}^{-1} y_\xi, \quad \eta_y = \mathsf{J}^{-1} x_\xi. \tag{2.35}$$

Lastly, for any integrable function g, the following relation holds

$$\int_{\Omega} g(x,y)dxdy = \int_{\widehat{\Omega}} \mathsf{J} g(x(\xi,\eta), y(\xi,\eta))d\xi d\eta. \tag{2.36}$$

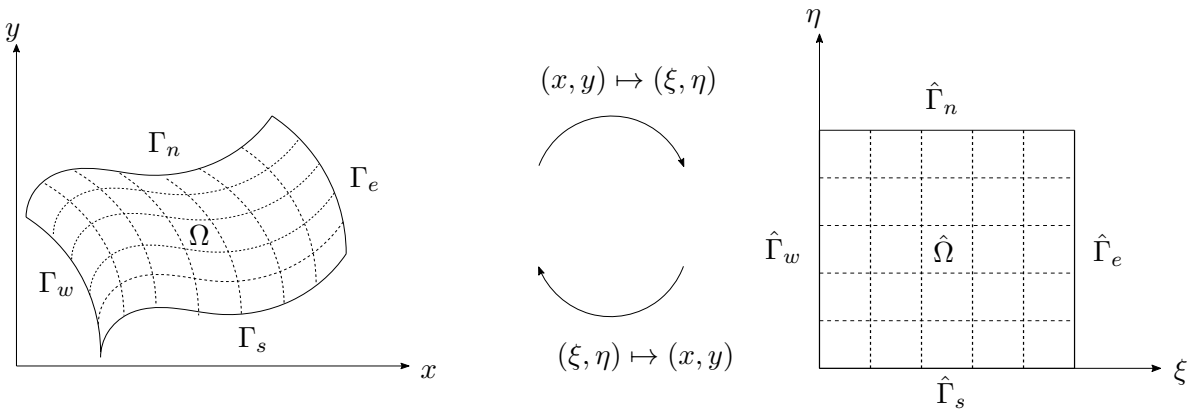

Figure 2.2: The illustration of the coordinate transformation between the curvilinear and isometric domains.

2.8.1 Coordinate transformation

To demonstrate the coordinate transformation for a PDE, let's consider a 2D linear advection problem with constant coefficients defined on some curved domain Ω

$$w_t + aw_x + bw_y = 0, \quad (x,y) \in \Omega, \quad t \geq 0, \tag{2.37}$$

where $a, b > 0$. The energy method applied to (2.37) yields

$$\frac{d}{dt}||w||^2 = -\oint (an_x + bn_y)w^2 ds, \tag{2.38}$$

where n_x, n_y denote the components of the unit outward pointing normal vectors on Ω. We will define them for curved domains later. An energy estimate exists for (2.37) if $an_x + bn_y \geq 0$ in (2.38). At boundaries where this is not the case, then appropriate boundary conditions must be imposed. The PDE (2.37) can be transformed to a square domain $\widehat{\Omega}$ using the chain rule for differentiation. Starting with the partial derivatives

$$\frac{\partial}{\partial x} w(\xi(x,y),\eta(x,y)) = w_\xi \xi_x + w_\eta \eta_x, \quad \frac{\partial}{\partial y} w(\xi(x,y),\eta(x,y)) = w_\xi \xi_y + w_\eta \eta_y, \tag{2.39}$$

and using the metric relations (2.35), w_x and w_y can be rewritten in terms of the isometric derivatives as

$$w_x = \mathsf{J}^{-1}(y_\eta w_\xi - y_\xi w_\eta), \; w_y = \mathsf{J}^{-1}(x_\xi w_\eta - x_\eta w_\xi). \tag{2.40}$$

Therefore, (2.37) with (2.40) becomes

$$w_t + \mathsf{J}^{-1}\left(\widehat{a}w_\xi + \widehat{b}w_\eta\right) = 0, \quad (\xi,\eta) \in \widehat{\Omega}, \quad t \geq 0, \tag{2.41}$$

where $\widehat{a} = ay_\eta - bx_\eta$ and $\widehat{b} = bx_\xi - ay_\xi$ are the new variable coefficients. For the purpose of the upcoming stability analysis, these coefficients must be written as an average of the conservative and non-conservative forms [72]. The flux splitting technique [32, 72, 73] leads to

$$\widehat{a}w_\xi = \frac{1}{2}\left((\widehat{a}w)_\xi + \widehat{a}w_\xi - \widehat{a}_\xi w\right), \quad \widehat{b}w_\eta = \frac{1}{2}\left((\widehat{b}w)_\eta + \widehat{b}w_\eta - \widehat{b}_\eta w\right). \tag{2.42}$$

By further noting that $\widehat{a}_\xi + \widehat{b}_\eta = a(y_{\eta\xi} - y_{\xi\eta}) + b(x_{\xi\eta} - x_{\eta\xi}) = 0$ (since $\partial_{\xi\eta}(\cdot) = \partial_{\eta\xi}(\cdot)$), (2.41) becomes

$$w_t + \frac{1}{2}\mathsf{J}^{-1}\left((\widehat{a}w)_\xi + \widehat{a}w_\xi + (\widehat{b}w)_\eta + \widehat{b}w_\eta\right). \tag{2.43}$$

Lastly, the unit outward pointing vectors on the curved and isometric domains are

$$\hat{\mathbf{n}}^n = \frac{1}{\sqrt{x_\xi^2 + y_\xi^2}}\begin{pmatrix} -y_\xi \\ x_\xi \end{pmatrix}, \qquad \mathbf{n}^n = \begin{pmatrix} 0 \\ 1 \end{pmatrix},$$

$$\hat{\mathbf{n}}^s = \frac{1}{\sqrt{x_\xi^2 + y_\xi^2}}\begin{pmatrix} y_\xi \\ -x_\xi \end{pmatrix}, \qquad \mathbf{n}^s = \begin{pmatrix} 0 \\ -1 \end{pmatrix},$$

$$\hat{\mathbf{n}}^e = \frac{1}{\sqrt{x_\eta^2 + y_\eta^2}}\begin{pmatrix} y_\eta \\ -x_\eta \end{pmatrix}, \qquad \mathbf{n}^e = \begin{pmatrix} 1 \\ 0 \end{pmatrix},$$

$$\hat{\mathbf{n}}^w = \frac{1}{\sqrt{x_\eta^2 + y_\eta^2}}\begin{pmatrix} -y_\eta \\ x_\eta \end{pmatrix}, \qquad \mathbf{n}^w = \begin{pmatrix} -1 \\ 0 \end{pmatrix}.$$

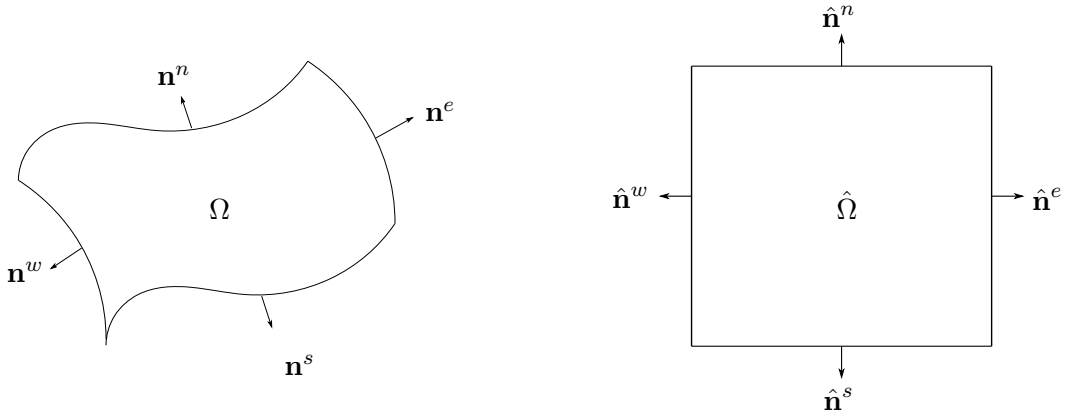

Figure 2.3: The illustration of the 2D curved and isometric domains including the outward pointing unit normal vectors.

2.8.2 Encapsulated SBP operators on curvilinear meshes

To present the semi-discrete approximation of (2.43), we consider an isometric domain $\widehat{\Omega} = [0,1]^2$ and discretize it with $(N+1) \times (M+1)$ equidistant Cartesian grid coordinates (ξ_i, η_i). Let

$\mathbf{x}$, $\mathbf{y}$ be the vectors containing the coordinates (x_{ij}, y_{ij}) of the discretized physical domain $\widehat{\Omega}$ where $x_{ij} = x(\xi_i, \eta_j)$ and $y_{ij} = y(\xi_i, \eta_j)$. We denote the approximation vector of (2.43) with an $(N+1)(M+1) \times 1$ vector $\mathbf{w}$, arranged in a columnwise orientation (see Figure 2.1). To approximate the continuous derivatives, we employ the 2D SBP operators (2.31a)

$$\mathbf{D}_\xi = P_\xi^{-1} Q_\xi \otimes \mathbf{I}_\eta, \quad \mathbf{D}_\eta = \mathbf{I}_\xi \otimes P_\eta^{-1} Q_\eta, \tag{2.44}$$

where the subscripts ξ, η are used to distinguish the operators acting on the ξ and η directions. Further, $\mathbf{I}_\xi$, $\mathbf{I}_\eta$ are the unit matrices with appropriate sizes. Next, we compute the partial derivatives in (2.39) as

$$\mathbf{X}_\xi = \text{diag}(\mathbf{D}_\xi \mathbf{x}), \quad \mathbf{Y}_\xi = \text{diag}(\mathbf{D}_\xi \mathbf{y}), \quad \mathbf{X}_\eta = \text{diag}(\mathbf{D}_\eta \mathbf{x}), \quad \mathbf{Y}_\eta = \text{diag}(\mathbf{D}_\eta \mathbf{y}), \tag{2.45}$$

and subsequently the discrete version of J in (2.32) as

$$\mathbf{J} = \mathbf{X}_\xi \mathbf{Y}_\eta - \mathbf{X}_\eta \mathbf{Y}_\xi, \tag{2.46}$$

Therefore, diagonal norm approximating the continuous integral (2.36) is

$$\mathbf{P}_{\xi\eta} = \mathbf{J}(P_\xi \otimes P_\eta). \tag{2.47}$$

The semi-discrete formulation of (2.41) becomes

$$\mathbf{w}_t + \frac{1}{2}\mathbf{J}^{-1}\left(\mathbf{D}_\xi \mathsf{A}\mathbf{w} + \mathsf{A}\mathbf{D}_\xi \mathbf{w} + \mathbf{D}_\eta \mathsf{B}\mathbf{w} + \mathsf{B}\mathbf{D}_\eta \mathbf{w}\right) = \mathsf{SAT}, \tag{2.48}$$

where $\mathsf{A} = a\mathbf{Y}_\eta - b\mathbf{X}_\eta$, $\mathsf{B} = b\mathbf{X}_\xi - a\mathbf{Y}_\xi$ are the discrete analogues of $\widehat{a}$, $\widehat{b}$ in (2.41), and SAT denotes the weakly imposed boundary conditions. Further, we can rearrange (2.48) and rewrite it in compact form as

$$\mathbf{w}_t + a\mathcal{D}_x \mathbf{w} + b\mathcal{D}_y \mathbf{w} = \mathsf{SAT}, \tag{2.49}$$

where

$$\mathcal{D}_x = \frac{1}{2}\mathbf{J}^{-1}(\mathbf{D}_\xi \mathbf{Y}_\eta + \mathbf{Y}_\eta \mathbf{D}_\xi - \mathbf{D}_\eta \mathbf{Y}_\xi - \mathbf{Y}_\xi \mathbf{D}_\eta),$$
$$\mathcal{D}_y = \frac{1}{2}\mathbf{J}^{-1}(\mathbf{D}_\eta \mathbf{X}_\xi + \mathbf{X}_\xi \mathbf{D}_\eta - \mathbf{D}_\xi \mathbf{X}_\eta - \mathbf{X}_\eta \mathbf{D}_\xi).$$

In (2.49), $\mathcal{D}_x$, $\mathcal{D}_y$ are called the encapsulated SBP operators [70], which *red*comes from the fact that they incorporate the coordinate transformations. Furthermore, it can be shown they satisfy the SBP property (2.31c). These operators can be applied to curved domains directly. Next, we apply the energy method to (2.49) to obtain the energy rate

$$\frac{d}{dt}||\mathbf{w}||^2_{\mathbf{PJ}} = \mathbf{w}^\mathsf{T}\mathbf{P}_w\mathbf{A}\mathbf{w} - \mathbf{w}^\mathsf{T}\mathbf{P}_e\mathbf{A}\mathbf{w} + \mathbf{w}^\mathsf{T}\mathbf{P}_s\mathbf{B}\mathbf{w} - \mathbf{w}^\mathsf{T}\mathbf{P}_n\mathbf{B}\mathbf{w} + 2\mathbf{w}^\mathsf{T}\mathbf{P}\mathsf{SAT}, \tag{2.50}$$

where the discrete boundary quadrature $\mathbf{P}_{n,s,e,w}$ imitate $\oint_{\widehat{\Omega}}(\cdot)d\hat{s}$

$$\mathbf{P}_k = \begin{cases} (P_\xi \otimes E_{1\eta})\sqrt{\boldsymbol{X}_\xi^2 + \boldsymbol{Y}_\xi^2} & \text{north boundary,} \\ (P_\xi \otimes E_{0\eta})\sqrt{\boldsymbol{X}_\xi^2 + \boldsymbol{Y}_\xi^2} & \text{south boundary} \\ (E_{1\xi} \otimes P_\eta)\sqrt{\boldsymbol{X}_\eta^2 + \boldsymbol{Y}_\eta^2} & \text{east boundary,} \\ (E_{0\xi} \otimes P_\eta)\sqrt{\boldsymbol{X}_\eta^2 + \boldsymbol{Y}_\eta^2} & \text{west boundary.} \end{cases} \tag{2.51}$$

The penalty terms in (2.50) must be defined such that they cancel growth terms and the energy rate is non-positive.

Chapter 3

Incompressible flow

This chapter presents the flow governing equations used in this study. The flow under consideration is incompressible and laminar. The incompressisble Navier-Stokes equations are used as an original model to the problem, from which the laminar boundary layer equations are derived using the dimensional analysis technique.

3.1 Incompressible Navier-Stokes equations

Fluids are characterized by a tendency to deform continuously when subjected to a shear force, and due to molecular interactions. The fluid dynamical macroscopic properties such as density, velocity, and pressure can be associated to an infinitesimal volume of fluid, enabling fluid flows to be considered continuous media. This phenomenon is also known as the continuum hypothesis. The rheology of fluids is better explained using the conservation laws, and mathematically, these are space-time coupled partial differential equations. In this study, the INS model for viscous Newtonian fluids [4] under isothermal conditions is considered. In 2D, this model consists of the conservation of mass and momentum equations

$$\frac{\partial \rho}{\partial t} + \nabla \cdot (\rho \mathbf{u}) = 0, \tag{3.1a}$$

$$\rho \frac{\partial \mathbf{u}}{\partial t} + \rho \mathbf{u} \cdot \nabla \mathbf{u} = \nabla \cdot \tau + \rho \mathbf{f}, \tag{3.1b}$$

where ρ is the fluid density and is assumed constant, $\nabla = (\frac{\partial}{\partial x}, \frac{\partial}{\partial y})^\mathsf{T}$ is the spatial gradient operator, $\mathbf{u} = (u, v)^\mathsf{T}$ is the velocity vector field, and $\rho\mathbf{f}$ is the body force. The second-order tensor τ denotes the total stress in the fluid and it is defined as

$$\tau = -p\mathbf{I} + \mathbf{D}, \tag{3.2}$$

where p is the pressure, $\mathbf{I}$ is an identity matrix, and $\mathbf{D}$ is the deformation rate tensor. For Newtonian fluids, stress varies linearly with strain rate [4]. Therefore, the deformation rate tensor consisting of the fluid's strain rate $\mathbf{S}$ reads

$$\mathbf{D} = 2\mu\mathbf{S}, \quad \text{where} \quad \mathbf{S} = \frac{1}{2}(\nabla\mathbf{u} + (\nabla\mathbf{u})^\mathsf{T}), \tag{3.3}$$

and μ is a coefficient of dynamic viscosity.

Equation (3.1) consists of three equations and three unknowns namely, p, u, and v. Due to $\nabla \cdot \mathbf{u} = 0$, (3.1) can be rewritten in the absence of a body force as

$$\frac{\partial u}{\partial t} + u\frac{\partial u}{\partial x} + v\frac{\partial u}{\partial y} = -\frac{1}{\rho}\frac{\partial p}{\partial x} + \nu\left(\frac{\partial^2 u}{\partial x^2} + \frac{\partial^2 u}{\partial y^2}\right), \tag{3.4a}$$

$$\frac{\partial v}{\partial t} + u\frac{\partial v}{\partial x} + v\frac{\partial v}{\partial y} = -\frac{1}{\rho}\frac{\partial p}{\partial y} + \nu\left(\frac{\partial^2 v}{\partial x^2} + \frac{\partial^2 v}{\partial y^2}\right), \tag{3.4b}$$

$$\frac{\partial u}{\partial x} + \frac{\partial v}{\partial y} = 0, \tag{3.4c}$$

where $\nu = \frac{\mu}{\rho}$ is the kinematic viscosity. The system of equations (3.4) is known as the INS equations under isothermal condition with no body force.

3.2 Incompressible boundary layer equations

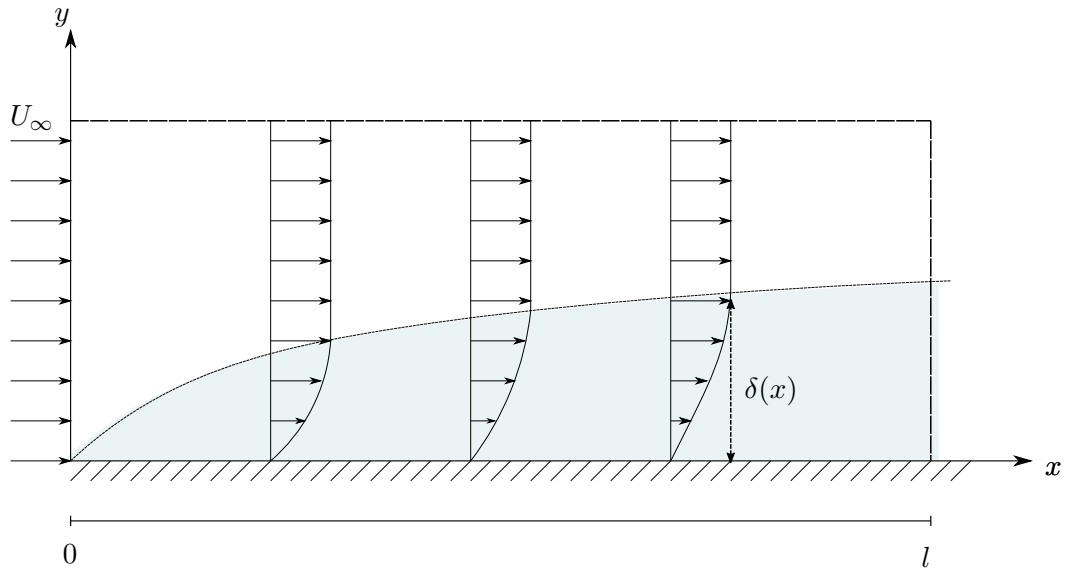

Figure 3.1: Viscous fluid flowing over a thin plate of length l at uniform speed U_∞ leads to the formation of a boundary layer.

Laminar, viscous flow past a solid surface can be divided into two flow regimes. The first resides in the immediate vicinity of the solid surface where viscous effects are so prevalent that they rapidly reduce the flow velocity to zero (so-called no-slip boundary condition). This region is known as the boundary layer. The second regime occurs in the outer flow where viscous effects are insignificant. The boundary layer forms on the plate's surface and its thickness is denoted by $\delta(x)$. This is a normal distance from the plate to a point in the fluid where the flow velocity is 99% of the freestream speed. Further, it grows as a function of distance from the plate's leading edge as shown in Figure 3.1. In the case where the Reynolds number $\mathrm{Re} = \frac{U_\infty l}{\nu} \gg 1$, $\delta(x) \ll l$, resulting in the transverse scales being significantly less than the streamwise scales. This leads to

$$\frac{u}{U_\infty}, \frac{x}{l} \sim \mathcal{O}(1), \quad \frac{v}{U_\infty}, \frac{y}{l} \sim \mathcal{O}(\sqrt{\mathrm{Re}})^{-1}, \tag{3.5}$$

which can be used to define the following dimensionless quantities

$$x^* = \frac{x}{l}, \quad y^* = \frac{y}{l}\sqrt{\mathrm{Re}}, \quad t^* = \frac{tU_\infty}{l}, \quad u^* = \frac{u}{U_\infty}, \quad v^* = \frac{v}{U_\infty}\sqrt{\mathrm{Re}}, \quad p^* = \frac{p}{\rho U_\infty^2}. \tag{3.6}$$

Substituting (3.6) into (3.4) yields

$$\begin{aligned} \frac{\partial u^*}{\partial t^*} + u^*\frac{\partial u^*}{\partial x^*} + v^*\frac{\partial u^*}{\partial y^*} &= -\frac{\partial p^*}{\partial x^*} + \left(\frac{1}{\mathrm{Re}}\frac{\partial^2 u^*}{\partial x^{*2}} + \frac{\partial^2 u^*}{\partial y^{*2}}\right), \\ \frac{1}{\mathrm{Re}}\left(\frac{\partial v^*}{\partial t^*} + u^*\frac{\partial v^*}{\partial x^*} + v^*\frac{\partial v^*}{\partial y^*}\right) &= -\frac{\partial p^*}{\partial y^*} + \frac{1}{\mathrm{Re}^2}\left(\frac{\partial^2 v^*}{\partial x^{*2}} + \frac{\partial^2 v^*}{\partial y^{*2}}\right), \\ \frac{\partial u^*}{\partial x^*} + \frac{\partial v^*}{\partial y^*} &= 0, \end{aligned} \tag{3.7}$$

where the superscripts $*$ denotes the dimensionless quantities. For $\mathrm{Re} \gg 1$, most of the terms in (3.7) become insignificant and the system of equations reduces (dropping $*$) to

$$\frac{\partial u}{\partial t} + u\frac{\partial u}{\partial x} + v\frac{\partial u}{\partial y} = -\frac{\partial p}{\partial x} + \frac{\partial^2 u}{\partial y^2}, \tag{3.8a}$$

$$0 = -\frac{\partial p}{\partial y}, \tag{3.8b}$$

$$\frac{\partial u}{\partial x} + \frac{\partial v}{\partial y} = 0. \tag{3.8c}$$

Equations (3.8) are called the incompressible boundary layer equations (IBL) [74] and they only hold for significantly large Re that still maintains laminar flow. Furthermore, all the terms in (3.8) are $\mathcal{O}(1)$. Note that the mass conservation equation (3.8c) remains invariant to non-dimensionalisation. From (3.8b), the pressure variation in the y-direction is insignificant and negligible. Thus, the pressure is a function of x only and it is related to the flow's freestream velocity through Bernoulli's equation [75]

$$p + \frac{1}{2}\rho U_\infty^2 = c, \quad \Rightarrow \quad \frac{\partial p}{\partial x} = -\rho U_\infty \frac{\partial U_\infty}{\partial x}, \tag{3.9}$$

where c is a constant.

The flow above was aligned to the solid surface, it can however be generalised to any angle by setting $U_\infty = x^m$, where $m = \frac{\beta}{2\pi - \beta}$ uniquely defines the flow configuration and β is the angle between the wall and the inflow. For example, $\beta = 0$, $m = 0$ corresponds to the Blasius boundary layer while $\beta = \pi$, $m = 1$ corresponds to Hiemenz stagnation flow as illustrated in Figure 3.2 [74]. Note that for the Blasius boundary layer, $\frac{\partial p}{\partial x} = 0$ in (3.8a) as a result of $U_\infty = 1$. We however keep U_∞ general. The steady version of (3.8) is

$$\begin{aligned} u\frac{\partial u}{\partial x} + v\frac{\partial u}{\partial y} &= \rho U_\infty \frac{\partial U_\infty}{\partial x} + \frac{\partial^2 u}{\partial y^2}, \\ \frac{\partial u}{\partial x} + \frac{\partial v}{\partial y} &= 0. \end{aligned} \tag{3.10}$$

The missing terms in (3.8) indicate that the new simplified system of governing equations requires less boundary conditions compared to the original model (3.4). We will explore this in Chapter 4 where we will be deriving a new set of provably stable boundary conditions specific to (3.8).

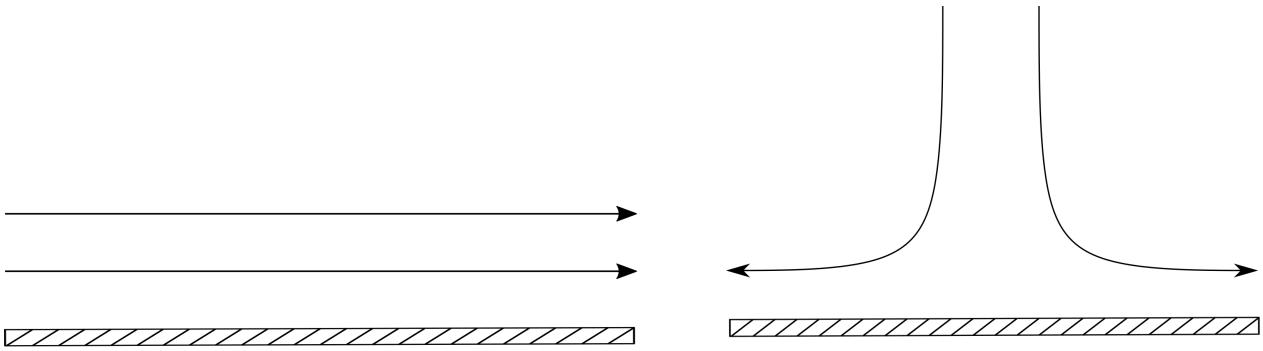

(a) $\beta = 0$, $m = 0$ (b) $\beta = \pi$, $m = 1$

Figure 3.2: Schematic representation of different freestream velocity, (a) Blasius boundary layer and (b) Hiemenz stagnation flow.

The similarity solution of (3.10) exits (see Appendix B) and will be used to validate the upcoming discrete approximation.

3.3 Concluding remarks

To summarize the above, we started with the INS equations and derived the boundary layer equations using dimensional analysis. Specifically, we considered viscous fluid flowing past an infinitely thin plate. For $\mathrm{Re} \gg 1$, several terms in the momentum equations may be assumed insignificant while the continuity equation remains the same. Of note, the new set of equations is likely to require less boundary conditions. The similarity solution for these equations is presented in Appendix B. In Chapter 4, we will construct a continuous initial-boundary value problem for (3.10) which is fundamentally important for the development of the approximation solution of the IBL equations.

Chapter 4

Stable boundary conditions for the IBL equations

In this chapter, we consider the continuous analysis of the incompressible laminar boundary layer equations. Our aim is to construct an energy stable continuous problem which fundamentally depends on the choice of boundary conditions. Therefore, we begin the analysis by deriving the conditions that lead to a bounded energy estimate using the energy method. This is done for both strong and weak boundary condition imposition. We then derive the precise weak and strong boundary conditions which lead to an energy estimate for the boundary layer equations.

4.1 Derivation of conditions for energy stability

To set up an initial-boundary value problem for the analysis, we consider a rectangular domain Ω with boundary Γ. The plate is positioned along the x-axis such that it aligns with the south boundary and the leading edge is at the origin as depicted in Figure 3.1. The north boundary is positioned at the far-field where the flow is almost inviscid. Since we are considering the right-going flow as illustrated in Figure 3.1, the west boundary is the inflow while the east boundary is the outflow.

We augment (3.8) with initial and boundary conditions, and write the resulting IBVP in matrix-vector notation as

$$\bar{I}\mathrm{U}_t + A\mathrm{U}_x + B\mathrm{U}_y - \nu\bar{I}\mathrm{U}_{yy} = 0, \quad (x,y) \in \Omega, \quad t > 0, \tag{4.1a}$$

$$H\mathrm{U} = \mathbf{g}, \quad (x,y) \in \Gamma, \quad t \geq 0, \tag{4.1b}$$

$$\bar{I}\mathrm{U} = \mathbf{f}, \quad (x,y) \in \Omega, \quad t = 0, \tag{4.1c}$$

where

$$A = \begin{bmatrix} u & 0 & 1 \\ 0 & 0 & 0 \\ 1 & 0 & 0 \end{bmatrix}, \quad B = \begin{bmatrix} v & 0 & 0 \\ 0 & 0 & 1 \\ 0 & 1 & 0 \end{bmatrix}, \quad \text{and} \quad \bar{I} = \begin{bmatrix} 1 & 0 & 0 \\ 0 & 0 & 0 \\ 0 & 0 & 0 \end{bmatrix}.$$

The vector $\mathrm{U} = [u, v, p]^\mathsf{T}$ is a solution vector containing the horizontal and vertical components of the velocity, the pressure, ν which is the viscous coefficient. The boundary operator H in (4.1b) and its exact form is not specified yet while $\mathbf{g}$, $\mathbf{f}$ are continuous functions specifying boundary and initial data, respectively. Moreover, we assume that all data is available and compatible

such that a sufficiently smooth solution of (4.1) exists. In (4.1c), the initial condition is only imposed on u because it is the only flow variable with a temporal term. Therefore, $\mathbf{f}$ has the form $\mathbf{f} = [f, 0, 0]^\mathsf{T}$ where $f = f(x, y)$ is a continuous function. We devote the first part of this analysis to determining H such that (4.1b) leads to an energy bounded estimate. For this purpose, we follow the guideline for constructing a well-posed continuous problem provided in [18] and further exemplified on the fully incompressible Navier-Stokes equations in [31, 32], Euler's equations [76] and the shallow water equations [35]. We summarize the key steps in Figure 4.1 which will be mimicked in the upcoming discrete analysis to develop a provably stable approximation of (4.1).

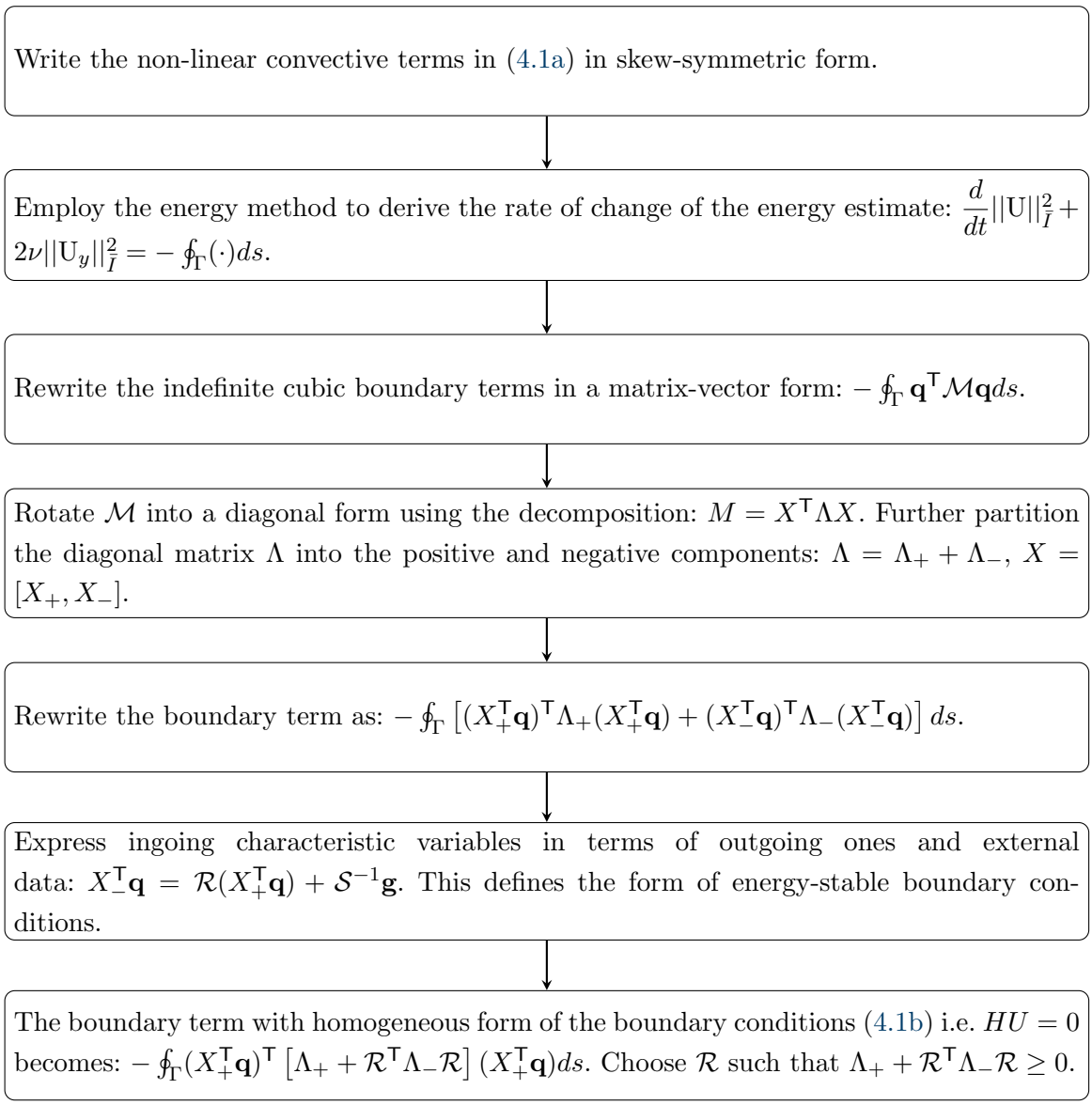

Figure 4.1: Schematic flow diagram for constructing energy bounded continuous problem. Once the energy-stable boundary conditions are obtained, leading to a bounded energy rate, a similar process is mimicked in the discrete setting to construct a stable approximation.

The analysis begins by transforming the primitive form of (4.1a) into skew-symmetric form using the flux splitting technique [32, 72, 73]. This step is necessary in the upcoming discrete

analysis when using the SBP properties in Definition 2.3. We first consider the x-convective terms and write them as a linear combination of the conservative and non-conservative parts

$$A\mathrm{U}_x = \alpha(A\mathrm{U})_x + (1-\alpha)A\mathrm{U}_x - \alpha A_x\mathrm{U}, \tag{4.2}$$

where α is a real constant. By applying a similar splitting technique to the y-convective terms in (4.1a) and making the choice $\alpha = 1/2$ [32], the nonlinear convective terms in (4.1a) transform to

$$A\mathrm{U}_x = \frac{1}{2}(A\mathrm{U})_x + \frac{1}{2}A\mathrm{U}_x - \frac{1}{2}A_x\mathrm{U}, \quad B\mathrm{U}_y = \frac{1}{2}(B\mathrm{U})_y + \frac{1}{2}B\mathrm{U}_y - \frac{1}{2}B_y\mathrm{U}. \tag{4.3}$$

Therefore, substituting (4.3) into (4.1a) yields the skew-symmetric form of the IBL equations which reads

$$\bar{I}\mathrm{U}_t + \mathcal{D}(\mathrm{U})\mathrm{U} = 0, \tag{4.4}$$

where

$$\mathcal{D}(\mathrm{U})\mathrm{U} = \frac{1}{2}\left[(A\mathrm{U})_x + A\mathrm{U}_x + (B\mathrm{U})_y + B\mathrm{U}_y\right] - \nu\bar{I}\mathrm{U}_{yy},$$

is the spatial operator. Moreover, this is the form we will be working with in the subsequent analysis. Further, note that $A_x + B_y = (u_x + v_y)\bar{I} = 0$ using the divergence relation (3.8c).

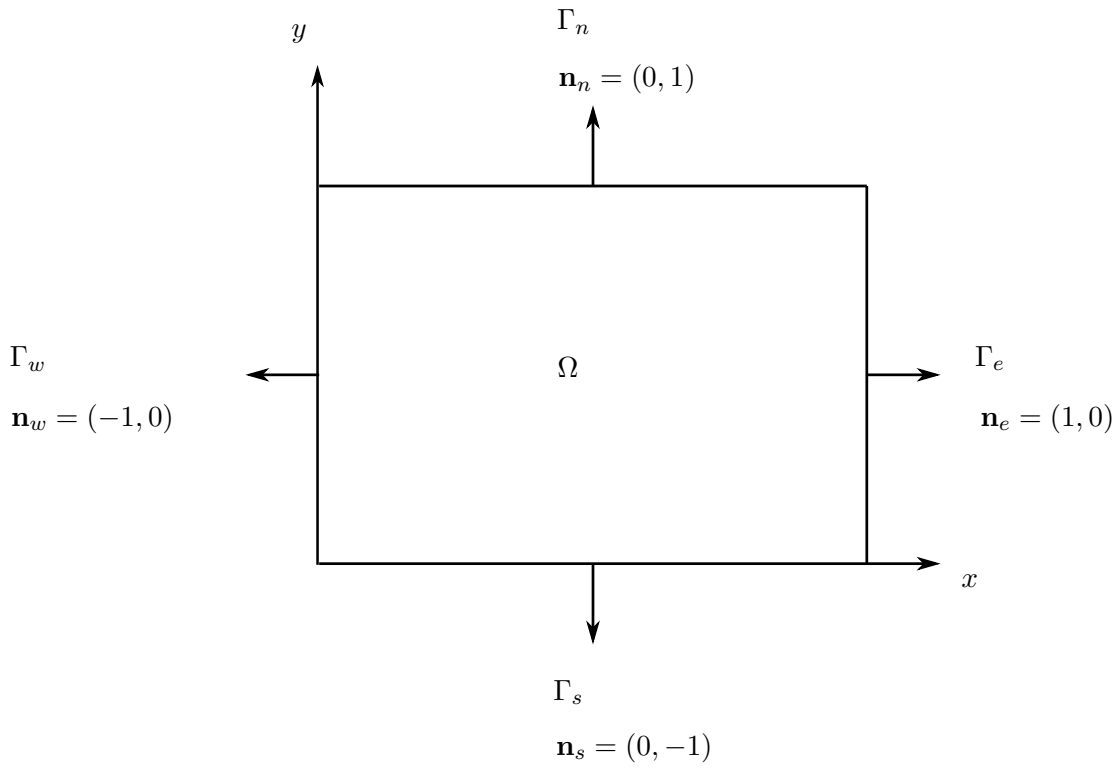

Figure 4.2: The illustration of a regular 2D domain with outward pointing boundary normal vectors.

We reiterate that herein, we do not modify the divergence relations with the density/pressure augmentation techniques mentioned before in Chapter 1. Instead, we determine energy stable

boundary conditions (4.1b) such that their correct implementation in the discrete setting remove the singularities associated with the incompressibility constraint [77] while leading to a discrete bounded energy estimate.

The energy method applied to (4.4) yields

$$\int_{\Omega} \mathrm{U}^{\mathsf{T}} \bar{I} \mathrm{U} d\Omega + \int_{\Omega} \left[\mathrm{U}^{\mathsf{T}} (A\mathrm{U})_x + \mathrm{U}^{\mathsf{T}} A \mathrm{U}_x + \mathrm{U}^{\mathsf{T}} (B\mathrm{U})^{\mathsf{T}} + \mathrm{U}^{\mathsf{T}} B \mathrm{U}_y - 2\nu \mathrm{U}^{\mathsf{T}} \bar{I} \mathrm{U}_{yy} \right] d\Omega = 0, \quad (4.5)$$

where $d\Omega = dxdy$ is the volume element. Let $||\mathrm{U}||_{\bar{I}}^2 = \int_{\Omega} \mathrm{U}^{\mathsf{T}} \bar{I} \mathrm{U} d\Omega$ be the L_2 semi-norm. By using Green's theorem to simplify the integrals in (4.5), we obtain the rate of change of the energy estimate

$$\frac{d}{dt} ||\mathrm{U}||_{\bar{I}}^2 + 2\nu ||\mathrm{U}_y||_{\bar{I}}^2 = \mathrm{BT}, \quad (4.6)$$

where BT denotes the indefinite boundary term

$$\mathrm{BT} = -\oint_{\Gamma} \left[\mathrm{U}^{\mathsf{T}} (An_x + Bn_y)\mathrm{U} - 2\nu \mathrm{U}^{\mathsf{T}} \bar{I} \mathrm{U}_y \right] ds = -\oint_{\Gamma} \left(u_{\mathbf{n}} u^2 + 2u_{\mathbf{n}} p - 2\nu u u_y n_y \right) ds.$$

In (4.6), $\oint_{\Gamma}(\cdot)ds$ is the boundary line integral with the infinitesimal line element $ds = \sqrt{dx^2 + dy^2}$. Further, $u_{\mathbf{n}} = un_x + vn_y$ denotes the boundary normal velocity where $\mathbf{n} = (n_x, n_y)$ is the outward pointing unit vector as shown in Figure 4.2. Equation (4.6) measures the rate of change of the solution which depends on the sign of BT. The trivial choice of setting $u = v = 0$ on the boundary such that the BT $= 0$ yields the desired results, however, it is restrictive (i.e. it is only applicable for no-slip boundary conditions).

Remark 4.1. *Equation (4.6) is an altered version of the energy rate of the fully incompressible Navier-Stokes equations [32]. We therefore follow closely the analysis therein to construct different bounds for BT in (4.6).*

We start by formulating the following Lemma.

Lemma 1. *The semi-norms $||U||_{\bar{I}}^2$ and $||U_y||_{\bar{I}}^2$ are bounded if $BT \leq 0$ in (4.6).*

Proof. Let's assume that $BT \leq 0$. The temporal integration of (4.6) over a finite time domain $[0, T]$ yields the energy estimate

$$||\mathrm{U}||_{\bar{I}}^2 \Big|_{t=T} + 2\nu \int_0^T ||\mathrm{U}_y||_{\bar{I}}^2 dt \leq ||\mathbf{f}||_{\bar{I}}^2,$$

which is bounded by initial data. □

Remark 4.2. *The bound is imposed only on the horizontal component of the velocity since it is the only flow variable in (4.1) with the temporal derivative. This is different compared to the incompressible Navier-Stokes equations where the vertical velocity is also bounded [32].*

4.1.1 Boundedness

The boundary term (BT) in (4.6) can potentially add growth to the energy rate. However, this growth can be limited with appropriate boundary conditions. To achieve this, we first write BT (4.6) in a matrix-vector notation as

$$\mathrm{BT} = -\oint_{\Gamma} \mathbf{q}^{\mathsf{T}} \mathcal{M} \mathbf{q} ds = -\oint_{\Gamma} \begin{bmatrix} u \\ v \\ p \\ \nu u_y \end{bmatrix}^{\mathsf{T}} \begin{bmatrix} u_n & 0 & n_x & -n_y \\ 0 & 0 & n_y & 0 \\ n_x & n_y & 0 & 0 \\ -n_y & 0 & 0 & 0 \end{bmatrix} \begin{bmatrix} u \\ v \\ p \\ \nu u_y \end{bmatrix} ds. \tag{4.7}$$

This form is convenient because we can now clearly see that $\mathrm{BT} \leq 0$ if and if only the matrix $\mathcal{M}$ is positive definite. In that case, the energy estimate follows from Lemma 1. To determine the signs of the eigenvalues of $\mathcal{M}$, we first state the following results.

Theorem 2 (Eigenvalue decomposition)**.** *Let K be an $n \times n$ matrix. If $K = K^{\mathsf{T}}$ then there exists an $n \times n$ orthogonal matrix J (i.e. $J^{-1} = J^{\mathsf{T}}$) such that $J^{-1}KJ = D$ where D is a diagonal matrix. Further, the elements of D are the eigenvalues of K [78].*

Therefore, since $\mathcal{M}$ in (4.7) is symmetric, we use the results above to decompose it as

$$X^{-1}\mathcal{M}X = \Lambda_{\mathcal{M}} \quad \Rightarrow \quad \mathcal{M} = X\Lambda_{\mathcal{M}}X^{\mathsf{T}}, \tag{4.8}$$

where $\Lambda_{\mathcal{M}}$ is a diagonal matrix containing the actual eigenvalues of $\mathcal{M}$. Further, matrix X is the associated orthogonal eigenvector matrix ($X^{-1} = X^{\mathsf{T}}$) whose columns are the linearly independent eigenvectors of $\mathcal{M}$.

Remark 4.3. *The matrix eigenvalue decomposition (4.8) is not the only choice to diagonalize $\mathcal{M}$ and subsequently determine the correct minimal number of boundary conditions required for energy boundedness. Matrix $\mathcal{M}$ can also be diagonalized using so-called matrix rotations. According to Sylvester's law of Inertia [79], the signs of the entries of the rotated matrix coincide with those of $\Lambda_{\mathcal{M}}$ in (4.8). This technique was applied to the incompressible Navier-Stokes equations in [32].*

Next, we determine the eigenvalues of $\mathcal{M}$ explicitly. This is achieved by formulating the eigenvalue problem $\mathcal{M}\mathbf{x} = \lambda\mathbf{x}$ and solving the characteristic polynomial

$$\det\left(\mathcal{M} - \lambda I_4\right) = \lambda^4 - u_{\mathbf{n}}\lambda^3 - (n_x^2 + 2n_y^2)\lambda^2 + u_{\mathbf{n}}n_y^2\lambda + n_y^4 = 0, \tag{4.9a}$$

where I_4 is a unit matrix of size 4. For the vertical boundaries with $n_x = \pm 1$ and $n_y = 0$ as depicted in Figure 4.2, (4.9a) simplifies to

$$\det(\mathcal{M} - \lambda I_4) = \lambda^2(\lambda^2 - u_{\mathbf{n}}\lambda - 1) = 0. \tag{4.9b}$$

Similarly, for horizontal boundaries with $n_x = 0$ and $n_y = \pm 1$, (4.9a) simplifies to

$$\det(\mathcal{M} - \lambda I_4) = (\lambda^2 - 1)(\lambda^2 - u_{\mathbf{n}}\lambda - 1) = 0. \tag{4.9c}$$

Here, the λ_i that solve (4.9) are called the eigenvalues of $\mathcal{M}$ and $\mathbf{x}_i$ are the associated eigenvectors. Since the characteristic polynomial for the horizontal boundaries (4.9b) differs from

the one for the vertical boundaries (4.9c), we will consider them separately. Starting with the horizontal boundaries, the λ_i that solve (4.9b) and the associated eigenvectors $\mathbf{x}_i$ are

$$\lambda_1 = \frac{u_\mathbf{n}}{2} - \sqrt{\left(\frac{u_\mathbf{n}}{2}\right)^2 + 1}, \quad \lambda_2 = -1, \quad \lambda_3 = +1, \quad \lambda_4 = \frac{u_\mathbf{n}}{2} + \sqrt{\left(\frac{u_\mathbf{n}}{2}\right)^2 + 1}, \tag{4.10a}$$

$$\mathbf{x}_1 = \begin{bmatrix} \lambda_1 \\ 0 \\ 0 \\ -n_y \end{bmatrix}, \quad \mathbf{x}_2 = \begin{bmatrix} 0 \\ 1 \\ -n_y \\ 0 \end{bmatrix}, \quad \mathbf{x}_3 = \begin{bmatrix} 0 \\ 1 \\ n_y \\ 0 \end{bmatrix}, \quad \mathbf{x}_4 = \begin{bmatrix} \lambda_4 \\ 0 \\ 0 \\ -n_y \end{bmatrix}.$$

Similarly for the east and west boundaries, the λ_i that solve (4.9c) and the associated eigenvectors are

$$\lambda_1 = \frac{u_\mathbf{n}}{2} - \sqrt{\left(\frac{u_\mathbf{n}}{2}\right)^2 + 1}, \quad \lambda_2 = 0, \quad \lambda_3 = 0, \quad \lambda_4 = \frac{u_\mathbf{n}}{2} + \sqrt{\left(\frac{u_\mathbf{n}}{2}\right)^2 + 1}, \tag{4.10b}$$

$$\mathbf{x}_1 = \begin{bmatrix} \lambda_1 \\ 0 \\ n_x \\ 0 \end{bmatrix}, \quad \mathbf{x}_2 = \begin{bmatrix} 0 \\ n_x \\ 0 \\ 0 \end{bmatrix}, \quad \mathbf{x}_3 = \begin{bmatrix} 0 \\ 0 \\ 0 \\ n_x \end{bmatrix}, \quad \mathbf{x}_4 = \begin{bmatrix} \lambda_4 \\ 0 \\ n_x \\ 0 \end{bmatrix}.$$

From (4.10), we can now explicitly write the eigenvalue and the normalized eigenvector matrices introduced in (4.8) for the north and south boundaries as

$$\Lambda_\mathcal{M} = \operatorname{diag}(\lambda_1, \lambda_2\lambda_3, \lambda_4), \tag{4.11a}$$

$$X = \mathfrak{N} \begin{bmatrix} \lambda_1 & 0 & 0 & \lambda_4 \\ 0 & 1 & 1 & 0 \\ 0 & -n_y & n_y & 0 \\ -n_y & 0 & 0 & -n_y \end{bmatrix}, \quad \mathfrak{N} = \operatorname{diag}\left(\sqrt{\lambda_1^2 + 1}, \sqrt{2}, \sqrt{2}, \sqrt{\lambda_4^2 + 1}\right)^{-1},$$

Similarly, for the east and west boundaries, they are

$$\Lambda_\mathcal{M} = \operatorname{diag}(\lambda_1, \lambda_2\lambda_3, \lambda_4), \tag{4.11b}$$

$$X = \mathfrak{N} \begin{bmatrix} \lambda_1 & 0 & 0 & \lambda_4 \\ 0 & n_x & 0 & 0 \\ n_x & 0 & 0 & n_x \\ 0 & 0 & n_x & 0 \end{bmatrix}, \quad \mathfrak{N} = \operatorname{diag}\left(\sqrt{\lambda_1^2 + 1}, 1, 1, \sqrt{\lambda_4^2 + 1}\right)^{-1},$$

where λ_i, $\mathbf{x}_i$ are given in (4.10). Here, $\mathfrak{N}$ is the normalizing matrix. Moreover, with a slight abuse of notation, we rearrange $\mathcal{M}$ in (4.8) as $\mathcal{M} = X\Lambda X^\mathsf{T}$ where $\Lambda = \mathfrak{N}\Lambda_\mathcal{M}\mathfrak{N}$ is the scaled eigenvalue matrix. For the north and south boundaries

$$\Lambda = \operatorname{diag}\left(\frac{\lambda_1}{\lambda_1^2 + 1}, \frac{\lambda_2}{2}, \frac{\lambda_3}{2}, \frac{\lambda_4}{\lambda_4^2 + 1}\right), \tag{4.12a}$$

while for the east and west boundaries

$$\Lambda = \operatorname{diag}\left(\frac{\lambda_1}{\lambda_1^2 + 1}, \lambda_2, \lambda_3, \frac{\lambda_4}{\lambda_4^2 + 1}\right). \tag{4.12b}$$

Remark 4.4. *The diagonal entries of the scaled eigenvalue matrices* (4.12) *are bounded for all* $u_\mathbf{n}$.

Next, we partition (4.12) into the positive and negative components and denote them respectively with superscripts/subscripts $\pm$

$$\mathcal{M} = \begin{bmatrix} X_+ \\ X_- \end{bmatrix}^{\mathsf{T}} \begin{bmatrix} \Lambda^+ & 0 \\ 0 & \Lambda^- \end{bmatrix} \begin{bmatrix} X_+ \\ X_- \end{bmatrix}, \tag{4.13}$$

and therefore, by substituting (4.13) into (4.7), BT becomes

$$\mathrm{BT} = -\oint_\Gamma \begin{bmatrix} W_+ \\ W_- \end{bmatrix}^{\mathsf{T}} \begin{bmatrix} \Lambda^+ & 0 \\ 0 & \Lambda^- \end{bmatrix} \begin{bmatrix} W_+ \\ W_- \end{bmatrix} ds. \tag{4.14}$$

In (4.14), we introduced the new variables $W_+ = X_+^{\mathsf{T}}\mathbf{q}$, $W_- = X_-^{\mathsf{T}}\mathbf{q}$. Moreover, they are called in- and out-going characteristic variables, respectively. For the north and south boundaries, they are

$$W_+ = \begin{bmatrix} v + pn_y \\ \lambda_4 u - \nu u_y n_y \end{bmatrix}, \quad W_- = \begin{bmatrix} \lambda_1 u - \nu u_y n_y \\ v - pn_y \end{bmatrix},$$
$$\Lambda_+ = \begin{bmatrix} \dfrac{\lambda_3}{2} & 0 \\ 0 & \dfrac{\lambda_4}{\lambda_4^2+1} \end{bmatrix}, \quad \Lambda_- = \begin{bmatrix} \dfrac{\lambda_1}{\lambda_1^2+1} & 0 \\ 0 & \dfrac{\lambda_2}{2} \end{bmatrix},$$

while for the east and west boundaries, they are

$$W_+ = \left[\lambda_4 u + pn_x\right], \quad W_- = \left[\lambda_1 u + pn_x\right], \quad \Lambda_+ = \left[\frac{\lambda_4}{\lambda_4^2+1}\right], \quad \Lambda_- = \left[\frac{\lambda_1}{\lambda_1^2+1}\right].$$

The terms associated with negative eigenvalues Λ^- add growth to the energy rate (4.6) due to the negative sign preceding them. We therefore limit this growth as in the following Proposition, and the proof is in [46].

Proposition 3. *The number of boundary conditions required to bound* (4.6) *coincide with the number of negative eigenvalues of* $\mathcal{M}$.

In (4.10), $\lambda_1 < 0$ and $\lambda_4 > 0$ regardless of the sign of $u_{\mathbf{n}}$. Therefore, there are two negative eigenvalues λ_1, λ_2 and two positive eigenvalues λ_3, λ_4 in (4.10a) at the north and south boundaries. According to Proposition 3, precisely two boundary conditions must be prescribed at both boundaries (this is due to the presence of νu_{yy} in the equations (4.4)). At the east and west boundaries, there is only one negative eigenvalue λ_1 in (4.10b) inferring that only one boundary condition must be imposed at each boundary.

We have now established the minimal number of boundary conditions required for boundedness and the boundaries where they should be imposed, however, the question about their form remains. In (4.14), the problematic growth terms are the ingoing characteristic variables since they are positive. We circumvent this by specifying the general boundary conditions [39, 79, 80]

$$\mathcal{S}(W_- - \mathcal{R}W_+) = \mathbf{g}, \tag{4.15}$$

where $\mathcal{R}$ is a nonzero matrix with the number of columns coinciding with the number of diagonal elements of Λ^+ and the number of rows coinciding with the number of negative eigenvalues of $\mathcal{M}$. Here, $\mathcal{S}$ is an invertible matrix that combines the variables in W_- while $\mathcal{SR}$ combines the variables in W_+ to implement the desired boundary conditions.

Remark 4.5. *In the subsequent analysis, unless stated otherwise, we will set $\mathcal{S}$ in (4.15) to be an identity matrix.*

Proposition 4. *Strong imposition of the homogeneous form of the boundary conditions (4.15) yields an energy estimate if $\Lambda^+ + \mathcal{R}^\mathsf{T}\Lambda^-\mathcal{R} \geq 0$ [18, 32].*

Proof. By substituting (4.15) into (4.14), BT transforms to

$$\mathrm{BT} = -\oint_\Gamma \begin{bmatrix} W_+ \\ \mathbf{g} \end{bmatrix}^\mathsf{T} \begin{bmatrix} \Lambda^+ + \mathcal{R}^\mathsf{T}\Lambda^-\mathcal{R} & \Lambda^-\mathcal{R} \\ \mathcal{R}^\mathsf{T}\Lambda^- & \Lambda^- \end{bmatrix} \begin{bmatrix} W_+ \\ \mathbf{g} \end{bmatrix} ds, \tag{4.16}$$

which by setting $\mathbf{g} = 0$, it further simplifies to

$$\mathrm{BT} = -\oint_\Gamma W_+^\mathsf{T}(\Lambda^+ + \mathcal{R}^\mathsf{T}\Lambda^-\mathcal{R})W_+ ds. \tag{4.17}$$

Hence, BT is non-positive if

$$\Lambda^+ + \mathcal{R}^\mathsf{T}\Lambda^-\mathcal{R} \geq 0, \tag{4.18}$$

and Lemma 1 completes the proof. □

To tackle the non-homogeneous boundary conditions case, we first modify Lemma 1 to account for non-zero external data.

Lemma 5. *The semi-norms $||U||_{\bar{I}}^2$ and $||U_y||_{\bar{I}}^2$ are bounded if BT (4.6) is bounded by external data.*

Proof. Suppose that BT is bounded by data, then the temporal integration of (4.6) over a finite time domain leads to a bounded growth

$$||\mathrm{U}||_{\bar{I}}^2\Big|_{t=T} + 2\nu \int_0^T ||\mathrm{U}_y||_{\bar{I}}^2 dt \leq ||\mathbf{f}||_{\bar{I}}^2 + \int_0^T \oint_\Gamma \mathbf{g}^\mathsf{T}\Phi\mathbf{g} ds dt, \tag{4.19}$$

where Φ is a finite matrix. □

Proposition 6. *Strong imposition of the non-homogeneous form of the boundary conditions (4.15) yield an estimate if there exists a non-negative matrix Ξ and $\mathcal{R}$ such that*

$$(\Lambda^-\mathcal{R})(\Lambda^+ + \mathcal{R}^\mathsf{T}\Lambda^-\mathcal{R})^{-1}(\mathcal{R}^\mathsf{T}\Lambda^-) - \Lambda^- \leq \Xi < \infty \quad \textit{and} \quad \Lambda^+ + \mathcal{R}^\mathsf{T}\Lambda^-\mathcal{R} > 0, \tag{4.20}$$

[18, 32].

Proof. Let's assume that $\Xi < \infty$, and $\mathcal{R}$ satisfies the stringent form of (4.18) such that $\Lambda^+ + \mathcal{R}^\mathsf{T}\Lambda^-\mathcal{R} > 0$. Implementing boundary conditions (4.15) strongly yields (4.16). Therefore, we consider the boundary matrix in (4.16) and multiply it on the right with a triangular matrix and on the left with the corresponding transpose

$$\Upsilon = \begin{bmatrix} I & 0 \\ \Pi^\mathsf{T} & I \end{bmatrix} \begin{bmatrix} \Lambda^+ + \mathcal{R}^\mathsf{T}\Lambda^-\mathcal{R} & \Lambda^-\mathcal{R} \\ \mathcal{R}^\mathsf{T}\Lambda^- & \Lambda^- \end{bmatrix} \begin{bmatrix} I & \Pi \\ 0 & I \end{bmatrix},$$

where I is a unit matrix of an appropriate size. The choice $\Pi = -(\Lambda^+ + \mathcal{R}^\mathsf{T}\Lambda^-\mathcal{R})^{-1}(\mathcal{R}^\mathsf{T}\Lambda^-)$ transforms Υ into the diagonal matrix

$$\Upsilon = \begin{bmatrix} \Lambda^+ + \mathcal{R}^\mathsf{T}\Lambda^-\mathcal{R} & 0 \\ 0 & \Lambda^- - (\Lambda^-\mathcal{R})(\Lambda^+ + \mathcal{R}^\mathsf{T}\Lambda^-\mathcal{R})^{-1}(\mathcal{R}^\mathsf{T}\Lambda^-) \end{bmatrix}. \tag{4.21}$$

Finally, we add and subtract Ξ to the *Schur complement* of Υ i.e. matrix entry Υ_{22}. Therefore, substituting the above into (4.16) simplifies BT to

$$\begin{aligned} \mathrm{BT} = &- \oint_\Gamma \begin{bmatrix} W_+ + \Pi\mathbf{g} \\ \mathbf{g} \end{bmatrix}^\mathsf{T} \widehat{\Upsilon} \begin{bmatrix} W_+ + \Pi\mathbf{g} \\ \mathbf{g} \end{bmatrix} ds \\ &+ \oint_\Gamma \mathbf{g}^\mathsf{T}\Xi\mathbf{g} ds, \end{aligned} \tag{4.22}$$

where $\widehat{\Upsilon}$ is the modified Υ in (4.21)

$$\widehat{\Upsilon} = \begin{bmatrix} \Lambda^+ + \mathcal{R}^\mathsf{T}\Lambda^-\mathcal{R} & 0 \\ 0 & \Lambda^- - (\Lambda^-\mathcal{R})(\Lambda^+ + \mathcal{R}^\mathsf{T}\Lambda^-\mathcal{R})^{-1}(\mathcal{R}^\mathsf{T}\Lambda^-) + \Xi \end{bmatrix}.$$

In (4.22), the first boundary integral is negative if $\mathcal{R}$ satisfies $\Lambda^+ + \mathcal{R}^\mathsf{T}\Lambda^-\mathcal{R} > 0$ and $\Xi < \infty$ exists such that $\Xi \geq (\Lambda^-\mathcal{R})(\Lambda^+ + \mathcal{R}^\mathsf{T}\Lambda^-\mathcal{R})^{-1}(\mathcal{R}^\mathsf{T}\Lambda^-) - \Lambda^-$. Therefore, BT is bounded by data and the energy rate (4.6) becomes

$$\frac{d}{dt}||\mathrm{U}||_I^2 + 2\nu||\mathrm{U}_y||_I^2 \leq \oint_\Gamma \mathbf{g}^\mathsf{T}\Xi\mathbf{g} ds, \tag{4.23}$$

which leads to an estimate by application of Lemma 5. □

Remark 4.6. *In (4.22), $\Xi = \Xi(\Lambda^\pm)$ and $\Lambda^\pm$ depend on the solution due to the nonlinear nature of our problem. However, the elements of $\Lambda^\pm$ are bounded (see Remark 4.4).*

Remark 4.7. *Boundary conditions (4.1b) can be related to the general form (4.15) i.e. $HU = W_- - \mathcal{R}W_+ = \boldsymbol{g}$, by computing an appropriate $\mathcal{R}$ satisfying (4.18).*

4.1.2 Stability conditions for weakly implemented boundary conditions

To prepare for the upcoming discrete analysis, we implement boundary conditions (4.15) weakly and derive the energy estimates. We follow the analysis from the previous section. Equation (4.4) augmented with weak boundary conditions (4.15) becomes

$$\bar{I}\mathrm{U}_t + \mathcal{D}(\mathrm{U})\mathrm{U} = \mathbb{SAT}, \tag{4.24}$$

where $\mathbb{SAT} = \mathcal{L}\left(\Sigma(H\mathrm{U} - \mathbf{g})\right)$ is the bounary penalty term. Here, where $\mathcal{L}(\cdot)$ is the lifting operator defined in (2.13) and Σ is the penalty coefficient matrix. Our ambition is to determine Σ such that we obtain an energy estimate similar to (4.19). The energy method applied to (4.24) leads to

$$\frac{d}{dt}||\mathrm{U}||_I^2 + 2\nu||\mathrm{U}_y||_I^2 = \widetilde{\mathrm{BT}} = \mathrm{BT} + \mathrm{PT}, \tag{4.25}$$

where BT denotes the indefinite boundary terms that are similar to BT in (4.6). Meanwhile, PT denotes the penalty boundary terms

$$\mathrm{PT} = \int_{\Omega} \left[\mathrm{U}^{\mathsf{T}} \mathbb{S}\mathbb{A}\mathbb{T} + (\mathrm{U}^{\mathsf{T}} \mathbb{S}\mathbb{A}\mathbb{T})^{\mathsf{T}} \right] ds,$$

which by the definition of $\mathcal{L}$ simplifies to

$$\mathrm{PT} = \oint_{\Gamma} \left[\mathrm{U}^{\mathsf{T}} \Sigma (H\mathrm{U} - \mathbf{g}) + (\mathrm{U}^{\mathsf{T}} \Sigma (H\mathrm{U} - \mathbf{g}))^{\mathsf{T}} \right] ds.$$

The energy rate (4.25) is decreasing if $\widetilde{\mathrm{BT}}$ is non positive or bounded by data. By first writing BT in the form (4.14) and also replacing the boundary conditions in PT with (4.15), $\widetilde{\mathrm{BT}}$ can be written as

$$\begin{aligned} \widetilde{\mathrm{BT}} = &- \oint_{\Gamma} \begin{bmatrix} W_+ \\ W_- \end{bmatrix}^{\mathsf{T}} \begin{bmatrix} \Lambda^+ & 0 \\ 0 & \Lambda^- \end{bmatrix} \begin{bmatrix} W_+ \\ W_- \end{bmatrix} ds \\ &+ \oint_{\Gamma} \left[\mathrm{U}^{\mathsf{T}} \Sigma (W_- - \mathcal{R} W_+ - \mathbf{g}) + (\mathrm{U}^{\mathsf{T}} \Sigma (W_- - \mathcal{R} W_+ - \mathbf{g}))^{\mathsf{T}} \right]. \end{aligned} \tag{4.26}$$

Since Σ in (4.24) is general, we modify it as $\Sigma = T^{\mathsf{T}} X_- \widetilde{\Sigma}$, where X_- is the negative component of the eigenvector matrices (4.11) and $\widetilde{\Sigma}$ is a new penalty coefficient. We also introduced matrix T which transforms the solution U to variable $\mathbf{q} = T\mathrm{U}$ in (4.7) and is given by

$$T = \begin{bmatrix} 1 & 0 & 0 \\ 0 & 1 & 0 \\ 0 & 0 & 1 \\ \nu \partial_y & 0 & 0 \end{bmatrix}, \tag{4.27}$$

such that

$$\mathrm{U}^{\mathsf{T}} \Sigma = (T\mathrm{U})^{\mathsf{T}} X_- \widetilde{\Sigma} = (X_-^{\mathsf{T}} \mathbf{q})^{\mathsf{T}} \widetilde{\Sigma} = W_-^{\mathsf{T}} \widetilde{\Sigma}. \tag{4.28}$$

By substituting (4.28) into (4.26), we combine the two line integrals as

$$\widetilde{\mathrm{BT}} = - \oint_{\Gamma} \begin{bmatrix} W_+ \\ W_- \\ \mathbf{g} \end{bmatrix}^{\mathsf{T}} \begin{bmatrix} \Lambda^+ & (\widetilde{\Sigma}\mathcal{R})^{\mathsf{T}} & 0 \\ \widetilde{\Sigma}\mathcal{R} & \Lambda^- - (\widetilde{\Sigma} + \widetilde{\Sigma}^{\mathsf{T}}) & \widetilde{\Sigma} \\ 0 & \widetilde{\Sigma}^{\mathsf{T}} & 0 \end{bmatrix} \begin{bmatrix} W_+ \\ W_- \\ \mathbf{g} \end{bmatrix} ds. \tag{4.29}$$

Proposition 7. *$\widetilde{BT}$ in (4.29) with $\widetilde{\Sigma} = \Lambda^-$ [18] and zero boundary data is non-positive if $\mathcal{R}$ exists such that (4.18) holds.*

Proof. Substituting $\widetilde{\Sigma} = \Lambda^-$ into (4.29) with $\mathbf{g} = 0$ yields

$$\widetilde{\mathrm{BT}} = - \oint_{\Gamma} \begin{bmatrix} W_+ \\ W_- \end{bmatrix}^{\mathsf{T}} \begin{bmatrix} \Lambda^+ & \mathcal{R}^{\mathsf{T}} \Lambda^- \\ \Lambda^- \mathcal{R} & -\Lambda^- \end{bmatrix} \begin{bmatrix} W_+ \\ W_- \end{bmatrix} ds.$$

By adding and subtracting $\oint_\Gamma (\mathcal{R}W_+)^\mathsf{T}\Lambda^-(\mathcal{R}W_+)ds$ above, $\widetilde{\mathrm{BT}}$ becomes

$$\begin{aligned}\widetilde{\mathrm{BT}} &= -\oint_\Gamma W_+^\mathsf{T}(\Lambda^+ + \mathcal{R}^\mathsf{T}\Lambda^-\mathcal{R})W_+ds + \oint_\Gamma \begin{bmatrix} W_+ \\ W_- \end{bmatrix}^\mathsf{T} \begin{bmatrix} \mathcal{R}^\mathsf{T}\Lambda^-\mathcal{R} & -\mathcal{R}^\mathsf{T}\Lambda^- \\ -\Lambda^-\mathcal{R} & -\Lambda^- \end{bmatrix} ds \\ &= -\oint_\Gamma W_+^\mathsf{T}(\Lambda^+ + \mathcal{R}^\mathsf{T}\Lambda^-\mathcal{R})W_+ds + \oint_\Gamma (W_- - \mathcal{R}W_+)^\mathsf{T}\Lambda^-(W_- - \mathcal{R}W_+)ds.\end{aligned} \tag{4.30}$$

The first term in (4.30) is negative if (4.18) holds and the second term is negative since Λ^- is negative. □

The energy estimate follows trivially using Lemma (1). Further, the penalty coefficient matrix in (4.28) becomes $\Sigma = T^\mathsf{T}X_-\Lambda^-$.

Remark 4.8. *$\widetilde{BT}$ in (4.30) is similar to BT in (4.17) with an additional dissipative term $\oint_\Gamma (W_- - \mathcal{R}W_+)^\mathsf{T}\Lambda^-(W_- - \mathcal{R}W_+)ds$ which is proportional to the boundary conditions (4.15).*

Next, we show that the choice of Σ in (4.28) also yields an energy estimate for the non-homogeneous case.

Proposition 8. *$\widetilde{BT}$ in (4.29) with non-homogeneous boundary condition and $\widetilde{\Sigma} = \Lambda^-$ is bounded by data if $\mathcal{R}$ and a positive definite matrix Ξ exists satisfying (4.20) [18, 32].*

Proof. By substituting $\widetilde{\Sigma} = \Lambda^-$ in (4.29), then adding and subtracting $\oint_\Gamma \mathbf{g}^\mathsf{T}\Xi\mathbf{g}ds$, $\widetilde{\mathrm{BT}}$ becomes

$$\widetilde{\mathrm{BT}} = -\oint_\Gamma \begin{bmatrix} W_+ \\ W_- \\ \mathbf{g} \end{bmatrix}^\mathsf{T} \begin{bmatrix} \Lambda^+ & \mathcal{R}^\mathsf{T}\Lambda^- & 0 \\ \Lambda^-\mathcal{R} & -\Lambda^- & \Lambda^- \\ 0 & \Lambda^- & \Xi \end{bmatrix} \begin{bmatrix} W_+ \\ W_- \\ \mathbf{g} \end{bmatrix} ds + \oint_\Gamma \mathbf{g}^\mathsf{T}\Xi\mathbf{g}ds. \tag{4.31}$$

The matrix split [18]

$$\begin{aligned}\begin{bmatrix} \Lambda^+ & \mathcal{R}^\mathsf{T}\Lambda^- & 0 \\ \Lambda^-\mathcal{R} & -\Lambda^- & \Lambda^- \\ 0 & \Lambda^- & \Xi \end{bmatrix} &= \begin{bmatrix} \Lambda^+ + \mathcal{R}^\mathsf{T}\Lambda^-\mathcal{R} & 0 & \mathcal{R}^\mathsf{T}\Lambda^- \\ 0 & 0 & 0 \\ \Lambda^-\mathcal{R} & 0 & \Lambda^- + \Xi \end{bmatrix} \\ &\quad + \begin{bmatrix} -\mathcal{R}^\mathsf{T}\Lambda^-\mathcal{R} & \mathcal{R}^\mathsf{T}\Lambda^- & -\mathcal{R}^\mathsf{T}\Lambda^- \\ \Lambda^-\mathcal{R} & -\Lambda^- & \Lambda^- \\ -\Lambda^-\mathcal{R} & \Lambda^- & -\Lambda^- \end{bmatrix},\end{aligned} \tag{4.32}$$

transforms $\widetilde{\mathrm{BT}}$ to

$$\begin{aligned}\widetilde{\mathrm{BT}} = &-\oint_\Gamma \begin{bmatrix} W_+ \\ \mathbf{g} \end{bmatrix}^\mathsf{T} \begin{bmatrix} \Lambda^+ + \mathcal{R}^\mathsf{T}\Lambda^-\mathcal{R} & \mathcal{R}^\mathsf{T}\Lambda^- \\ \Lambda^-\mathcal{R} & \Lambda^- + \Xi \end{bmatrix} \begin{bmatrix} W_+ \\ \mathbf{g} \end{bmatrix} ds \\ &+ \oint_\Gamma (W_- - \mathcal{R}W_+ - \mathbf{g})^\mathsf{T}\Lambda^-(W_- - \mathcal{R}W_+ - \mathbf{g})ds + \oint_\Gamma \mathbf{g}^\mathsf{T}\Xi\mathbf{g}ds.\end{aligned} \tag{4.33}$$

The first line integral in (4.33) is identical to (4.16) and it is non-positive using Proposition 4 if Ξ satisfies (4.20). We also note that the second integral in (4.33) is negative while the last term is data and it is bounded since $\Xi < \infty$. Therefore, $\widetilde{\mathrm{BT}}$ becomes

$$\widetilde{\mathrm{BT}} \leq \oint_\Gamma \mathbf{g}^\mathsf{T}\Xi\mathbf{g}ds, \tag{4.34}$$

which is identical to the external data term in (4.22). □

Lastly, temporal integration of (4.25) with (4.34) lead to the results (4.19), and hence proving that the semi-norms are bounded by data.

Remark 4.9. *Proposition 8 is the extension of Proposition 7 for the non-homogenenous boundary conditions case. By setting* $\boldsymbol{g} = 0$ *in* (4.33)*, we obtain* (4.30) *and this further alleviates the stringent requirement of* (4.18) *in* (4.20) *since* Ξ *will not be required.*

4.2 Energy stable boundary conditions

4.2.1 Strongly imposed boundary conditions

Next, we derive a new set of boundary conditions specific to the flat plate boundary layer problem. These boundary conditions must have the general form (4.15) and subsequently satisfy condition (4.18). To achieve this, we return to the energy rate (4.6) and use the indefinite BT terms as a guide to identify the terms that add growth terms to the energy rate. We will then impose conditions to prevent energy growth while satisfying the physics of the problem as illustrated in Figure 3.1.

Starting at the south boundary which is aligned with the solid surface, we eliminate the contribution of the south boundary in BT by prescribing a no-slip velocity condition i.e. $u = v = 0$. The north boundary is considered next, at which we should impose two boundary conditions which are given below. It is important to note that at this boundary, $u_{\mathbf{n}} > 0$. Next, we turn to the vertical boundaries where only one boundary condition is required. Since we assumed inflow ($u_{\mathbf{n}} < 0$) at the west boundary and outflow ($u_{\mathbf{n}} > 0$) at the east boundary, we prescribe velocity at the west boundary and pressure at the east boundary. In summary, the proposed boundary conditions are

$$\begin{aligned} &\frac{\vartheta}{2}vu - \nu u_y = g, \quad p = P_\infty, && \text{north boundary,}, \\ &u = 0, \quad v = 0, && \text{south boundary,} \\ &p = P_\infty, && \text{east boundary,} \\ &u = U_\infty, && \text{west boundary,} \end{aligned} \tag{4.35}$$

where $\vartheta \in [0, 1]$ is a constant that gives us the flexibility to impose either the Robin boundary condition ($\vartheta = 1$) or the Neumann boundary condition ($\vartheta = 0$), depending on the available data. The above can be written in the form (4.1b) as

$$H_e\mathrm{U} = \begin{bmatrix} 0 & 0 & 1 \end{bmatrix} \begin{bmatrix} u \\ v \\ p \end{bmatrix} = \begin{bmatrix} P_\infty \end{bmatrix}, \qquad H_n\mathrm{U} = \begin{bmatrix} \frac{\vartheta}{2}v - \nu\partial_y & 0 & 0 \\ 0 & 0 & 1 \end{bmatrix} \begin{bmatrix} u \\ v \\ p \end{bmatrix} = \begin{bmatrix} g \\ P_\infty \end{bmatrix}, \tag{4.36}$$

$$H_w\mathrm{U} = \begin{bmatrix} 1 & 0 & 0 \end{bmatrix} \begin{bmatrix} u \\ v \\ p \end{bmatrix} = \begin{bmatrix} U_\infty \end{bmatrix}, \qquad H_s\mathrm{U} = \begin{bmatrix} 1 & 0 & 0 \\ 0 & 1 & 0 \end{bmatrix} \begin{bmatrix} u \\ v \\ p \end{bmatrix} = \begin{bmatrix} 0 \\ 0 \end{bmatrix},$$

where P_∞ is the freestream pressure.

By strongly imposing the homogeneous form of the boundary conditions (4.36) in (4.6), most of the boundary terms vanish and only the contribution from the north and east boundaries

remain which carry appropriate signs since $u_{\boldsymbol{n}} > 0$ at the outflow boundaries. The energy rate (4.6) becomes

$$\frac{d}{dt}||\mathrm{U}||_{\bar{I}}^2 + 2\nu||\mathrm{U}_y||_{\bar{I}}^2 = -\int_{\Gamma_n}(1-\vartheta)u_{\mathbf{n}}u^2dx - \int_{\Gamma_e}u_{\mathbf{n}}u^2ds \leq 0. \tag{4.37}$$

Notice that $\vartheta = 0$, which prescribes the Neumann boundary condition in (4.35), leads to a more dissipative energy rate. Also note that the last term in (4.37) is dissipative since $u_{\mathbf{n}} > 0$. Finally, temporal integration over a finite time domain $[0, T]$ and imposing the initial condition leads to the energy estimate

$$||\mathrm{U}||_{\bar{I}}^2 + 2\nu\int_0^T||\mathrm{U}_y||_{\bar{I}}^2dt \leq ||\mathbf{f}||_{\bar{I}}^2. \tag{4.38}$$

The estimate (4.38) shows that boundary conditions (4.36) are energy stable. Further, we show that they can be written in the general form (4.15) by computing $\mathcal{R}$ satisfying (4.18) for each boundary. We set $\mathcal{S}$ for all the boundaries to be an identity matrix. Therefore, starting with the north and south boundaries, we propose $\mathcal{R}$ in (4.15) with the form

$$\mathcal{R} = \begin{bmatrix} 0 & r_1 \\ r_2 & 0 \end{bmatrix}, \tag{4.39}$$

which together with the variables W_+, W_- in (4.14), lead to

$$\begin{aligned} W_- - \mathcal{R}W_+ &= \begin{bmatrix} \lambda_1 u - \nu u_y n_y \\ v - pn_y \end{bmatrix} - \begin{bmatrix} 0 & r_1 \\ r_2 & 0 \end{bmatrix}\begin{bmatrix} v + pn_y \\ \lambda_4 u - \nu u_y n_y \end{bmatrix} \\ &= \begin{bmatrix} (\lambda_1 - r_1\lambda_4)u + (r_1 - 1)\nu u_y n_y \\ (1 - r_2)v - (1 + r_2)pn_y \end{bmatrix} = \begin{bmatrix} g_1 \\ g_2 \end{bmatrix}. \end{aligned} \tag{4.40}$$

Here, g_1, g_2 are boundary data. To write the no-slip condition at the south boundary in the form (4.15), we set $r_1 = 1$ and $r_2 = -1$ in (4.39) which simplify (4.40) to

$$W_- - \mathcal{R}W_+ = \begin{bmatrix} \lambda_1 - \lambda_4 & 0 \\ 0 & 2 \end{bmatrix}\begin{bmatrix} u \\ v \end{bmatrix} = \begin{bmatrix} 0 \\ 0 \end{bmatrix}. \tag{4.41}$$

By further multiplying (4.41) on both sides with the diagonal matrix $\mathrm{diag}(\lambda_1 - \lambda_4, 2)^{-1}$, we obtain $u = v = 0$. This choice of $\mathcal{R}$ satisfies (4.18) since

$$\begin{aligned} \Lambda_+ + \mathcal{R}^{\mathsf{T}}\Lambda_-\mathcal{R} &= \begin{bmatrix} \frac{\lambda_3}{2} & 0 \\ 0 & \frac{\lambda_4}{\lambda_4^2 + 1} \end{bmatrix} + \begin{bmatrix} 0 & 1 \\ -1 & 0 \end{bmatrix}^T \begin{bmatrix} \frac{\lambda_1}{\lambda_1^2 + 1} & 0 \\ 0 & \frac{\lambda_2}{2} \end{bmatrix}\begin{bmatrix} 0 & 1 \\ -1 & 0 \end{bmatrix} \\ &= \begin{bmatrix} 0 & 0 \\ 0 & 0 \end{bmatrix}. \end{aligned} \tag{4.42}$$

where Λ_+, Λ_- for horizontal boundaries are given in (4.14).

To show that the Robin velocity ($\vartheta = 1$) and the Dirichlet pressure conditions at the north boundary with $(n_x, n_y) = (0, 1)$ in (4.36) can be written in the form (4.15), we set $r_1 = 0$ and $r_2 = 1$ in (4.40) which leads to

$$W_- - \mathcal{R}W_+ = \begin{bmatrix} \lambda_1 u - \nu u_y n_y \\ -2pn_y \end{bmatrix} = \begin{bmatrix} 1 & 0 \\ 0 & -2 \end{bmatrix}\begin{bmatrix} \lambda_1 u - \nu u_y \\ p \end{bmatrix} = \begin{bmatrix} g_1 \\ g_2 \end{bmatrix}.$$

Moreover, (4.18) is satisfied by this choice since

$$\begin{aligned}\Lambda_+ + \mathcal{R}^\mathsf{T}\Lambda_-\mathcal{R} &= \begin{bmatrix}\frac{\lambda_3}{2} & 0\\ 0 & \frac{\lambda_4}{\lambda_4^2+1}\end{bmatrix} + \begin{bmatrix}0 & 0\\ 1 & 0\end{bmatrix}^\mathsf{T}\begin{bmatrix}\frac{\lambda_1}{\lambda_1^2+1} & 0\\ 0 & \frac{\lambda_2}{2}\end{bmatrix}\begin{bmatrix}0 & 0\\ 1 & 0\end{bmatrix} \\ &= \begin{bmatrix}0 & 0\\ 0 & \frac{\lambda_4}{\lambda_4^2+1}\end{bmatrix} \geq 0.\end{aligned} \tag{4.43}$$

Next, we turn to the east and west boundaries. Similar to the horizontal boundaries, we want to show that the west and east boundary conditions can be written in the form (4.15). We begin by substituting W_+, W_- in (4.14) into (4.15) to obtain

$$W_- - \mathcal{R}W_+ = \Big[\lambda_1 u + pn_x\Big] - \mathcal{R}\Big[\lambda_4 u + pn_x\Big] = (\lambda_1 - \mathcal{R}\lambda_4)u + (1-\mathcal{R})pn_x = \mathbf{g}, \tag{4.44}$$

where $\mathbf{g}$ denotes data as before. Starting with the west boundary, we want to determine $\mathcal{R}$ such that it removes the pressure term from (4.44) and only the velocity remains. The obvious choice $\mathcal{R} = 1$ leads to

$$W_- - \mathcal{R}W_+ = (\lambda_1 - \lambda_4)u = \mathbf{g}.$$

Consequently, this choice satisfies (4.18) since

$$\Lambda_+ + \mathcal{R}^\mathsf{T}\Lambda_-\mathcal{R} = \frac{\lambda_4}{\lambda_4^2+1} + \frac{\lambda_1}{\lambda_1^2+1} = 0, \tag{4.45}$$

where Λ_+, Λ_- are given in (4.14).

Similarly, to write the pressure condition at the east boundary in the form (4.15), we need an appropriate $\mathcal{R}$ satisfying (4.18) that remove the velocity contribution in (4.44). Setting $\mathcal{R} = \lambda_1/\lambda_4$ yields

$$W_- - \mathcal{R}W_+ = \left(1 - \frac{\lambda_1}{\lambda_4}\right)p = \mathbf{g},$$

and satisfies (4.18) since

$$\Lambda^+ + \mathcal{R}^\mathsf{T}\Lambda^-\mathcal{R} = \frac{\lambda_4}{\lambda_4^2+1} + \left(\frac{\lambda_1}{\lambda_4}\right)^2\frac{\lambda_1}{\lambda_1^2+1} = \frac{u_\mathbf{n}(u_\mathbf{n}^2+1)}{(\lambda_4^2+1)(\lambda_1^2+1)\lambda_4} \geq 0, \tag{4.46}$$

4.2.2 Weakly imposed boundary conditions

Similar to Section 4.1.2, we implement the boundary conditions (4.35) weakly and show that they lead to an energy estimate. Let's recall the weak formulation (4.24)

$$\bar{I}\mathrm{U}_t + \mathcal{D}(\mathrm{U})\mathrm{U} = \mathcal{L}\left(\Sigma(H\mathrm{U} - \mathbf{g})\right), \qquad (x,y) \in \Omega, \quad t > 0, \tag{4.47}$$

where $H\mathrm{U}$ is now given by (4.36). As before, we want to determine the penalty matrix Σ such that the weakly imposed boundary conditions (4.36) yield an energy estimate. Applying the energy method to (4.47) leads to the energy rate

$$\frac{d}{dt}||\mathrm{U}||_{\bar{I}}^2 + 2\nu||\mathrm{U}_y||_{\bar{I}}^2 = \mathrm{BT} + \mathrm{PT}, \tag{4.48}$$

where BT, PT are given in (4.6) and (4.25), respectively. We further express them as a sum of all four boundary contributions $\mathrm{BT} = \mathrm{BT}_n + \mathrm{BT}_e + \mathrm{BT}_s + \mathrm{BT}_w$, where

$$\mathrm{BT}_n = -\int_{\Gamma_n} (u_{\mathbf{n}} u^2 + 2u_{\mathbf{n}} p - 2\nu u u_y n_y) dx, \quad \mathrm{BT}_e = -\int_{\Gamma_e} (u_{\mathbf{n}} u^2 + 2u_{\mathbf{n}} p) dy, \tag{4.49}$$
$$\mathrm{BT}_s = -\int_{\Gamma_s} (u_{\mathbf{n}} u^2 + 2u_{\mathbf{n}} p - 2\nu u u_y n_y) dx, \quad \mathrm{BT}_w = -\int_{\Gamma_w} (u_{\mathbf{n}} u^2 + 2u_{\mathbf{n}} p) dy.$$

Similarly, we partition the penalty terms as

$$\mathrm{PT} = \sum_{i \in \{n,e,s,w\}} \int_{\Gamma_i} \left(\mathrm{U}^{\mathsf{T}} \Sigma_i H_i \mathrm{U} + (\mathrm{U}^{\mathsf{T}} \Sigma_i H_i \mathrm{U})^{\mathsf{T}} \right) ds. \tag{4.50}$$

Our ambition is to determine Σ such that the boundary terms in (4.48) are dissipative. We propose the following penalty coefficients for each boundary

$$\Sigma_s = \begin{bmatrix} \frac{u_{\mathbf{n}}}{2} - \nu \partial_y^* n_y & 0 \\ 0 & 0 \\ 0 & n_y \end{bmatrix}, \quad \Sigma_n = \begin{bmatrix} n_y & 0 \\ 0 & n_y \\ 0 & 0 \end{bmatrix}, \tag{4.51}$$
$$\Sigma_w = \begin{bmatrix} \frac{u_{\mathbf{n}}}{2} \\ 0 \\ n_x \end{bmatrix}, \qquad \Sigma_e = \begin{bmatrix} n_x \\ 0 \\ 0 \end{bmatrix},$$

where ∂_y^* is the $y-$partial derivative operator acting on the left such that $\mathrm{U}^{\mathsf{T}} \partial_y^* = \mathrm{U}_y^{\mathsf{T}}$. By substituting (4.51) into (4.50), the penalty terms becomes

$$\mathrm{PT}_n = \int_{\Gamma_n} (\vartheta u_{\mathbf{n}} u^2 + 2u_{\mathbf{n}} p - 2\nu u u_y n_y) dx, \quad \mathrm{PT}_e = \int_{\Gamma_e} 2u_{\mathbf{n}} p dy, \tag{4.52}$$
$$\mathrm{PT}_s = \int_{\Gamma_s} (u_{\mathbf{n}} u^2 + 2u_{\mathbf{n}} p - 2\nu u u_y n_y) dx, \quad \mathrm{PT}_w = \int_{\Gamma_w} (u_{\mathbf{n}} u^2 + 2u_{\mathbf{n}} p) dy.$$

Lastly, combining (4.49) and (4.52) leads to the cancellation of several terms and the energy rate (4.48) becomes

$$\frac{d}{dt} ||\mathrm{U}||_I^2 + 2\nu ||\mathrm{U}_y||_I^2 = -\int_{\Gamma_n} (1 - \vartheta) u_{\mathbf{n}} u^2 dx - \int_{\Gamma_e} u_{\mathbf{n}} u^2 dy \leq 0, \tag{4.53}$$

which is similar to (4.37). Note also that the dissipative boundary terms in (4.53) came from the two outflow boundaries.

In essence, the strong imposition of boundary conditions overrides the solution values at the boundaries. However, conflicts may arise when different conditions coincide at a particular boundary point. For example, in (4.35), both the inflow and wall boundary conditions coincide at the plate's leading edge. Meanwhile, the weak imposition of boundary solutions handles this paradox by penalizing the solution with the exact amount it deviates from data. Therefore, we will mimic the weak formulation (4.24) in the upcoming semi-discrete formulation.

4.3 Closing remarks

We applied the energy method and Green's theorem to the continuous problem (4.5) which led to the energy rate (4.6) consisting of the volume and boundary terms. The volume term is dissipative while the boundary terms are indefinite and could potentially lead to unbounded growth. We circumvented this by first rewriting them in a matrix-vector notation (4.7), then rotating the resulting boundary matrix M into a diagonal form using the matrix eigenvalue decomposition (4.8).

We further partitioned them into the positive and negative parts (4.14), and immediately noted that the negative component was problematic. This required us to express it in terms of the positive component and data, leading to the general energy stable boundary conditions (4.15). We proved that the strong imposition of these boundary conditions (both homogeneous and non-homogeneous) leads to energy estimates. We subsequently imposed them weakly (4.24) and obtained an even more dissipative energy rate.

A new set of energy stable boundary conditions specific to the flat plate laminar boundary layer problem were also proposed in (4.35). We also showed that they can be written in the general form (4.15), and that both their strong and weak imposition leads to identical energy rates (4.37), (4.53). In the next section, we will discretely mimic the analysis above, also summerized in Figure (4.1), and derive discrete estimates that have similar asymptotic temporal convergence as the continuous counterparts.

Chapter 5

SBP-SAT approximation for the IBL equations

We derive a stable approximation of the IBL equations (4.24) with the newly derived continuous form boundary conditions (4.35) in this chapter. As stated in the previous chapter, we only consider weak imposition of the boundary conditions. The spatial derivatives are approximated using finite difference operators on SBP form while keeping the temporal derivative continuous leading to a semi-discrete formulation. The boundary conditions are imposed weakly using the SAT technique which discretely imitates the boundary imposition (4.24). By following the guideline in Figure 4.1 in the discrete sense, we derive a discrete energy estimate that mimics the continuous counterpart, proving that the newly formulated SBP-SAT approximation is stable. Subsequently, we prove by plotting eigenvalues that the stable imposition of boundary conditions using the SAT method alleviates the incompressibility-related singularities associated with the nullspace of the differential operator. We conclude the chapter by discretizing the temporal derivative using the Backward Euler method, which leads to a fully discrete approximation.

5.1 The semi-discrete formulation

Let's consider domain $\Omega \in [0,1] \times [0,1]$ and discretize it using $\bar{N}+1$ and $\bar{M}+1$ equidistant grid points. Each grid point is given by pair a (x_i, y_j) where $x_i = i/\bar{N}$, $i = 0,1,2,\ldots,\bar{N}$ and $y_j = j/\bar{M}$, $j = 0,1,2,\ldots,\bar{M}$. We further arrange them as *row of column* vectors following the columnwise orientation as depicted in Figure 2.1. This arrangement allows us to represent a continuous function $h(x,y)$ evaluated on the grid points (x_i, y_j) as a vector $\mathbf{k} = (k_{00},\ldots,k_{0\bar{M}},\ldots,k_{\bar{N}0},\ldots,k_{\bar{N}\bar{M}})^T$, where $k_{ij} = k(x_i, y_j)$.

Remark 5.1. *To keep the subsequent derivations neater, we introduce the short-hand notations* $N = \bar{N}+1$ *and* $M = \bar{M}+1$.

Let $\mathbf{U} = [\mathbf{u}, \mathbf{v}, \mathbf{p}]^\mathsf{T}$ be an approximation solution of (4.24) where $\mathbf{u}, \mathbf{v}, \mathbf{p}$ respectively contain the discrete versions of u, v and p. Here, vectors $\mathbf{u}, \mathbf{v}, \mathbf{p}$ respectively have dimensions $NM \times 1$, and they are packaged in columnwise orientation. Further, we note that $\mathbf{U}$ is a $3NM \times 1$ vector. The boundary and initial data are arranged in a similar manner and denoted by vectors G and F, respectively.

The 2D SBP operators (2.31a) have $NM \times NM$ dimensions, respectively. Moreover, to ensure that these SBP matrices operate on the entire vector $\mathbf{U}$, we introduce the following notations

$$\begin{aligned} &\mathbf{P} = I_3 \otimes P_x \otimes P_y, \quad \mathbf{D}_x = I_3 \otimes P_x^{-1} Q_x \otimes I_M, \quad \mathbf{D}_y = I_3 \otimes I_N \otimes P_y^{-1} Q_x \\ &\mathbf{Q}_x = I_3 \otimes Q_x \otimes P_y, \quad \mathbf{Q}_y = I_3 \otimes P_x \otimes Q_y, \end{aligned} \tag{5.1}$$

where I_3, I_N, I_M are unit matrices of size 3×3, $N \times N$ and $M \times M$, respectively. Similarly, the SBP properties (2.31c) become

$$\mathbf{Q}_x + \mathbf{Q}_x^{\mathsf{T}} = I_3 \otimes (E_N - E_0) \otimes P_y \quad \text{and} \quad \mathbf{Q}_y + \mathbf{Q}_y^{\mathsf{T}} = I_3 \otimes (E_M - E_0) \otimes P_x, \tag{5.2}$$

where $E_0 = \text{diag}(1, 0, \ldots, 0)$, $E_N = \text{diag}(0, \ldots, 0, 1)$ and $E_M = \text{diag}(0, \ldots, 0, 1)$, with the appropriate sizes. With the notations in (5.1), we can compactly write the SBP approximations of the continuous derivatives in (4.1) as, for example, $U_x \approx \mathbf{D}_x \mathbf{U} = [D_x \mathbf{u}, D_x \mathbf{v}, D_x \mathbf{p}]^{\mathsf{T}}$ where $D_x = P_x^{-1} Q_x \otimes I_M$.

The semi-discrete approximation of (4.24) on SBP-SAT form is

$$\bar{\mathbf{I}} \mathbf{U}_t + \boldsymbol{\mathcal{D}}(\mathbf{U}) \mathbf{U} = \mathbb{SAT}, \tag{5.3a}$$

$$\bar{\mathbf{I}} \mathbf{U}(0) = F, \tag{5.3b}$$

where $\boldsymbol{\mathcal{D}}(\mathbf{U})$ is the discrete version of the spatial operator in (4.4) and is given by

$$\boldsymbol{\mathcal{D}}(\mathbf{U}) = \frac{1}{2} \left[\mathbf{A} \mathbf{D}_x + \mathbf{D}_x \mathbf{A} + \mathbf{B} \mathbf{D}_y + \mathbf{D}_y \mathbf{B} \right] - \nu \bar{\mathbf{I}} \mathbf{D}_y^2,$$

and $\mathbf{A}$, $\mathbf{B}$, $\bar{\mathbf{I}}$ are discrete versions of A, B and $\bar{I}$ in (4.1). By denoting unit and zero matrices of size $NM \times NM$ respectively with I_{NM} and $\mathbf{0}$, these matrices are

$$\mathbf{A} = \begin{bmatrix} \text{diag}(\mathbf{u}) & \mathbf{0} & I_{NM} \\ \mathbf{0} & \mathbf{0} & \mathbf{0} \\ I_{NM} & \mathbf{0} & \mathbf{0} \end{bmatrix}, \quad \mathbf{B} = \begin{bmatrix} \text{diag}(\mathbf{v}) & \mathbf{0} & \mathbf{0} \\ \mathbf{0} & \mathbf{0} & I_{NM} \\ \mathbf{0} & I_{NM} & \mathbf{0} \end{bmatrix}, \quad \bar{\mathbf{I}} = \begin{bmatrix} I_{NM} & \mathbf{0} & \mathbf{0} \\ \mathbf{0} & \mathbf{0} & \mathbf{0} \\ \mathbf{0} & \mathbf{0} & \mathbf{0} \end{bmatrix}.$$

In (5.3a), the $\mathbb{SAT}$ terms are the weakly implemented boundary conditions defined as

$$\begin{aligned} \mathbb{SAT} = &\mathbf{P}^{-1} \boldsymbol{\Sigma}_n (I_2 \otimes \mathbb{P}_n)(\mathcal{H}_n \mathbf{U} - G_n) + \mathbf{P}^{-1} \boldsymbol{\Sigma}_e \mathbb{P}_e (\mathcal{H}_e \mathbf{U} - G_e) \\ &+ \mathbf{P}^{-1} \boldsymbol{\Sigma}_n (I_2 \otimes \mathbb{P}_s)(\mathcal{H}_s \mathbf{U} - G_s) + \mathbf{P}^{-1} \boldsymbol{\Sigma}_w \mathbb{P}_w (\mathcal{H}_w \mathbf{U} - G_w), \end{aligned}$$

which discretely mimic $\mathbb{SAT}$ in (4.24). Here, $\boldsymbol{\Sigma}$, $\mathcal{H}$ and G denote the discrete penalty matrix, boundary operator and data, respectively, and their dimensions vary depending on the boundary. In Section 4.1.1, we inferred that two boundary conditions must be imposed at the horizontal boundaries and one boundary condition at the vertical boundaries. Therefore, the dimensions of $\mathcal{H}_{n,s}$, $\mathcal{H}_{e,w}$ are $2NM \times 3NM$ and $NM \times 3NM$, respectively. Similarly, the dimensions of $G_{n,s}$ and $G_{e,w}$ respectively are $2NM \times 1$ and $NM \times 1$. Lastly, to balance dimensions such that matrix multiplication is defined, $\boldsymbol{\Sigma}_{n,s}$, $\boldsymbol{\Sigma}_{e,w}$ must be matrices of size $3NM \times 2NM$ and $3NM \times NM$, respectively. We therefore rewrite $\mathbb{SAT}$ in compact form as

$$\mathbb{SAT} = \sum_{k \in \{n,s,e,w\}} \mathbf{P}^{-1} \boldsymbol{\Sigma}_k (I_j \otimes \mathbb{P}_k)(\mathcal{H}_k \mathbf{U} - G_k), \quad j = \begin{cases} 1 & \text{for} \quad k \in \{e, w\} \\ 2 & \text{for} \quad k \in \{n, s\} \end{cases},$$

where I_j denotes an identity matrix of size $j \times j$ and j is defined such that matrix multiplication is possible. It is equal to the number of boundary conditions prescribed per boundary. Lastly, the diagonal matrices $\mathbb{P}_k$ in (5.3a) are the quadrature rules approximating the boundary line integrals and they are defined in (2.31d). Further, we can write the SBP properties (5.2) as $\mathbf{Q}_x + \mathbf{Q}_x^\mathsf{T} = I_3 \otimes (\mathbb{P}_e - \mathbb{P}_w)$ and $\mathbf{Q}_y + \mathbf{Q}_y^\mathsf{T} = I_3 \otimes (\mathbb{P}_n - \mathbb{P}_s)$.

5.1.1 The discrete energy estimate

Next, we derive a discrete energy estimate that resembles the continuous counterpart. In Section 4.1.2, we imposed the boundary conditions (4.15) weakly in (4.24). We subsequently derived the penalty matrices in (4.28) which led to the continuous estimate. In this section, we endeavor to mimic the energy method discretely and show that the discrete version of these penalty coefficients lead to a stable approximation. The discrete energy method applied to (5.3a) which involves multiplying (5.3a) with $\mathbf{U}^\mathsf{T}\mathbf{P}$ and adding to its transpose yields

$$\frac{d}{dt}||\mathbf{U}||^2_{\bar{\mathbf{I}}\mathbf{P}} + \mathbf{U}^\mathsf{T}\big(\mathbf{P}\mathbf{A}\mathbf{D}_x + \mathbf{Q}_x\mathbf{A}\big)\mathbf{U} + \mathbf{U}^\mathsf{T}\big(\mathbf{P}\mathbf{B}\mathbf{D}_y + \mathbf{Q}_y\mathbf{B}\big)\mathbf{U} - 2\nu\mathbf{U}^\mathsf{T}\bar{\mathbf{I}}\mathbf{Q}_y\mathbf{D}_y\mathbf{U} = \mathbf{P}\mathbf{T}. \tag{5.4}$$

Here,

$$\begin{aligned}\mathbf{P}\mathbf{T} &= \mathbf{U}^\mathsf{T}\mathbb{S}\mathbb{A}\mathbb{T} + \Big(\mathbf{U}^\mathsf{T}\mathbb{S}\mathbb{A}\mathbb{T}\Big)^\mathsf{T} \\ &= \sum_{k\in\{n,s,e,w\}} \Big(\mathbf{U}^\mathsf{T}\mathbf{\Sigma}_k(I_j \otimes \mathbb{P}_k)(\mathcal{H}_k\mathbf{U} - G_k) + (\mathbf{U}^\mathsf{T}\mathbf{\Sigma}_k(I_j \otimes \mathbb{P}_k)(\mathcal{H}_k\mathbf{U} - G_k))^\mathsf{T}\Big),\end{aligned}$$

are the penalty terms mimicking the continuous counterparts in (4.25). In (5.4), $||\mathbf{U}||^2_{\bar{\mathbf{I}}\mathbf{P}} = \mathbf{U}^\mathsf{T}\bar{\mathbf{I}}\mathbf{P}\mathbf{U}$ is the discrete equivalence of the L_2-semi-norm. Next, we simplify the terms on the LHS of (5.4) separately. By starting with the nonlinear advection terms in the x-direction and applying the SBP property (5.2) on its conservative term, we rewrite it as

$$\begin{aligned}\mathbf{U}^\mathsf{T}\mathbf{P}\mathbf{A}(\mathbf{D}_x\mathbf{U}) + \mathbf{U}^\mathsf{T}\mathbf{Q}_x\mathbf{A}\mathbf{U} &= \mathbf{U}^\mathsf{T}\mathbf{P}\mathbf{A}(\mathbf{D}_x\mathbf{U}) - \mathbf{U}^\mathsf{T}\mathbf{Q}_x^\mathsf{T}\mathbf{P}^{-1}\mathbf{P}\mathbf{A}\mathbf{U} \\ &\quad + \mathbf{U}^\mathsf{T}(I_3 \otimes (\mathbb{P}_e - \mathbb{P}_w))\mathbf{A}\mathbf{U} \\ &= \mathbf{U}^\mathsf{T}\mathbf{P}\mathbf{A}(\mathbf{D}_x\mathbf{U}) - (\mathbf{D}_x\mathbf{U})^\mathsf{T}\mathbf{P}\mathbf{A}\mathbf{U} \\ &\quad + \mathbf{U}^\mathsf{T}(I_3 \otimes (\mathbb{P}_e - \mathbb{P}_w))\mathbf{A}\mathbf{U} \\ &= \mathbf{U}^\mathsf{T}(I_3 \otimes (\mathbb{P}_e - \mathbb{P}_w))\mathbf{A}\mathbf{U}.\end{aligned} \tag{5.5}$$

Notice that the non-conservative indefinite terms above vanish owing to the skew-symmetric flux splitting (4.3), and only the boundary terms remain. By applying a similar approach to the y advection terms in (5.4), we obtain

$$\mathbf{U}^\mathsf{T}\mathbf{P}\mathbf{B}(\mathbf{D}_y\mathbf{U}) + \mathbf{U}^\mathsf{T}\mathbf{Q}_y\mathbf{B}\mathbf{U} = \mathbf{U}^\mathsf{T}(I_3 \otimes (\mathbb{P}_n - \mathbb{P}_s))\mathbf{B}\mathbf{U}. \tag{5.6}$$

We consider the viscous term next, and use (5.2) to simplify them to

$$\begin{aligned}2\nu\mathbf{U}^\mathsf{T}\bar{\mathbf{I}}\mathbf{Q}_y(\mathbf{D}_y\mathbf{U}) &= 2\nu\mathbf{U}^\mathsf{T}(I_3 \otimes (\mathbb{P}_n - \mathbb{P}_s))\bar{\mathbf{I}}(\mathbf{D}_y\mathbf{U}) - 2\nu\mathbf{U}^\mathsf{T}\mathbf{Q}_y^\mathsf{T}\mathbf{P}^{-1}\mathbf{P}\bar{\mathbf{I}}(\mathbf{D}_y\mathbf{U}) \\ &= 2\nu\mathbf{U}^\mathsf{T}(I_3 \otimes (\mathbb{P}_n - \mathbb{P}_s))\bar{\mathbf{I}}(\mathbf{D}_y\mathbf{U}) - 2\nu(\mathbf{D}_y\mathbf{U})^\mathsf{T}\mathbf{P}\bar{\mathbf{I}}(\mathbf{D}_y\mathbf{U}).\end{aligned} \tag{5.7}$$

Here, we obtain both the boundary and the dissipative volume terms. Therefore, substituting (5.5), (5.6) and (5.7) into (5.4), transforms the energy rate to

$$\frac{d}{dt}||\mathbf{U}||^2_{\bar{\mathbf{I}}\mathbf{P}} + 2\nu||\mathbf{D}_y\mathbf{U}||^2_{\bar{\mathbf{I}}\mathbf{P}} = \widetilde{\mathbf{BT}} = \mathbf{BT} + \mathbf{PT} \tag{5.8}$$

where

$$\begin{aligned}\mathbf{BT} = &- \mathbf{U}^\mathsf{T}\left[(I_3 \otimes (\mathbb{P}_e + \mathbb{P}_w))\mathbf{A} - (I_3 \otimes (\mathbb{P}_n - \mathbb{P}_s))\mathbf{B}\right]\mathbf{U} \\ &+ 2\nu\mathbf{U}^\mathsf{T}(I_3 \otimes (\mathbb{P}_n - \mathbb{P}_s))\bar{\mathbf{I}}(\mathbf{D}_y\mathbf{U}),\end{aligned}$$

are the indefinite boundary terms resembling (4.6) discretely, and $\mathbf{PT}$ is given in (5.4). For later reference, we simplify $\mathbf{BT}$ further as

$$\begin{aligned}\mathbf{BT} = &- \big[\mathbf{u}^\mathsf{T}(\mathbb{P}_e - \mathbb{P}_w)\mathrm{diag}(\mathbf{u})\mathbf{u} + \mathbf{u}^\mathsf{T}(\mathbb{P}_n - \mathbb{P}_s)\mathrm{diag}(\mathbf{v})\mathbf{u} + 2\mathbf{u}^\mathsf{T}(\mathbb{P}_e - \mathbb{P}_w)\mathbf{p} \\ &+ 2\mathbf{v}^\mathsf{T}(\mathbb{P}_n - \mathbb{P}_s)\mathbf{p} - 2\nu\mathbf{u}^\mathsf{T}(\mathbb{P}_n - \mathbb{P}_s)D_y\mathbf{u}\big].\end{aligned}$$

The energy rate (5.8) is the discrete analogue of (4.25). Similar to the continuous case, the energy norm is bounded if $\widetilde{\mathbf{BT}}$ is non-positive or bounded by external data. We formalize this with the following Lemmas.

Lemma 9. *Approximation* (5.3) *with homogeneous boundary conditions is stable if* $\widetilde{\boldsymbol{BT}}$ *in* (5.8) *is non-negative.*

Proof. If $\widetilde{\mathbf{BT}} \leq 0$, then time integration in (5.8) leads to bounded discrete energy estimate

$$||\mathbf{U}||^2_{\bar{\mathbf{I}}\mathbf{P}} + 2\nu\int_0^T ||\mathbf{D}_y\mathbf{U}||^2_{\bar{\mathbf{I}}\mathbf{P}}dt \leq ||F||^2_{\bar{\mathbf{I}}\mathbf{P}}, \tag{5.9}$$

which is bounded by data and thus proving stability. □

Lemma 10. *Approximation* (5.3) *with non-homogeneous boundary conditions is strongly stable if* $\widetilde{\boldsymbol{BT}}$ *in* (5.8) *is bounded from above by data.*

Proof. Time integration in (5.8) over finite time domain $[0, T]$ leads to the discrete energy estimate

$$||\mathbf{U}||^2_{\bar{\mathbf{I}}\mathbf{P}}\big|_{t=0} + 2\nu\int_0^T ||\mathbf{D}_y\mathbf{U}||^2_{\bar{\mathbf{I}}\mathbf{P}}dt \leq ||F||^2_{\bar{\mathbf{I}}\mathbf{P}} + \int_0^T \left(\sum_{k\in\{n,s,e,w\}} G_k^\mathsf{T}\chi G_k\right)dt, \tag{5.10}$$

where χ is a bounded matrix. □

To proceed, we first rewrite $\mathbf{BT}$ in (5.8) in a form that resembles (4.7). Let the pair (N_x^k, N_y^k) be the discrete boundary normal matrices as defined below.

Definition 5.1. The discrete outward pointing boundary normals are given by the pair $N^k = (N_x^k, N_y^k)$

$$\begin{aligned}(N_x^n, N_y^n) &= (\mathbf{0}, I_N \otimes E_M), \\ (N_x^s, N_y^s) &= (\mathbf{0}, I_N \otimes -E_0), \\ (N_x^e, N_y^e) &= (E_N \otimes I_M, \mathbf{0}), \\ (N_x^w, N_y^w) &= (-E_0 \otimes I_M, \mathbf{0}),\end{aligned} \tag{5.11}$$

where the matrices E_1, $E_{N,M}$ and $I_{N,M}$, $\mathbf{0}$ are given in (5.2) and (5.3), respectively.

Using the notation above, we rewrite **BT** in (5.8) in a matrix-vector form as

$$\mathbf{BT} = -\sum_{k\in\{n,s,e,w\}} \widetilde{\mathbf{q}}^{\mathsf{T}}(I_4 \otimes \mathbb{P}_k)\boldsymbol{\mathcal{M}}\widetilde{\mathbf{q}}, \tag{5.12}$$

where

$$\widetilde{\mathbf{q}} = \begin{bmatrix} \mathbf{u} \\ \mathbf{v} \\ \mathbf{p} \\ \nu D_y \mathbf{u} \end{bmatrix}, \quad \boldsymbol{\mathcal{M}}_k = \begin{bmatrix} \mathrm{diag}(\mathbf{u}_\mathbf{n}^k) & \mathbf{0} & N_x^k & -N_y^k \\ \mathbf{0} & \mathbf{0} & N_y^k & \mathbf{0} \\ N_x^k & N_y^k & \mathbf{0} & \mathbf{0} \\ -N_y^k & \mathbf{0} & \mathbf{0} & \mathbf{0} \end{bmatrix},$$

are the discrete version of $\mathbf{q}$ and $\mathcal{M}$ in (4.7), respectively. Moreover, $\mathbf{u}_\mathbf{n}^k = N_x^k\mathbf{u} + N_y^k\mathbf{v}$ is the discrete boundary normal velocity. Since all the matrices in (5.12) are diagonal, then there are NM decoupled nonlinear equations. However, the number of nonzero entries is equal to the number of boundary grid points due to the normal matrices (5.11). By noting the similarity in the structures of $\mathcal{M}$ in (4.7) and $\boldsymbol{\mathcal{M}}$ in (5.12), we adopt the similar matrix eigenvalue decomposition (4.8) in the discrete sense

$$\boldsymbol{\mathcal{M}}_k = \mathbf{X}_k \boldsymbol{\Lambda}_k \mathbf{X}_k^{\mathsf{T}}, \tag{5.13}$$

for the k-th boundary. Here, $\boldsymbol{\Lambda}_k = \mathrm{diag}\big(\boldsymbol{\lambda}_1^k, \boldsymbol{\lambda}_2^k, \boldsymbol{\lambda}_3^k, \boldsymbol{\lambda}_4^k\big)$ is a $4NM \times 4NM$ diagonal matrix containing the eigenvalues of $\boldsymbol{\mathcal{M}}_k$ and $\mathbf{X}_k$ is the associated eigenvector block-matrix on the k-th boundary. Vectors $\boldsymbol{\lambda}_i^k$ contain pointwise eigenvalues of $\boldsymbol{\mathcal{M}}_k$ which are obtained by projecting (4.10) on the boundary grid points. For the north and south boundaries, $\boldsymbol{\lambda}_i^k$ and $\boldsymbol{X}^k$ are

$$\boldsymbol{\lambda}_1^k = \frac{\mathbf{u}_\mathbf{n}^k}{2} - \sqrt{\left(\frac{\mathbf{u}_\mathbf{n}^k}{2}\right)^2 + 1}, \quad \boldsymbol{\lambda}_2^k = -\vec{1}, \quad \boldsymbol{\lambda}_3^k = \vec{1}, \quad \boldsymbol{\lambda}_4^k = \frac{\mathbf{u}_\mathbf{n}^k}{2} + \sqrt{\left(\frac{\mathbf{u}_\mathbf{n}^k}{2}\right)^2 + 1}, \tag{5.14a}$$

$$\mathbf{X}_k = \begin{bmatrix} \mathrm{diag}(\boldsymbol{\lambda}_1^k) & \mathbf{0} & \mathbf{0} & \mathrm{diag}(\boldsymbol{\lambda}_4^k) \\ \mathbf{0} & \mathbf{I} & \mathbf{I} & \mathbf{0} \\ \mathbf{0} & N_y^k & N_y^k & \mathbf{0} \\ -N_y^k & \mathbf{0} & \mathbf{0} & -N_y^k \end{bmatrix}.$$

Similarly, at the east and west boundaries, they are

$$\boldsymbol{\lambda}_1^k = \frac{\mathbf{u}_\mathbf{n}^k}{2} - \sqrt{\left(\frac{\mathbf{u}_\mathbf{n}^k}{2}\right)^2 + 1}, \quad \boldsymbol{\lambda}_2^k = \vec{0}, \quad \boldsymbol{\lambda}_3^k = \vec{0}, \quad \boldsymbol{\lambda}_4^k = \frac{\mathbf{u}_\mathbf{n}^k}{2} + \sqrt{\left(\frac{\mathbf{u}_\mathbf{n}^k}{2}\right)^2 + 1}, \tag{5.14b}$$

$$\mathbf{X}_k = \begin{bmatrix} \mathrm{diag}(\boldsymbol{\lambda}_1^k) & \mathbf{0} & \mathbf{0} & \mathrm{diag}(\boldsymbol{\lambda}_4^k) \\ \mathbf{0} & N_x^k & \mathbf{0} & \mathbf{0} \\ N_x^k & \mathbf{0} & \mathbf{0} & N_x^k \\ \mathbf{0} & \mathbf{0} & N_x^k & \mathbf{0} \end{bmatrix},$$

where $\vec{1}$, $\vec{0}$ respectively denote vector of ones and zeros.

Remark 5.2. *The square-roots and multiplications in* (5.14) *should be interpreted element-wise. For subsequent analysis, all operations involving* $\boldsymbol{\lambda}_i$ *should also be interpreted element-wise.*

By substituting (5.13) into (5.12) and defining the discrete characteristic variables $\mathbf{W}^k = \mathbf{X}_k\widetilde{\mathbf{q}}^{\mathsf{T}}$, (5.12) becomes

$$\mathbf{BT} = -\sum_{k\in\{n,s,e,w\}} \mathbf{W}^{k,\mathsf{T}}(I_4 \otimes \mathbb{P}_k)\mathbf{\Lambda}_k\mathbf{W}^k. \tag{5.15}$$

We further imitate the continuous relation (4.14) and divide it in terms of the positive and negative components as

$$\mathbf{BT} = -\sum_{k\in\{n,s,e,w\}} \begin{bmatrix}\mathbf{W}_+^k\\ \mathbf{W}_-^k\end{bmatrix}^{\mathsf{T}} (I_{2j} \otimes \mathbb{P}_k) \begin{bmatrix}\mathbf{\Lambda}_k^+ & \mathbf{0}\\ \mathbf{0} & \mathbf{\Lambda}_k^-\end{bmatrix} \begin{bmatrix}\mathbf{W}_+^k\\ \mathbf{W}_-^k\end{bmatrix}. \tag{5.16}$$

The variables in (5.16) are the discrete analogues of (4.14). For the north and south boundaries, they are defined as

$$\begin{aligned}
\mathbf{\Lambda}_k^+ &= \begin{bmatrix}\operatorname{diag}(\boldsymbol{\lambda}_3^k/2) & \mathbf{0}\\ \mathbf{0} & \operatorname{diag}\big(\boldsymbol{\lambda}_4^k/((\boldsymbol{\lambda}_4^k)^2+1)\big)\end{bmatrix}, \quad \mathbf{W}_+^k = \begin{bmatrix}\mathbf{v} + N_y^k\mathbf{p}\\ \boldsymbol{\lambda}_4^k\mathbf{u} - \nu N_y^k D_y\mathbf{u}\end{bmatrix},\\
\mathbf{\Lambda}_k^- &= \begin{bmatrix}\operatorname{diag}\left(\boldsymbol{\lambda}_1^k/((\boldsymbol{\lambda}_1^k)^2+1)\right) & \mathbf{0}\\ \mathbf{0} & \operatorname{diag}\left(\boldsymbol{\lambda}_2^k/2\right)\end{bmatrix}, \quad \mathbf{W}_-^k = \begin{bmatrix}\boldsymbol{\lambda}_1^k\mathbf{u} - \nu N_y^k D_y\mathbf{u}\\ \mathbf{v} - N_y^k\mathbf{p}\end{bmatrix}.
\end{aligned} \tag{5.17a}$$

For the east and west boundaries, we have

$$\begin{aligned}
\mathbf{\Lambda}_+^k &= \left[\operatorname{diag}\big(\boldsymbol{\lambda}_4^k/((\boldsymbol{\lambda}_4^k)^2+1)\big)\right], \quad \mathbf{W}_+^k = \left[\boldsymbol{\lambda}_4^k\mathbf{u} + N_x^k\mathbf{p}\right],\\
\mathbf{\Lambda}_-^k &= \left[\operatorname{diag}\big(\boldsymbol{\lambda}_1^k/((\boldsymbol{\lambda}_1^k)^2+1)\big)\right]. \quad \mathbf{W}_-^k = \left[\boldsymbol{\lambda}_1^k\mathbf{u} + N_x^k\mathbf{p}\right]
\end{aligned} \tag{5.17b}$$

Note that in (5.16), we adjusted the dimensions of the unit matrix to $2j$ since $\mathbf{W} = [\mathbf{W}_+, \mathbf{W}_-]^{\mathsf{T}}$ has two vectors and index j is defined as before. Next, we define the discrete version of the boundary condition (4.15)

$$\mathcal{H}_k\mathbf{U} = \mathbf{W}_-^k - \boldsymbol{\mathcal{R}}_k\mathbf{W}_+^k, \tag{5.18}$$

where $\boldsymbol{\mathcal{R}}$ is the discrete version of $\mathcal{R}$. We rewrite $\mathbf{PT}$ in (5.4) in terms of the variables (5.17) as

$$\begin{aligned}
\mathbf{PT} = \sum_{k\in\{n,s,e,w\}} &\big(\mathbf{U}^{\mathsf{T}}\mathbf{\Sigma}_k(I_j \otimes \mathbb{P}_k)(\mathbf{W}_-^k - \boldsymbol{\mathcal{R}}_k\mathbf{W}_+^k - G_k)\\
&+ (\mathbf{U}^{\mathsf{T}}\mathbf{\Sigma}_k(I_j \otimes \mathbb{P}_k)(\mathbf{W}_-^k - \boldsymbol{\mathcal{R}}_k\mathbf{W}_+^k - G_k))^{\mathsf{T}}\big).
\end{aligned} \tag{5.19}$$

Further, by using (5.16) and (5.19), we rewrite $\widetilde{\mathbf{BT}}$ in (5.4) as

$$\begin{aligned}
\widetilde{\mathbf{BT}} = -\sum_{k\in\{n,s,e,w\}} \Bigg(&\begin{bmatrix}\mathbf{W}_+^k\\ \mathbf{W}_-^k\end{bmatrix}^{\mathsf{T}} (I_{2j} \otimes \mathbb{P}_k) \begin{bmatrix}\mathbf{\Lambda}_k^+ & \mathbf{0}\\ \mathbf{0} & \mathbf{\Lambda}_k^-\end{bmatrix} \begin{bmatrix}\mathbf{W}_+^k\\ \mathbf{W}_-^k\end{bmatrix}\\
&+ \mathbf{U}^{\mathsf{T}}\mathbf{\Sigma}_k(I_j \otimes \mathbb{P}_k)(\mathbf{W}_-^k - \boldsymbol{\mathcal{R}}_k\mathbf{W}_+^k - G_k)\\
&+ (\mathbf{U}^{\mathsf{T}}\mathbf{\Sigma}_k(I_j \otimes \mathbb{P}_k)(\mathbf{W}_-^k - \boldsymbol{\mathcal{R}}_k\mathbf{W}_+^k - G_k))^{\mathsf{T}}\Bigg),
\end{aligned} \tag{5.20}$$

which is a discrete equivalence of (4.26). Next, we combine the sums in (5.20) by making the ansatz $\mathbf{U}^{\mathsf{T}}\mathbf{\Sigma} = \mathbf{W}_-\widetilde{\mathbf{\Sigma}}$ which resembles (4.28). Therefore, $\widetilde{\mathbf{BT}}$ becomes

$$\widetilde{\mathbf{BT}} = -\sum_{k\in\{n,s,e,w\}} \begin{bmatrix}\mathbf{W}_+^k\\ \mathbf{W}_-^k\\ G_k\end{bmatrix}^{\mathsf{T}} (I_{3j} \otimes \mathbb{P}_k) \begin{bmatrix}\mathbf{\Lambda}_k^+ & (\widetilde{\mathbf{\Sigma}}_k\boldsymbol{\mathcal{R}}_k)^{\mathsf{T}} & \mathbf{0}\\ \widetilde{\mathbf{\Sigma}}_k\boldsymbol{\mathcal{R}}_k & \mathbf{\Lambda}_k^- - (\widetilde{\mathbf{\Sigma}}_k + \widetilde{\mathbf{\Sigma}}_k^{\mathsf{T}}) & \widetilde{\mathbf{\Sigma}}_k\\ \mathbf{0} & \widetilde{\mathbf{\Sigma}}_k^{\mathsf{T}} & \mathbf{0}\end{bmatrix} \begin{bmatrix}\mathbf{W}_+^k\\ \mathbf{W}_-^k\\ G_k\end{bmatrix}, \tag{5.21}$$

which is a discrete analogue of (4.29). Similarly here, our ambition is to determine $\boldsymbol{\mathcal{R}}$ and $\widetilde{\boldsymbol{\Sigma}}$ such that $\widetilde{\mathbf{BT}}$ is non-positive or bounded by data. Starting with homogeneous boundary conditions, we formulate the discrete equivalence of Proposition 4.

Proposition 11. *The discrete boundary term* (5.21) *with* $G_k = 0$ *is non-negative if* $\boldsymbol{\mathcal{R}}_k$ *satisfies* $\boldsymbol{\Lambda}_k^+ + \boldsymbol{\mathcal{R}}_k^\mathsf{T}\boldsymbol{\Lambda}_k^-\boldsymbol{\mathcal{R}}_k \geq \boldsymbol{0}$ *and* $\widetilde{\boldsymbol{\Sigma}}_k = \boldsymbol{\Lambda}_k^-$.

Proof. Substituting $\widetilde{\boldsymbol{\Sigma}}_k = \boldsymbol{\Lambda}_k^-$ and $G_k = 0$ into (5.21) leads to

$$\widetilde{\mathbf{BT}} = -\sum_{k\in\{n,s,e,w\}} \begin{bmatrix}\mathbf{W}_+^k\\ \mathbf{W}_-^k\end{bmatrix}^\mathsf{T} (I_{2j}\otimes\mathbb{P}_k) \begin{bmatrix}\boldsymbol{\Lambda}_k^+ & (\boldsymbol{\Lambda}_k^-\boldsymbol{\mathcal{R}}_k)^\mathsf{T}\\ \boldsymbol{\Lambda}_k^-\boldsymbol{\mathcal{R}}_k & -\boldsymbol{\Lambda}_k^-\end{bmatrix} \begin{bmatrix}\mathbf{W}_+^k\\ \mathbf{W}_-^k\end{bmatrix}.$$

By further adding and subtracting $(\boldsymbol{\mathcal{R}}_k\mathbf{W}_+^k)^\mathsf{T}(I_j\otimes\mathbb{P}_k)\boldsymbol{\Lambda}_k^-(\boldsymbol{\mathcal{R}}_k\mathbf{W}_+^k)$, the above can be written as

$$\begin{aligned}\widetilde{\mathbf{BT}} = &-\mathbf{W}_+^{k,\mathsf{T}}(I_j\otimes\mathbb{P}_k)\left[\boldsymbol{\Lambda}_k^+ + \boldsymbol{\mathcal{R}}_k^\mathsf{T}\boldsymbol{\Lambda}_k^-\boldsymbol{\mathcal{R}}_k\right]\mathbf{W}_+^k\\ &+(\mathbf{W}_-^k - \boldsymbol{\mathcal{R}}_k\mathbf{W}_+^k)^\mathsf{T}(I_{2j}\otimes\mathbb{P}_k)\boldsymbol{\Lambda}_k^-(\mathbf{W}_-^k - \boldsymbol{\mathcal{R}}_k\mathbf{W}_+^k),\end{aligned}$$

which is a discrete version of (4.30). Therefore, $\widetilde{\mathbf{BT}} \leq 0$ if $\boldsymbol{\mathcal{R}}_k$ exists such that it satisfies

$$\boldsymbol{\Lambda}_k^+ + \boldsymbol{\mathcal{R}}_k^\mathsf{T}\boldsymbol{\Lambda}_k^-\boldsymbol{\mathcal{R}}_k \geq 0. \tag{5.22}$$

This inequality is also the discrete analogue of (4.18). □

The energy rate (5.8) is bounded and hence the approximation (5.3) is stable using Lemma 9. The next case we are considering is (5.20) with nonzero boundary data.

Proposition 12. *The discrete boundary term* (5.20) *with* $G_k \neq 0$ *and* $\tilde{\boldsymbol{\Sigma}}_k = \boldsymbol{\Lambda}_k^-$ *is bounded by data if we can find* $\boldsymbol{\mathcal{R}}_k$ *and* $\boldsymbol{\Xi}$ *satisfying* $(\boldsymbol{\mathcal{R}}_k\boldsymbol{\Lambda}_k^-)(\boldsymbol{\Lambda}_k^+ + \boldsymbol{\mathcal{R}}_k^\mathsf{T}\boldsymbol{\Lambda}_k^-\boldsymbol{\mathcal{R}}_k)^{-1}(\boldsymbol{\mathcal{R}}_k\boldsymbol{\Lambda}_k^-)^\mathsf{T} \leq \boldsymbol{\Xi} < \infty$ *and* $\boldsymbol{\Lambda}_k^+ + \boldsymbol{\mathcal{R}}_k^\mathsf{T}\boldsymbol{\Lambda}_k^-\boldsymbol{\mathcal{R}}_k > 0$.

Proof. Let $\widetilde{\boldsymbol{\Sigma}}_k = \boldsymbol{\Lambda}_k^-$ and $\boldsymbol{\Xi} < \infty$ exist, then adding and subtracting $G_k^\mathsf{T}(I_j\otimes\mathbb{P}_k)\boldsymbol{\Xi}G_k\big|_{k\in\{n,s,e,w\}}$ to (5.20) yields

$$\begin{aligned}\widetilde{\mathbf{BT}} = -\sum_{k\in\{n,s,e,w\}} \Bigg(&\begin{bmatrix}\mathbf{W}_+^k\\ \mathbf{W}_-^k\\ G_k\end{bmatrix}^\mathsf{T} (I_{3j}\otimes\mathbb{P}_k) \begin{bmatrix}\boldsymbol{\Lambda}_k^+ & (\boldsymbol{\Lambda}_k^-\boldsymbol{\mathcal{R}}_k)^\mathsf{T} & \mathbf{0}\\ \boldsymbol{\Lambda}_k^-\boldsymbol{\mathcal{R}}_k & -\boldsymbol{\Lambda}_k^- & \boldsymbol{\Lambda}_k^-\\ \mathbf{0} & \boldsymbol{\Lambda}_k^- & \boldsymbol{\Xi}\end{bmatrix} \begin{bmatrix}\mathbf{W}_+^k\\ \mathbf{W}_-^k\\ G_k\end{bmatrix}\\ &+G_k^\mathsf{T}(I_j\otimes\mathbb{P}_k)\boldsymbol{\Xi}G_k\Bigg),\end{aligned} \tag{5.23}$$

which is discretely identical to (4.32). By employing the discrete analogue of the matrix splitting technique (4.33)

$$\begin{aligned}\begin{bmatrix}\boldsymbol{\Lambda}_k^+ & (\boldsymbol{\Lambda}_k^-\boldsymbol{\mathcal{R}}_k)^\mathsf{T} & \mathbf{0}\\ \boldsymbol{\Lambda}_k^-\boldsymbol{\mathcal{R}}_k & -\boldsymbol{\Lambda}_k^- & \boldsymbol{\Lambda}_k^-\\ \mathbf{0} & \boldsymbol{\Lambda}_k^- & \boldsymbol{\Xi}\end{bmatrix} = &\begin{bmatrix}\boldsymbol{\Lambda}_k^+ + \boldsymbol{\mathcal{R}}_k^\mathsf{T}\boldsymbol{\Lambda}_k^-\boldsymbol{\mathcal{R}}_k & \mathbf{0} & (\boldsymbol{\Lambda}_k^-\boldsymbol{\mathcal{R}}_k)^\mathsf{T}\\ \mathbf{0} & \mathbf{0} & \mathbf{0}\\ \boldsymbol{\Lambda}_k^-\boldsymbol{\mathcal{R}}_k & \mathbf{0} & \boldsymbol{\Lambda}_k^- + \boldsymbol{\Xi}\end{bmatrix}\\ &+\begin{bmatrix}-\boldsymbol{\mathcal{R}}_k^\mathsf{T}\boldsymbol{\Lambda}_k^-\boldsymbol{\mathcal{R}}_k & (\boldsymbol{\Lambda}_k^-\boldsymbol{\mathcal{R}}_k)^\mathsf{T} & -(\boldsymbol{\Lambda}_k^-\boldsymbol{\mathcal{R}}_k)^\mathsf{T}\\ \boldsymbol{\Lambda}_k^-\boldsymbol{\mathcal{R}}_k & -\boldsymbol{\Lambda}_k^- & \boldsymbol{\Lambda}_k^-\\ -\boldsymbol{\Lambda}_k^-\boldsymbol{\mathcal{R}}_k & \boldsymbol{\Lambda}_k^- & -\boldsymbol{\Lambda}_k^-\end{bmatrix},\end{aligned} \tag{5.24}$$

which transform (5.23) into

$$\widetilde{\mathbf{BT}} = \sum_{k\in\{n,s,e,w\}} \left(\widetilde{\mathbf{BT}}_1 + \widetilde{\mathbf{BT}}_2 + \widetilde{\mathbf{BT}}_3\right)_k, \tag{5.25}$$

where

$$\widetilde{\mathbf{BT}}_1 = (\mathbf{W}_-^k - \boldsymbol{\mathcal{R}}_k\mathbf{W}_+^k - G_k)^{\mathsf{T}}(I_{2j}\otimes\mathbb{P}_k)\boldsymbol{\Lambda}_k^-(\mathbf{W}_-^k - \boldsymbol{\mathcal{R}}_k\mathbf{W}_+^k - G_k),$$

$$\widetilde{\mathbf{BT}}_2 = -\begin{bmatrix}\mathbf{W}_+^k\\ G_k\end{bmatrix}^{\mathsf{T}}(I_{2j}\otimes\mathbb{P}_k)\underbrace{\begin{bmatrix}\boldsymbol{\Lambda}_k^+ + \boldsymbol{\mathcal{R}}_k^{\mathsf{T}}\boldsymbol{\Lambda}_k^-\boldsymbol{\mathcal{R}}_k & (\boldsymbol{\Lambda}_k^-\boldsymbol{\mathcal{R}}_k)^{\mathsf{T}}\\ \boldsymbol{\Lambda}_k^-\boldsymbol{\mathcal{R}}_k & \boldsymbol{\Lambda}_k^- + \boldsymbol{\Xi}\end{bmatrix}}_{\boldsymbol{\Theta}}\begin{bmatrix}\mathbf{W}_+^k\\ G_k\end{bmatrix},$$

$$\widetilde{\mathbf{BT}}_3 = G_k^{\mathsf{T}}(I_j\otimes\mathbb{P}_k)\boldsymbol{\Xi}G_k.$$

Here, $\widetilde{\mathbf{BT}}$ imitates (4.33) discretely and it is bounded by data if $\widetilde{\mathbf{BT}}_1$, $\widetilde{\mathbf{BT}}_2$ are non-negative and $\boldsymbol{\Xi}$ is finite. In (5.25), $\widetilde{\mathbf{BT}}_1$ is clearly negative since $\boldsymbol{\Lambda}_k^-$ is negative. It remains to show that $\widetilde{\mathbf{BT}}_2$ is non-negative as well i.e. we show that $\boldsymbol{\Theta}$ is positive semi-definite since it multiplied with a negative sign in (5.25).

Lemma 13. *Matrix* $\boldsymbol{\Theta}$ *in* (5.25) *is positive semi-definite if* $(\boldsymbol{\mathcal{R}}_k\boldsymbol{\Lambda}_k^-)(\boldsymbol{\Lambda}_k^+ + \boldsymbol{\mathcal{R}}_k^{\mathsf{T}}\boldsymbol{\Lambda}_k^-\boldsymbol{\mathcal{R}}_k)^{-1}(\boldsymbol{\mathcal{R}}_k\boldsymbol{\Lambda}_k^-)^{\mathsf{T}} - \boldsymbol{\Lambda}_k^- \le \boldsymbol{\Xi} < \infty$ *and* $\boldsymbol{\Lambda}_k^+ + \boldsymbol{\mathcal{R}}_k^{\mathsf{T}}\boldsymbol{\Lambda}_k^-\boldsymbol{\mathcal{R}}_k > 0$.

Proof. We adopt a similar matrix rotation technique as in (4.20) and transform $\boldsymbol{\Theta}$ to a block-diagonal matrix. By first considering the rotation matrix

$$\mathcal{N} = \begin{bmatrix}\mathbf{I} & -(\boldsymbol{\Lambda}_k^+ + \boldsymbol{\mathcal{R}}_k^{\mathsf{T}}\boldsymbol{\Lambda}_k^-\boldsymbol{\mathcal{R}}_k)^{-1}(\boldsymbol{\mathcal{R}}_k\boldsymbol{\Lambda}_k^-)^{\mathsf{T}}\\ \mathbf{0} & \mathbf{I}\end{bmatrix},$$

the rotated form of $\boldsymbol{\Theta}$ is computed as

$$\begin{aligned}\boldsymbol{\Upsilon} &= \mathcal{N}^{\mathsf{T}}\boldsymbol{\Theta}\mathcal{N} \\ &= \begin{bmatrix}\boldsymbol{\Lambda}_k^+ + \boldsymbol{\mathcal{R}}_k^{\mathsf{T}}\boldsymbol{\Lambda}_k^-\boldsymbol{\mathcal{R}}_k & \mathbf{0}\\ \mathbf{0} & \boldsymbol{\Lambda}_k^- + \boldsymbol{\Xi} - (\boldsymbol{\mathcal{R}}_k\boldsymbol{\Lambda}_k^-)(\boldsymbol{\Lambda}_k^+ + \boldsymbol{\mathcal{R}}_k^{\mathsf{T}}\boldsymbol{\Lambda}_k^-\boldsymbol{\mathcal{R}}_k)^{-1}(\boldsymbol{\mathcal{R}}_k\boldsymbol{\Lambda}_k^-)^{\mathsf{T}}\end{bmatrix},\end{aligned} \tag{5.26}$$

which is discretely identical to (4.21). Further, it is positive semi-definite if the inequalities in Proposition 12 holds. □

The results above prove that $\widetilde{\mathbf{BT}}$ in (5.25) is bounded by data which completes the proof. □

5.1.2 Stable approximation of the Blasius boundary layer equations

Next, we show that the discrete counterparts of the boundary conditions (4.35) and the penalty coefficients (4.49) lead to an energy estimate that mimics the continuous counterpart (4.38). The discrete boundary conditions and penalty matrices are

$$\mathcal{H}_e\mathbf{U} = \begin{bmatrix}\mathbf{0} & \mathbf{0} & \mathbf{I}\end{bmatrix}\begin{bmatrix}\mathbf{u}\\ \mathbf{v}\\ \mathbf{p}\end{bmatrix} = \begin{bmatrix}\mathbf{p}_\infty\end{bmatrix}, \quad \mathcal{H}_s\mathbf{U} = \begin{bmatrix}\mathbf{I} & \mathbf{0} & \mathbf{0}\\ \mathbf{0} & \mathbf{I} & \mathbf{0}\end{bmatrix}\begin{bmatrix}\mathbf{u}\\ \mathbf{v}\\ \mathbf{p}\end{bmatrix} = \begin{bmatrix}\mathbf{0}\\ \mathbf{0}\end{bmatrix}, \tag{5.27a}$$

$$\mathcal{H}_w\mathbf{U} = \begin{bmatrix}\mathbf{I} & \mathbf{0} & \mathbf{0}\end{bmatrix}\begin{bmatrix}\mathbf{u}\\ \mathbf{v}\\ \mathbf{p}\end{bmatrix} = \begin{bmatrix}\mathbf{u}_\infty\end{bmatrix}, \quad \mathcal{H}_n\mathbf{U} = \begin{bmatrix}\frac{\vartheta}{2}\mathrm{diag}(\mathbf{u}_\mathbf{n}^n) - \nu D_y & \mathbf{0} & \mathbf{0}\\ \mathbf{0} & \mathbf{0} & \mathbf{I}\end{bmatrix}\begin{bmatrix}\mathbf{u}\\ \mathbf{v}\\ \mathbf{p}\end{bmatrix} = \begin{bmatrix}\mathbf{0}\\ \mathbf{p}_\infty\end{bmatrix},$$

and

$$\mathbf{\Sigma}_s = \begin{bmatrix} \frac{1}{2}\text{diag}(\mathbf{u}_\mathbf{n}^s) - \nu D_y^\mathsf{T} N_y^s & \mathbf{0} \\ \mathbf{0} & \mathbf{0} \\ \mathbf{0} & N_y^s \end{bmatrix}, \quad \mathbf{\Sigma}_n = \begin{bmatrix} N_y^n & \mathbf{0} \\ \mathbf{0} & N_y^n \\ \mathbf{0} & \mathbf{0} \end{bmatrix}, \tag{5.27b}$$

$$\mathbf{\Sigma}_w = \begin{bmatrix} \frac{1}{2}\text{diag}(\mathbf{u}_\mathbf{n}^w) \\ \mathbf{0} \\ N_x^w \end{bmatrix}, \quad \mathbf{\Sigma}_e = \begin{bmatrix} N_x^e \\ \mathbf{0} \\ \mathbf{0} \end{bmatrix},$$

respectively. Using the above, the penalty terms in (5.3a) simplify to

$$\mathbf{P}^{-1}\mathbf{\Sigma}_s\mathbb{P}_s\mathcal{H}_s\mathbf{U} = \begin{bmatrix} (P_x \otimes P_y)^{-1}\left(\frac{1}{2}\text{diag}(\mathbf{u}_\mathbf{n}^s)\mathbb{P}_s\mathbf{u} - \nu D_y^\mathsf{T} N_y^s \mathbb{P}_s\mathbf{u}\right) \\ \mathbf{0} \\ (P_x \otimes P_y)^{-1} N_y^s \mathbb{P}_s\mathbf{v} \end{bmatrix}, \tag{5.28a}$$

$$\mathbf{P}^{-1}\mathbf{\Sigma}_n\mathbb{P}_n\mathcal{H}_n\mathbf{U} = \begin{bmatrix} (P_x \otimes P_y)^{-1}\left(\frac{\vartheta}{2}\mathbb{P}_n\text{diag}(\mathbf{u}_\mathbf{n}^n)\mathbf{u} - \nu N_y^n\mathbb{P}_n D_y\mathbf{u}\right) \\ (P_x \otimes P_y)^{-1} N_y^n \mathbb{P}_n\mathbf{p} \\ \mathbf{0} \end{bmatrix}, \tag{5.28b}$$

$$\mathbf{P}^{-1}\mathbf{\Sigma}_e\mathbb{P}_e\mathcal{H}_e\mathbf{U} = \begin{bmatrix} (P_x \otimes P_y)^{-1} N_x^e \mathbb{P}_e\mathbf{p} \\ \mathbf{0} \\ \mathbf{0} \end{bmatrix}, \tag{5.28c}$$

$$\mathbf{P}^{-1}\mathbf{\Sigma}_w\mathbb{P}_w\mathcal{H}_w\mathbf{U} = \begin{bmatrix} \frac{1}{2}(P_x \otimes P_y)^{-1}\text{diag}(\mathbf{u}_\mathbf{n}^w)\mathbb{P}_w\mathbf{u} \\ \mathbf{0} \\ (P_x \otimes P_y)^{-1} N_x^w \mathbb{P}_w\mathbf{u} \end{bmatrix}. \tag{5.28d}$$

Furthermore, substituting (5.28) with zero data into (5.4) simplifies $\mathbf{PT}$ to

$$\begin{aligned} \mathbf{PT} = &\left[\vartheta\mathbf{u}^\mathsf{T}\text{diag}(\mathbf{u}_\mathbf{n}^n)\mathbb{P}_n\mathbf{u} + 2\mathbf{u}_\mathbf{n}^{n,\mathsf{T}}\mathbb{P}_n\mathbf{p} - 2\nu\mathbf{u}^\mathsf{T} N_y^n\mathbb{P}_n(D_y\mathbf{u})\right] + \left[2\mathbf{u}_\mathbf{n}^{e,\mathsf{T}}\mathbb{P}_e\mathbf{p}\right] \\ &+ \left[\mathbf{u}^\mathsf{T}\text{diag}(\mathbf{u}_\mathbf{n}^s)\mathbb{P}_s\mathbf{u} + 2\mathbf{p}^\mathsf{T}\mathbb{P}_s\mathbf{u}_\mathbf{n}^s - 2\nu(D_y\mathbf{u})^\mathsf{T} N_y^s\mathbb{P}_s\mathbf{u}\right] \\ &+ \left[\mathbf{u}^\mathsf{T}\text{diag}(\mathbf{u}_\mathbf{n}^w)\mathbb{P}_w\mathbf{u} + 2\mathbf{p}^\mathsf{T}\mathbb{P}_w\mathbf{u}_\mathbf{n}^w\right], \end{aligned} \tag{5.29}$$

which mimics (4.50) discretely. Lastly, substituting (5.29) into (5.8) lead to the cancellation of several terms and the energy rate becomes

$$\frac{d}{dt}||\mathbf{U}||^2_{\mathbf{IP}} + 2\nu||\mathbf{D}_y\mathbf{U}||^2_{\mathbf{IP}} = \widetilde{\mathbf{BT}} = -(1-\vartheta)\mathbf{u}^\mathsf{T}\text{diag}(\mathbf{u}_\mathbf{n}^n)\mathbb{P}_n\mathbf{u} - \mathbf{u}^\mathsf{T}\text{diag}(\mathbf{u}_\mathbf{n}^e)\mathbb{P}_e\mathbf{u} \leq 0, \tag{5.30}$$

which mimics (4.51) discretely. We recall that $\text{diag}(\mathbf{u}_\mathbf{n}^n) > 0$ and $\text{diag}(\mathbf{u}_\mathbf{n}^s) > 0$, and therefore time integration leads to the estimate (5.9) which proves that the approximation (5.3) using (5.27) – (5.28) is stable.

5.2 The nullspace of discrete spatial operator

A key contribution of this work is to develop a stable approximation for the IBL equations in their original form i.e. without manipulating the continuity equation. As alluded earlier, the spatial operator $\boldsymbol{\mathcal{D}}(\mathbf{U})$ in (5.3a) is singular and could potentially lead to nonphysical growth in the solution. In the previous section, we obtained stability by amalgamating $\boldsymbol{\mathcal{D}}$ with the energy stable boundary conditions using the SBP-SAT framework. In this section, we intend to investigate the effect of imposing boundary conditions such that the nullspace of $\boldsymbol{\mathcal{D}}$ is removed. We return to (5.3a) and write out the spatial operator as

$$\boldsymbol{\mathcal{D}}(\mathbf{U}) = \left[\begin{array}{c|c|c} \frac{1}{2}\big[\mathrm{diag}(\mathbf{u})D_x + D_x\mathrm{diag}(\mathbf{u}) + \mathrm{diag}(\mathbf{v})D_y & \mathbf{0} & D_x \\ +D_y\mathrm{diag}(\mathbf{v})\big] - \nu D_y^2 & & \\ \hline \mathbf{0} & \mathbf{0} & D_y \\ \hline D_x & D_y & \mathbf{0} \end{array}\right]. \tag{5.31}$$

The difference operators D_x, D_y in (5.31) are singular by construction (since they are constructed on the central difference stencil). Therefore, without the inclusion of the boundary conditions, the coefficients of the system $\boldsymbol{\mathcal{D}}(\mathbf{U})\mathbf{U} = \mathbf{0}$ are singular. As mentioned before, the singularity emanating from (5.31) is typically circumvented by creating a relationship between the velocity divergence relation and the pressure. Essentially, these approaches populate the nonzero pressure values on the main diagonal. We however have already established that they are inefficient since they introduce numerical errors and require additional boundary conditions. The SAT technique on the other hand elegantly removes the singularity. To see this, let $\widetilde{\boldsymbol{\mathcal{D}}}$ denote the spatial operator with SAT homogeneous boundary conditions (5.28) included

$$\widetilde{\boldsymbol{\mathcal{D}}}(\mathbf{U}) = \boldsymbol{\mathcal{D}}(\mathbf{U}) - \nu\boldsymbol{\mathcal{I}}\mathbf{D}_y^2 - \sum_{k\in\{n,s,e,w\}} \mathbf{P}^{-1}\boldsymbol{\Sigma}_k(I_j \otimes \mathbb{P}_k)\mathcal{H}_k \tag{5.32}$$

$$= \begin{bmatrix} \widetilde{\mathcal{D}}_{11} & \mathbf{0} & \widetilde{\mathcal{D}}_{13} \\ \mathbf{0} & \mathbf{0} & \widetilde{\mathcal{D}}_{23} \\ \widetilde{\mathcal{D}}_{31} & \widetilde{\mathcal{D}}_{32} & \mathbf{0} \end{bmatrix} \tag{5.33}$$

where

$$\begin{aligned} \widetilde{\mathcal{D}}_{11} &= \mathrm{diag}(\mathbf{u})D_x + D_x\mathrm{diag}(\mathbf{u}) + \mathrm{diag}(\mathbf{v})D_y + D_y\mathrm{diag}(\mathbf{v})\big] - \nu D_y^2 \\ &\quad - (P_x \otimes P_y)^{-1}\Big[\frac{1}{2}\mathrm{diag}(\mathbf{u}_\mathbf{n}^w)\mathbb{P}_w + \frac{1}{2}\mathrm{diag}(\mathbf{u}_\mathbf{n}^s)\mathbb{P}_s + \frac{\vartheta}{2}\mathbb{P}_n\mathrm{diag}(\mathbf{u}_\mathbf{n}^n) \\ &\quad - \nu N_y^s D_y^\mathsf{T}\mathbb{P}_s - \nu N_y^n\mathbb{P}_n D_y, \\ \widetilde{\mathcal{D}}_{13} &= D_x - (P_x \otimes P_y)^{-1}N_x^e\mathbb{P}_e, \quad \widetilde{\mathcal{D}}_{23} = D_y - (P_x \otimes P_y)^{-1}N_y^n\mathbb{P}_n, \\ \widetilde{\mathcal{D}}_{31} &= D_x - (P_x \otimes P_y)^{-1}N_x^w\mathbb{P}_w, \quad \widetilde{\mathcal{D}}_{32} = D_y - (P_x \otimes P_y)^{-1}N_y^s\mathbb{P}_s. \end{aligned}$$

The nonzero sub-matrices in $\widetilde{\boldsymbol{\mathcal{D}}}$ are now non-singular due to the addition of the boundary terms (5.28). Furthermore, the spectrum of $\widetilde{\boldsymbol{\mathcal{D}}}$ with only have positive real components is stable. By adding the temporal terms $\bar{\mathbf{I}}\mathbf{U}_t$ to (5.32), and then applying the energy methods, we obtain

$$\frac{d}{dt}||\mathbf{U}||^2_{\bar{\mathbf{I}}\mathcal{P}} = -\mathbf{U}^\mathsf{T}\big[\mathbf{P}\widetilde{\boldsymbol{\mathcal{D}}} + (\mathbf{P}\widetilde{\boldsymbol{\mathcal{D}}})^\mathsf{T}\big]\mathbf{U}. \tag{5.34}$$

The above will yield an estimate and hence prove stability if $\mathbf{P}\widetilde{\boldsymbol{\mathcal{D}}} + (\mathbf{P}\widetilde{\boldsymbol{\mathcal{D}}})^{\mathsf{T}}$ is positive semi-definite. To determine the spectrum $\widetilde{\boldsymbol{\mathcal{D}}}$, we consider the generalized nonlinear eigenvalue problem

$$\widetilde{\boldsymbol{\mathcal{D}}}(\mathbf{U})\mathbf{U} = \lambda\mathbf{U}, \tag{5.35}$$

where λ denotes the complex eigenvalues of $\widetilde{\boldsymbol{\mathcal{D}}}$ which are independent of the solution. By multiplying (5.35) with $\mathbf{U}^*\mathbf{P}$ from the left and adding it to its complex transpose, we obtain

$$\mathbf{U}^*\big[\mathbf{P}\widetilde{\boldsymbol{\mathcal{D}}} + (\mathbf{P}\widetilde{\boldsymbol{\mathcal{D}}})^{\mathsf{T}}\big]\mathbf{U} = (\lambda + \bar{\lambda})\mathbf{U}^*\mathbf{P}\mathbf{U} = 2\mathrm{Re}(\lambda)||\mathbf{U}||^2_{\mathbf{P}}, \tag{5.36}$$

where $\mathbf{U}^*$ is the complex conjugate transpose of $\mathbf{U}$. To show that $\mathrm{Re}(\lambda)$ is non-positive, it suffices to show that the LHS of (5.36) is non-negative. By reusing the previous results (see (5.8)), these terms simplify to

$$\mathbf{U}^*\big[\mathbf{P}\widetilde{\boldsymbol{\mathcal{D}}} + (\mathbf{P}\widetilde{\boldsymbol{\mathcal{D}}})^{T}\big]\mathbf{U} = 2\nu||\mathbf{D}_y\mathbf{U}||^2_{\mathbf{IP}} - \widetilde{\mathbf{BT}}, \tag{5.37}$$

where $\widetilde{\mathbf{BT}}$ is given in (5.8). For the boundary conditions (5.27a), $\widetilde{\mathbf{BT}}$ simplifies to

$$\widetilde{\mathbf{BT}} = -(1-\vartheta)\mathbf{u}^{\mathsf{T}}\mathrm{diag}(\mathbf{u}^n_{\mathbf{n}})\mathbb{P}_n\mathbf{u} - \mathbf{u}^{\mathsf{T}}\mathrm{diag}(\mathbf{u}^e_{\mathbf{n}})\mathbb{P}_e\mathbf{u} < 0. \tag{5.38}$$

Substituting (5.38) into (5.37) yields $\mathbf{U}^*\big[\mathbf{P}\widetilde{\boldsymbol{\mathcal{D}}} + (\mathbf{P}\widetilde{\boldsymbol{\mathcal{D}}})^{\mathsf{T}}\big]\mathbf{U} > 0$ which implies that $\mathrm{Re}(\lambda) > 0$ i.e. all the eigenvalues of $\widetilde{\boldsymbol{\mathcal{D}}}$ are on the right side of the complex plane for all $\mathbf{U} \neq 0$. Furthermore, their signs are independent of the order of accuracy of the SBP operators and the number of computational grid points.

Next, we inject the solution $\mathbf{U} = [1, \ldots, 1]^{\mathsf{T}}$ into (5.35) and use 4th-order SBP operators to compute the eigenvalues of $\widetilde{\boldsymbol{\mathcal{D}}}$ numerically. Further, we choose $\vartheta = 1$, this choice suffices to guarantee a positive spectrum of $\widetilde{\boldsymbol{\mathcal{D}}}$. Setting $\vartheta = 0$ will result in $\widetilde{\mathbf{BT}}$ (5.38) becoming large and negative, leading to even more positive spectrum. We consider two cases where: the developed boundary conditions are (a) not included (5.31) and (b) included (5.32). The eigenvalues resulting from the first case are depicted in Figure 5.1a. As shown, these contain both negative and zero values, which will result in an unstable solution scheme. As shown in Figure 5.1b however, the addition of the developed boundary conditions remedies the latter in full. This is a key insight and contribution of this work.

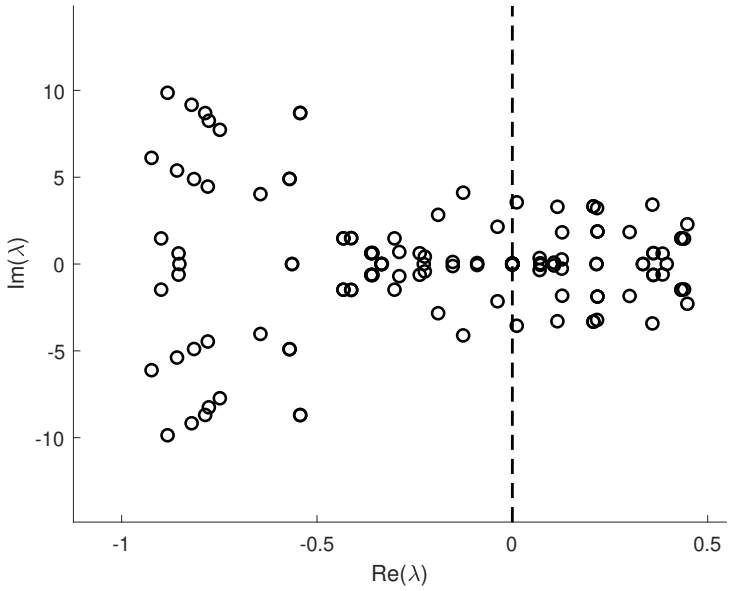

(a)

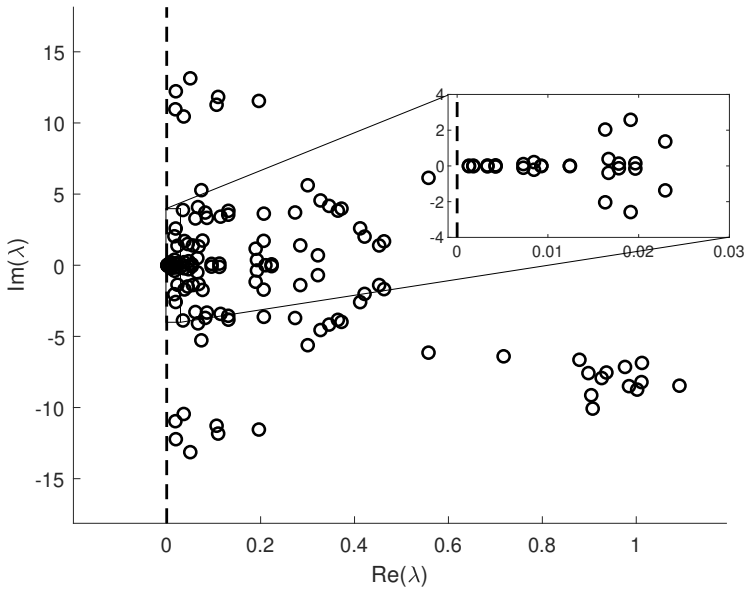

(b)

Figure 5.1: Eigenvalues of the spatial operator $\boldsymbol{\mathcal{D}}$ with (a) boundary conditions not included and (b) boundary conditions with $\vartheta = 1$ are included.

5.3 The fully discrete approximation

In the previous section, we considered the spatial discretization of (4.24) while keeping the temporal derivative continuous. We subsequently obtained the discrete energy estimates that hold for all time t. In this section, we discretize the temporal derivative in (5.3a), leading to a fully discrete formulation. Let Δt be time-step size and k denote time-level. The solution at two consecutive time-levels are denoted by U^{k+1} and U^k. By discretizing (5.3a) with the first-order

Backward Euler method [81], the fully discrete approximation of (4.24) becomes

$$\mathcal{F}(\mathbf{U}^{k+1}) = \bar{\mathbf{I}}\frac{\mathbf{U}^{k+1} - \mathrm{U}^{k}}{\Delta t} + \widetilde{\boldsymbol{\mathcal{D}}}(\mathbf{U}^{k+1})\mathbf{U}^{k+1} = 0, \tag{5.39}$$

where the spatial operator $\widetilde{\boldsymbol{\mathcal{D}}}$ includes the boundary conditions, see (5.31). Here, we choose the implicit time discretization since the vertical component of velocity and pressure have no temporal derivatives. Equation (5.39) is a system of nonlinear equations which we linearize using Newton's method [81]

$$\mathbf{U}^{k+1} = \mathbf{U}^{k} - \mathbf{J}^{-1}\mathcal{F}(\mathbf{U}^{k}), \tag{5.40}$$

where $\mathbf{J}^{-1}$ is the inverse Jacobian matrix of $\mathcal{F}$. Equation (5.40) is solved iteratively till

$$||\mathbf{U}^{k+1} - \mathbf{U}^{k}||^2_{\mathbf{P}} < tol,$$

where tol is a specified tolerance. Below, is a summary of Newton's method. We start with the initial solution $\mathbf{U}^0$ then iterate (5.40) until it converges such that $\mathcal{F}(\mathbf{U}) = 0$.

Algorithm 1 Newton's method

Require: $\mathbf{U}^0$, tol, Initial solution error l_2-norm
  while $l_2 < tol$ **do**
    $\mathbf{U}^{j+1} = \mathbf{U}^0 - \mathbf{J}^{-1}\mathcal{F}(\mathbf{U}^0)$
    if $||\mathbf{U}^{j+1} - \mathbf{U}^0||^2_{\mathbf{P}} < tol$ **then**
      Return $\mathbf{U}^{j+1}$ ▷ Converged
    else
      $j = j + 1$
      $\mathbf{U}^0 = \mathbf{U}^j$
    end if
  end while

In (5.40), $\mathbf{J} \in \mathbb{R}^{3\widetilde{N}\widetilde{M}} \times \mathbb{R}^{3\widetilde{N}\widetilde{M}}$ and it is defined as

$$\mathbf{J} = \frac{\partial \mathcal{F}}{\partial \mathbf{U}} = \begin{bmatrix} \frac{\partial \mathcal{F}_1}{\partial \mathbf{u}} & \frac{\partial \mathcal{F}_1}{\partial \mathbf{v}} & \frac{\partial \mathcal{F}_1}{\partial \mathbf{p}} \\ \frac{\partial \mathcal{F}_2}{\partial \mathbf{u}} & \frac{\partial \mathcal{F}_2}{\partial \mathbf{v}} & \frac{\partial \mathcal{F}_2}{\partial \mathbf{p}} \\ \frac{\partial \mathcal{F}_3}{\partial \mathbf{u}} & \frac{\partial \mathcal{F}_3}{\partial \mathbf{v}} & \frac{\partial \mathcal{F}_3}{\partial \mathbf{p}} \end{bmatrix},$$

where $\mathcal{F}_1$, $\mathcal{F}_2$, $\mathcal{F}_3$ are the vector elements of $\mathcal{F}$ in (5.39). Further, $\mathbf{J}$ comprises of the temporal, volume and boundary components

$$\begin{aligned} \mathbf{J} &= \mathbf{J}_{\bar{\mathbf{I}}\mathbf{U}_t} + \mathbf{J}_{\boldsymbol{\mathcal{D}}(\mathbf{U})\mathbf{U}} - \mathbf{J}_{\mathbf{P}^{-1}\boldsymbol{\Sigma}_k(I_j \otimes \mathbb{P}_k)\mathcal{H}_k\mathbf{U}} \\ &= \frac{\partial}{\partial \mathbf{U}}\left(\frac{\bar{\mathbf{I}}}{\Delta t}\mathbf{U} + \boldsymbol{\mathcal{D}}(\mathbf{U})\mathbf{U} - \mathbf{P}^{-1}\boldsymbol{\Sigma}_k(I_j \otimes \mathbb{P}_k)\mathcal{H}_k\mathbf{U}\right). \end{aligned} \tag{5.41}$$

The SBP matrices in (5.32) are independent of the solution $\mathbf{U}$ and therefore should be interpreted as constant coefficients with respect to the partial derivative operator $\frac{\partial}{\partial \mathbf{U}}(\cdot)$. We proceed by computing the Jacobian matrices in (5.41) separately. Starting with the temporal term, we have that

$$\mathbf{J}_{\bar{\mathbf{I}}\mathbf{U}_t} = \frac{1}{\Delta t}\mathrm{diag}(\mathbf{I}, \mathbf{0}, \mathbf{0}) = \frac{\bar{\mathbf{I}}}{\Delta t}, \tag{5.42}$$

where $\mathbf{I}$ is the unit matrix. We turn to the volume terms, next. Due to the nonlinear terms in $\boldsymbol{\mathcal{D}}(\mathbf{U})$, we employ the product and chain rules of differentiation [45]. Moreover, such operations should be interpreted element-wise even though we use vector notation. For example, the nonlinear terms in (5.31) are computed as

$$\frac{\partial}{\partial \mathbf{u}}\left[\mathrm{diag}(\mathbf{u})D_x\mathbf{u}\right] = \mathrm{diag}(\mathbf{u})D_x + \mathrm{diag}(D_x\mathbf{u}),$$
$$\frac{\partial}{\partial \mathbf{u}}\left[D_x\mathrm{diag}(\mathbf{u})\mathbf{u}\right] = 2\mathrm{diag}(D_x\mathbf{u}).$$

The Jabocian matrix of the volume spatial operator is

$$\mathbf{J}_{\boldsymbol{\mathcal{D}}(\mathbf{U})\mathbf{U}} = \begin{bmatrix} \frac{1}{2}\big[\mathrm{diag}(\mathbf{u})D_x + \mathrm{diag}(D_x\mathbf{u}) + 2\mathrm{diag}(D_x\mathbf{u}) & 2\mathrm{diag}(D_y\mathbf{u}) & D_x \\ \quad + D_y\mathrm{diag}(\mathbf{v}) + \mathrm{diag}(\mathbf{v})D_y - \nu D_y^2\big] & & \\ \mathbf{0} & \mathbf{0} & D_y \\ D_x & D_y & \mathbf{0} \end{bmatrix}. \tag{5.43}$$

Next, we treat the penalty terms and similar to the volume terms, some of these terms are nonlinear in $\mathbf{u}$. Using (5.28), $\mathbf{J}$ for each boundary reads

$$\mathbf{J}_{\mathbf{P}^{-1}\boldsymbol{\Sigma}_s(I_j\otimes\mathbb{P}_s)\mathcal{H}_s\mathbf{U}} = \mathbf{P}^{-1}\begin{bmatrix} \frac{1}{2}\mathrm{diag}(\mathbf{u}_\mathbf{n}^s) - \nu N_y^s D_y^\mathsf{T} & \frac{1}{2}N_y^s\mathrm{diag}(\mathbf{u}) & \mathbf{0} \\ \mathbf{0} & \mathbf{0} & \mathbf{0} \\ \mathbf{0} & N_y^s & \mathbf{0} \end{bmatrix}(I_3\otimes\mathbb{P}_s), \tag{5.44a}$$

$$\mathbf{J}_{\mathbf{P}^{-1}\boldsymbol{\Sigma}_n(I_j\otimes\mathbb{P}_n)\mathcal{H}_n\mathbf{U}} = \mathbf{P}^{-1}(I_3\otimes\mathbb{P}_n)\begin{bmatrix} \frac{\vartheta}{2}\mathrm{diag}(\mathbf{u}_\mathbf{n}^n) - \varepsilon N_y^n D_y & \frac{\vartheta}{2}N_y^n\mathrm{diag}(\mathbf{u}) & \mathbf{0} \\ \mathbf{0} & \mathbf{0} & N_y^n \\ \mathbf{0} & \mathbf{0} & \mathbf{0} \end{bmatrix}, \tag{5.44b}$$

$$\mathbf{J}_{\mathbf{P}^{-1}\boldsymbol{\Sigma}_e(I_j\otimes\mathbb{P}_e)\mathcal{H}_e\mathbf{U}} = \mathbf{P}^{-1}(I_3\otimes\mathbb{P}_e)\begin{bmatrix} \mathbf{0} & \mathbf{0} & N_x^e \\ \mathbf{0} & \mathbf{0} & \mathbf{0} \\ \mathbf{0} & \mathbf{0} & \mathbf{0} \end{bmatrix}, \tag{5.44c}$$

$$\mathbf{J}_{\mathbf{P}^{-1}\boldsymbol{\Sigma}_w(I_j\otimes\mathbb{P}_w)\mathcal{H}_w\mathbf{U}} = \mathbf{P}^{-1}(I_3\otimes\mathbb{P}_w)\begin{bmatrix} \mathrm{diag}(\mathbf{u}_\mathbf{n}^w) & \mathbf{0} & \mathbf{0} \\ \mathbf{0} & \mathbf{0} & \mathbf{0} \\ N_x^w & \mathbf{0} & \mathbf{0} \end{bmatrix}. \tag{5.44d}$$

5.4 Closing remarks

We derived the stable approximation (5.3) of the boundary layer equations (4.1) using the SBP-SAT framework. By discretely imitating the continuous analysis in Chapter 4, we derived the discrete estimates that mimic the continuous counterparts. Subsequently, we considered the flat-plate problem with the discrete version of the newly derived energy-stable boundary conditions (4.35) and proved stability. Further, we demonstrated that the augmentation of the spatial operator with these boundary conditions alleviates the saddle-node problem typically associated with the incompressible flow equations. By discretizing the temporal term implicitly using the first-order Backward Euler, we formulated the fully discrete problem and subsequently presented the Newton's iterative method for solving the resulting system of nonlinear equations. In Chapter 6, we will verify (5.3) for high-order accuracy using numerical experiments and finally, we consider the solution for the flat-plate boundary layer problem.

Chapter 6

Numerical experiments and convergence rates

In this chapter, we verify the high-order accuracy of the approximation (5.3). For this purpose, we employ the method of manufactured solution (MMS) [82]. Once we have verified the accuracy, we proceed to computing the SBP-SAT approximation for the flat-plate boundary layer problem described in Section 3.2. We further compare the computational results with the Blasius similarity solution described in Appendix B.

6.1 Order of accuracy

We compute the rate at which the approximation (5.3) convergences to an analytical solution using MMS. In this code-verification procedure, a differentiable analytical solution is proposed and substituted into the PDE to derive a forcing function, which is then projected on the grid points and added to the RHS of a numerical scheme. We discretize the spatial derivatives using $(2s, s)$-accurate SBP finite difference operators on SBP form as described in Section 2.5. Furthermore, we approximate the viscous term in (5.3) by applying first derivative SBP operator twice (see (2.23)) which leads to $s+1$ global order of accuracy since the approximation is stable.

We advance the computations in time implicitly using the Backward Euler method (5.39). Further, we set time-step $\triangle t = 1\mathrm{e}-04$ such that the temporal errors are small and the scheme is terminated at $t = 1$. The resulting nonlinear system is solved using Newton's method (5.40), and we set the error tolerance between the successive Newton's iterations to $tol = 1\mathrm{e}-08$. Lastly, we choose the manufactured solution

$$\begin{aligned} &u(x,y,t) = \cosh(x)\sinh(y)e^{\nu t}, \quad v(x,y,t) = -\sinh(x)\cosh(y)e^{\nu t}, \\ &p(x,y,t) = \frac{1}{2}\sinh^2(x)e^{2\nu t}, \end{aligned} \tag{6.1}$$

on domain $\Omega = [0,1]^2$. Here, $\nu = 0.01$, and (6.1) satisfies (4.1a) exactly, leading to a forcing function that is zero (see Appendix C). The initial and boundary data are obtained by substituting (6.1) into (4.35). At the north boundary, we impose the Robin boundary condition i.e. we set $\vartheta = 1$ such that the energy rate (5.30) is bounded only by the east boundary term. Further, it possesses the correct sign since $u(1,y,t) \geq 0$ in (6.1). The convergence rates which are

computed using (2.29) for different orders of accuracy are presented in Tables 6.1 – 6.4, and they are compared with the theoretical order of convergence [64].

	u-velocity					
$N = M$	SBP(2,1)		SBP(4,2)		SBP(6,3)	
	L_2	q	L_2	q	L_2	q
21	0.0318	-	0.0030	-	5.9106e-04	-
41	0.0079	2.0829	3.1441e-04	3.3769	3.3657e-05	4.2834
61	0.0032	2.2951	7.3585e-05	3.6553	4.5945e-06	5.0120
81	0.0016	2.4443	2.4828e-05	3.8313	1.0355e-06	5.2543
Theoretical order		2		3		4

Table 6.1: The L_2 norm of errors and the global order of accuracy of the approximation (5.3) for the u-velocity using different SBP operators.

	v-velocity					
$N = M$	SBP(2,1)		SBP(4,2)		SBP(6,3)	
	L_2	q	L_2	q	L_2	q
21	0.0907	-	0.0098	-	0.0028	-
41	0.0210	2.1870	0.0015	2.7727	2.0366e-04	3.9257
61	0.0092	2.0861	4.3612e-04	3.1544	3.0721e-05	4.7609
81	0.0050	2.1503	1.6813e-04	3.3613	7.6274e-06	4.9130
Theoretical order		2		3		4

Table 6.2: The L_2 norm of errors and the global order of accuracy of the approximation (5.3) for the v-velocity using different SBP operators.

Pressure						
$N = M$	SBP(2,1)		SBP(4,2)		SBP(6,3)	
	L_2	q	L_2	q	L_2	q
21	0.0159	-	0.0021	-	5.2357e-04	-
41	0.0038	2.1549	1.9608e-04	3.5691	1.6050e-04	5.2088
61	0.0016	2.1989	4.7083e-05	3.6000	2.1108e-06	5.1061
81	8.4464e-04	2.2528	1.6355e-05	3.7287	6.9588e-07	3.9131
Theoretical order		2		3		4

Table 6.3: The L_2 norm of errors and the global order of accuracy of the approximation (5.3) for the pressure using different SBP operators.

Solution vector U						
$N = M$	SBP(2,1)		SBP(4,2)		SBP(6,3)	
	L_2	q	L_2	q	L_2	q
21	0.0029	-	0.0104	-	0.0029	-
41	0.0227	2.1743	0.0016	2.8300	2.0705e-04	3.9576
61	0.0098	2.1125	4.4478e-04	3.1770	3.1134e-05	4.7688
81	0.0053	2.1676	1.7074e-04	3.3763	7.7287e-06	4.9135
Theoretical order		2		3		4

Table 6.4: The L_2 norm of errors and the global order of accuracy of the approximation (5.3) for all variables $\mathrm{U} = [u, v, p]^T$ using different SBP operators.

The computed convergence rates above are slightly larger than the theoretical ones. This is possibly due to the time step-size $\Delta t = 1e-04$, which we chose to limit the simulation times. A smaller time-step size could possibly lead to a sharper match with the theoretical convergence rates.

6.2 Blasius boundary layer

Next, we model viscous flow over a flat-plate as illustrated in Figure 3.1. When encountering the plate's leading edge, the fluid near the solid wall slows down due to the no slip condition. Outside the boundary region, the fluid's speed increases rapidly in the vertical direction until it reach the stream velocity leading to the formation of the boundary layer. As a result, the velocity gradients are the steepest near the leading edge and the plate's surface. The thickness of this boundary layer $\delta(x)$ grows as a function of distance from the leading edge. To resolve it effectively, we employ nonuniform stretched meshes in the vicinity of the solid surface. As alluded to in Section

2.8, the use of the SBP finite difference operators on nonuniform computational grids requires a consistent coordinate transformation that preserves the overall accuracy of the approximation scheme. We therefore consider the encapsulated SBP operators in (2.49).

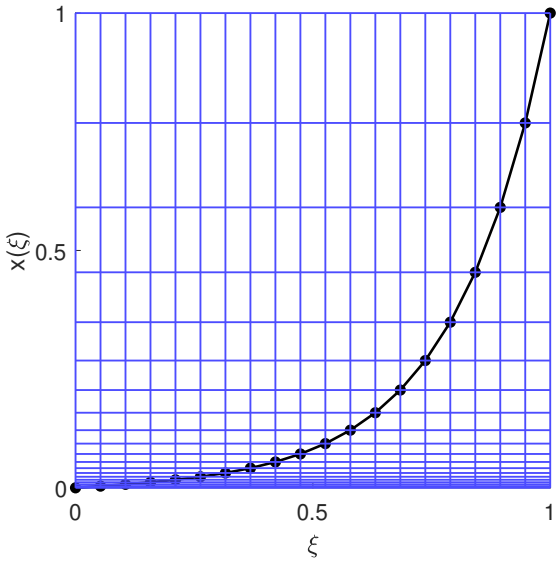

Figure 6.1: Trigonometric hyperbolic function sinh(·) used to generate a stretched computational mesh such that the grids are saturated near the origin and the plate's surface.

For coordinate stretching, we choose the continuous trigonometric hyperbolic function sinh(·). This choice is inspired by a slow growth near the origin as shown in Figure 6.1, which allows the mesh to be saturated in the region where the velocity gradients are the steepest. The curvilinear mesh is generated by

$$x(\xi,\eta) = x_0 + x_1\frac{\sinh(\beta\xi)}{\sinh(\beta)}, \quad y(\xi,\eta) = y_0 + y_1\frac{\sinh(\beta\eta)}{\sinh(\beta)}, \tag{6.2}$$

where $(\xi,\eta) \in [0,1]^2$ are the coordinates of the transformed regular domain, β is the stretching factor and we set it to $\beta = 4$. Further, x_0, y_0 and x_1, y_1 denote the minimum and maximum of the values of the physical rectangular domain such that the pairs (x_0, y_0) and (x_0, y_1) are the coordinates of the left lower and upper corners. Meanwhile, the coordinates of the right lower and upper corners are given by (x_1, y_0) and (x_1, y_1), respectively. Figures 6.2*a* and 6.2*b* show the 2D isometric and stretched nonuniform computational meshes.

We consider the steady version of (4.1) on the domain $\Omega \in [0,10] \times [0,4]$ and the stable approximation (5.3). We discretize Ω using $N = M = 80$ points and set boundary data $U_\infty = 1$, $p_\infty = 0$. At the north boundary, we consider Neumann boundary condition (i.e. set $\vartheta = 0$ in (4.35)) since we only know the velocity gradient of u in the freestream i.e. $\nu u_y = 0$. This choice however does not affect the positive definiteness of the resulting coefficient matrix as shown in (5.32).

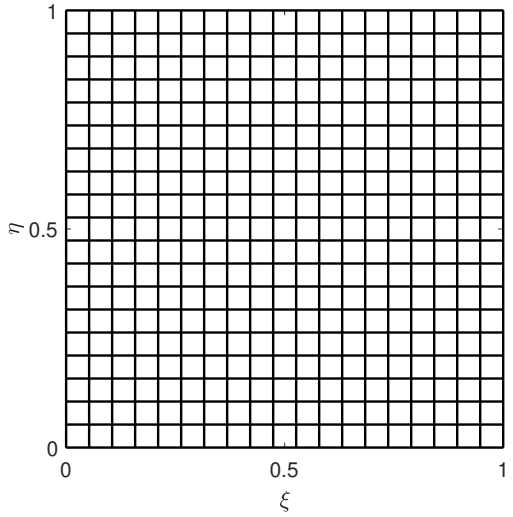

(a) Isometric mesh

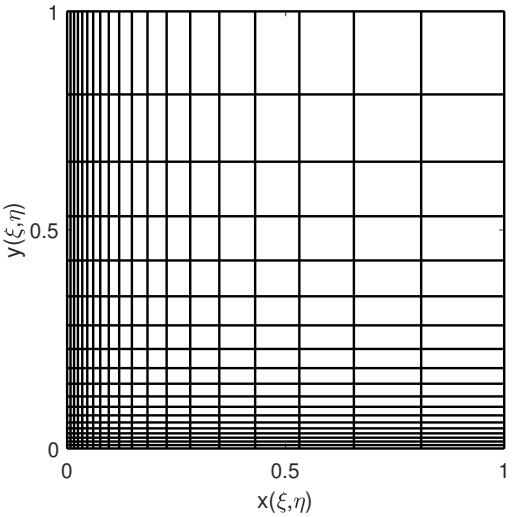

(b) Stretched nonuniform mesh

Figure 6.2: Two-dimensional computational mesh for the flat-plate boundary layer problem generated with the trigonometric hyperbolic functions.

The continuous derivatives are approximated using 3rd-order accurate SBP operators. Starting with the initial guess $\mathbf{U}^1 = [\mathbf{u}^1, \mathbf{v}^1, \mathbf{p}^1]^T = [1, \ldots, 1, 0, \ldots, 0, 0 \ldots, 0]^T$, we iterate (5.39) progressively until we reach the steady state solution which is measured by

$$||Res_k||^2_{\mathbf{P}} \leq 10^{-8}||Res_1||^2_{\mathbf{P}}$$

where Res_k is the residual (comprising of the spatial terms) at the kth time-level. There are no restrictions on the time-step size and we set it to $\Delta t = 0.01$. Moreover, we set $\nu = 0.01$ such that $\delta \ll l$. Figure 6.3 shows the velocity distribution on the entire computational domain, with a fully developed boundary layer.

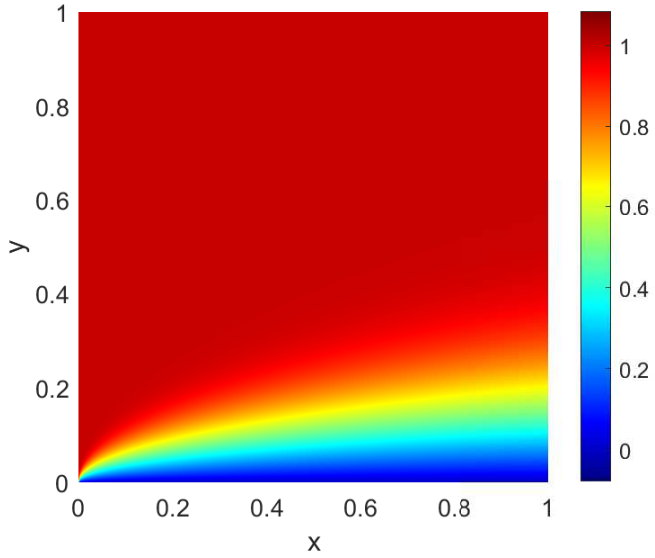

Figure 6.3: Horizontal velocity distribution of the Blasius boundary layer on the entire plate with $\nu = 0.01$.

Equation (3.8) with (i) $p_x = 0$, (ii) boundary conditions (4.35) with $\vartheta = 0$, and (iii) U_∞ = constant has a well-known time-independent solution called the Blasius solution. The similarity solution approach reduces (3.8) to a system of nonlinear ordinary differential equations which is then solved numerically (for details, see Appendix B). Therefore, we will use this case to validate the SBP-SAT approximation (5.3). We iterate (5.39) till we reach the steady solution and then compare the results with the Blasius solution along particular vertical cross-sections on the domain. In Figure 6.4*a* and 6.4*b*, the velocity profiles along $x \approx 5$ are shown and they compare very well with the Blasius solution.

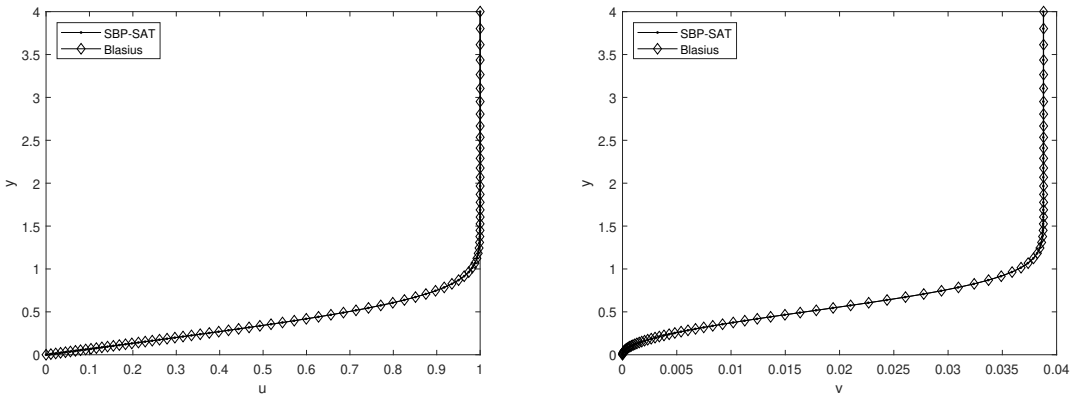

(a) (b)

Figure 6.4: The SBP-SAT approximation for the IBL equations compared with Blasius solution along the line $x \approx 5$ with computations starting at the plate's leading edge. (a) u-velocity profile and (b) v-velocity profile.

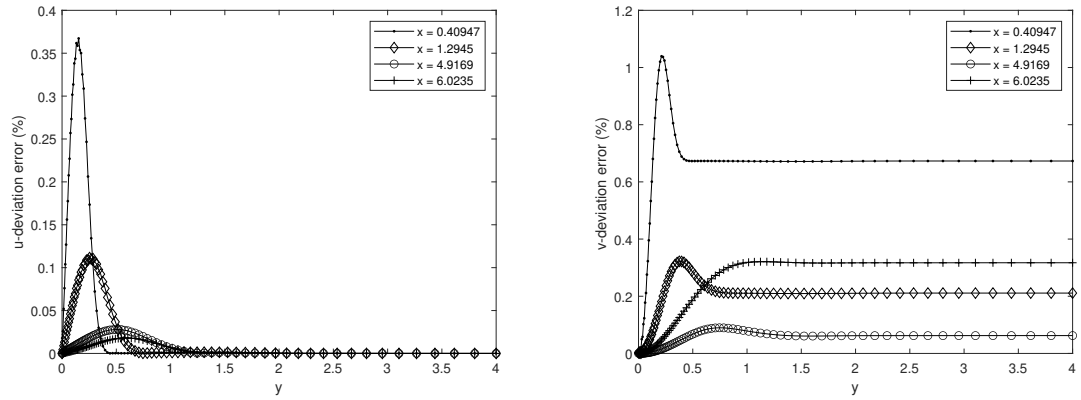

(a) (b)

Figure 6.5: The deviation errors of the (a) u-velocity and (b) v-velocity at various x position along the plate with computations starting at the leading edge.

Next, we include more vertical cross-sections across the domain and compare the deviation errors between the two solution as shown in Figure 6.5*a* and 6.5*a*. The point-wise errors are computed as

$$\text{error}|_u = \frac{|u - u_{\text{B}}|}{|\max(u_{\text{B}})|} \times 100\%, \tag{6.3}$$

where u and u_{B} denote the SBP-SAT approximation and the Blasius solution. Similarly, we use (6.3) to compute the deviations for the v-velocity. As shown in both profiles, the errors are more dominant towards the plate's leading edge and they dissipate downstream. This is however thought to be due to the singularity at the leading edge of the plate i.e. gradients in u tend to infinity here [83].

6.2.1 Truncated domain

To address the drawback pointed out in the previous section, we truncate domain Ω in Figure 3.1 such that it excludes the tip of the plate and start the computations at a point x_0 on the domain as illustrated in Figure 6.6*a*. Instead of using U_∞ as inflow data, we use the Blasius solution evaluated at x_0 such that the gradients with respect to x are not large. In this regard, we choose $x_0 = 2$ as shown in Figure 6.6*b*.

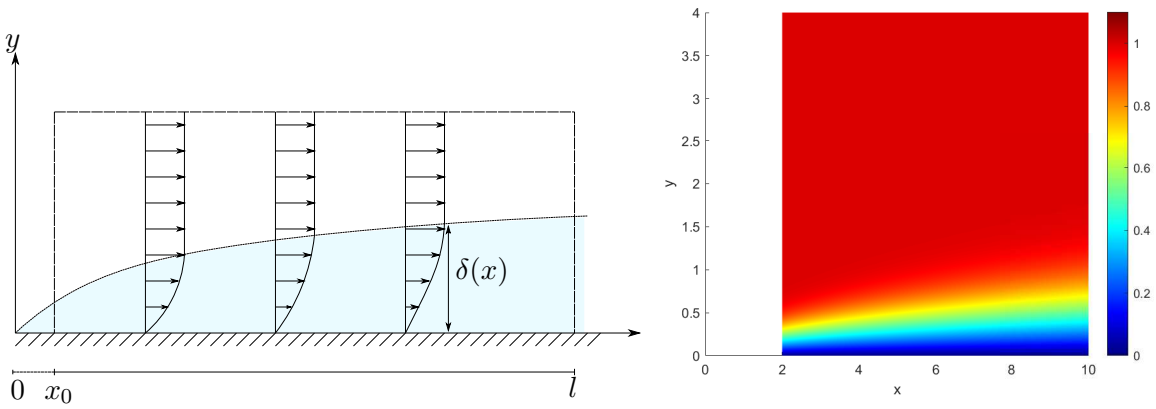

(a) (b)

Figure 6.6: The illustration of the (a) truncated domain that excludes the leading edge and (b) the u-velocity distribution.

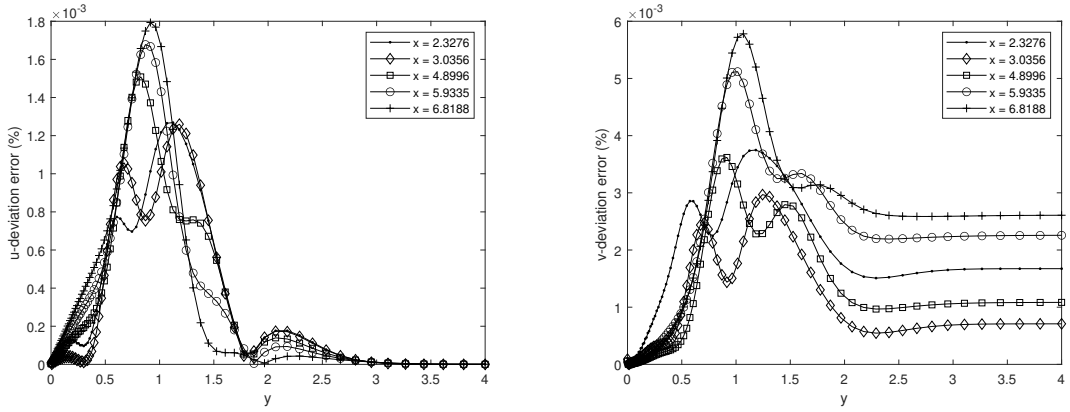

(a) (b)

Figure 6.7: The deviation errors of the (a) u-velocity and (b) v-velocity at various x position along the plate on the truncated domain.

Similar to the full domain case, we compare the deviation errors between the two solutions at various $x-$positions on the truncated domain. A notable observation in Figure 6.7 is the decrease in the magnitude of the errors. Further, though small, the errors in v do not drop to zero with increasing y but asymptote to a value. This was also the case for the full domain in Figure 6.5b. The reason for this will be investigated as part of future work.

Next, we compute the wall shear τ_w along the plate and compare to that computed from the Blasius similarity solution in Appendix B. Note that at the tip of the plate, the velocity gradients are infinite and moreover, the Blasius solution does not exist at $x = 0$. Therefore, we will next consider the truncated domain. The wall shear is computed as

$$\tau_w = \nu D_y \mathbf{u}|_{y=0}$$

and an accurate solution is achieved as shown in Figure 6.8.

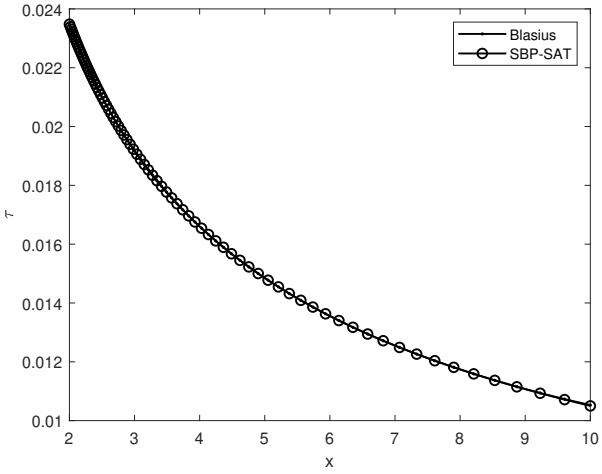

Figure 6.8: The wall shear along the plate computed from the SBP-SAT approximation is compared with the Blasius wall shear.

6.3 Closing remarks

In this chapter, we verified the high-order accuracy of the newly developed provably stable SBP-SAT approximation for the IBL equations (5.3). We proceeded to compute the solution of the Blasius boundary layer problem (3.10) and it corroborates with the analytical solution. By further computing the deviation errors at various x-positions on the plate, we observed the inconsistency between the computed and the analytical solutions near the plate's leading edge. We speculated that the discontinuity at the leading edge could be the cause of this. This prompted us to consider the truncated domain where we injected the analytical solution at the inflow boundary. The solution deviation errors on the new domain were significantly less. Lastly, we computed the wall shear on the plate and compared it with the Blasius shear. In the next chapter, we will consider the SBP-SAT approximation for the fully INS equations (3.4) and compare it with the Blasius solution.

Chapter 7

The fully incompressible Navier-Stokes equations

In Chapter 3, we derived the IBL equations from the INS equations at Re $\gg 1$ using dimensional analysis. We further formulated the continuous problem and the corresponding discrete problem in Chapter 4 and 5, respectively. Subsequently in Chapter 6, we considered the flat-plate boundary layer problem and compared the computed solution with the analytical one. In this chapter, we endeavor to corroborate the assumptions we made in Chapter 3 by comparing the SBP-SAT approximation of the INS equations with the Blasius similarity solution for different Reynolds numbers. We commence this investigation by presenting the continuous and discrete formulations of the INS equations. The detailed energy and stability analysis were considered in [32], and we will therefore omit the details herein. The developed numerical scheme was further verified for high-order accuracy in [84]. In this chapter, we adopt this scheme and compute the solution of the flat-plate boundary layer problem (depicted in Figure 7.1) modeled with the INS equations.

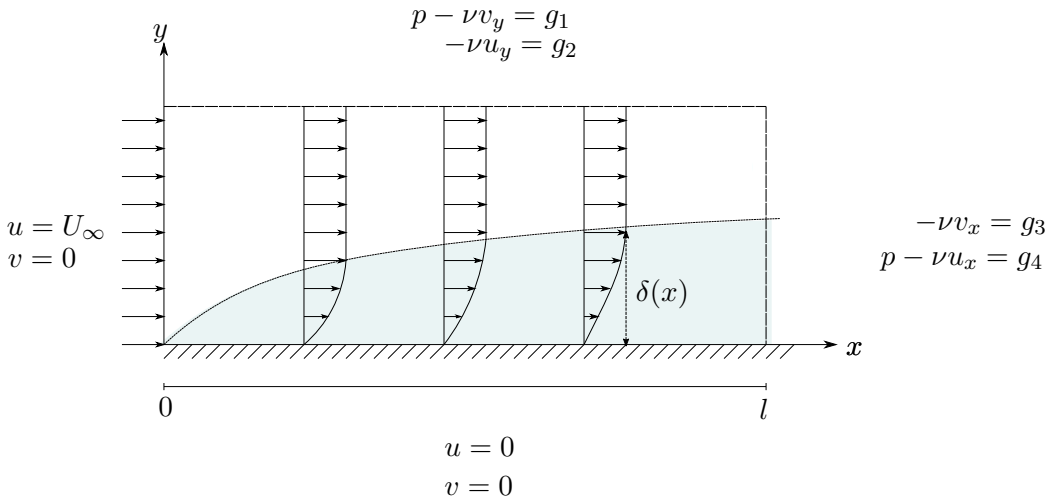

Figure 7.1: The depiction of the viscous flow over a thin plate of length l modeled with the fully INS equations.

7.1 Boundedness

Consider domain $\Omega \in [0,1]^2$ with boundary Γ. Similar to the continuous analysis of IBL equations in Chapter 4, the skew-symmetric form of (3.4) in matrix-vector form, augmented with initial and boundary conditions is

$$\begin{aligned} \widetilde{I}V_t + \frac{1}{2}\left[(\widetilde{A}V)_x + \widetilde{A}V_x + (\widetilde{B}V)_y + \widetilde{B}V_y\right] &= \nu\widetilde{I}\Delta V, \quad (x,y) \in \Omega, \quad t > 0, \\ LV &= \widehat{\mathbf{g}}, \quad (x,y) \in \Gamma, \quad t > 0, \\ \widetilde{I}V &= \widehat{\mathbf{f}}, \quad (x,y) \in \Omega, \quad t = 0. \end{aligned} \tag{7.1}$$

Here, $V = [u, v, p]^{\mathsf{T}}$ is the solution vector and the variables u, v, p, and ν are defined as before in Section 4.1. Further, $\triangle = \partial_x^2 + \partial_y^2$ is the Laplace operator while the coefficient matrices $\widetilde{I}$, $\widetilde{A}$, $\widetilde{B}$ are

$$\widetilde{A} = \begin{bmatrix} u & 0 & 1 \\ 0 & u & 0 \\ 1 & 0 & 0 \end{bmatrix}, \quad \widetilde{B} = \begin{bmatrix} v & 0 & 0 \\ 0 & v & 1 \\ 0 & 1 & 0 \end{bmatrix}, \quad \widetilde{I} = \begin{bmatrix} 1 & 0 & 0 \\ 0 & 1 & 0 \\ 0 & 0 & 0 \end{bmatrix}.$$

In (7.1), L is the boundary operator, the continuous and compatible functions $\widehat{\mathbf{g}}$, $\widehat{\mathbf{f}}$ denote the boundary and initial data, respectively. Contrary to the IBL equations where we only imposed initial condition on the u-velocity, we also impose an initial condition on v-velocity. Therefore, $\widehat{\mathbf{f}}$ has the form $\widehat{\mathbf{f}} = (\widehat{f}_1, \widehat{f}_2, 0)^{\mathsf{T}}$.

The energy method applied to (7.1) yields

$$\frac{d}{dt}||V||_{\widetilde{I}}^2 + 2\nu||\nabla V||_{\widetilde{I}}^2 = \widehat{\mathrm{BT}}, \tag{7.2}$$

where $\widehat{\mathrm{BT}}$ denotes the indefinite boundary terms

$$\widehat{\mathrm{BT}} = -\oint_{\Gamma} \left[u_{\mathbf{n}}(u^2 + v^2) + 2u_{\mathbf{n}}p - 2\nu(uu_x n_x + uu_y n_y + vv_x n_x + vv_y n_y)\right] ds.$$

Similar to the energy rate of the IBL equations in (4.6), (7.2) is decreasing and hence leads to an energy estimate if $\widehat{\mathrm{BT}} \leq 0$. We demonstrated earlier by following the *roadmap* in Figure 4.1 how this can be achieved by imposing appropriate boundary conditions. To obtain boundedness in (7.2), exactly two boundary conditions must be imposed at each boundary [32]. This is due to the presence of the second derivatives in both the x- and y-directions. We recall that the IBL problem (4.1) has only u_{yy}, and hence, exactly one boundary condition at the vertical boundaries was required (see (4.35)). To model the flat-plate boundary layer problem with the INS equation, we impose no-slip velocity conditions on the plate's surface and the inflow boundary conditions at the west boundary. At the north and east boundaries, we impose outflow boundary conditions as depicted in Figure 7.1. Further, these boundary conditions can be written in matrix-vector

notation $LV = \widehat{\mathbf{g}}$ as

$$L_w = \begin{bmatrix} 1 & 0 & 0 \\ 0 & 1 & 0 \\ 0 & 0 & 0 \end{bmatrix} \begin{bmatrix} u \\ v \\ p \end{bmatrix} = \begin{bmatrix} U_\infty \\ V_\infty \\ 0 \end{bmatrix}, \quad L_e = \begin{bmatrix} 0 & -\nu\partial_x & 0 \\ -\nu\partial_x & 0 & 1 \\ 0 & 0 & 0 \end{bmatrix} \begin{bmatrix} u \\ v \\ p \end{bmatrix} = \begin{bmatrix} 0 \\ P_\infty \\ 0 \end{bmatrix}, \tag{7.3}$$

$$L_s = \begin{bmatrix} 1 & 0 & 0 \\ 0 & 1 & 0 \\ 0 & 0 & 0 \end{bmatrix} \begin{bmatrix} u \\ v \\ p \end{bmatrix} = \begin{bmatrix} 0 \\ 0 \\ 0 \end{bmatrix}, \quad L_n = \begin{bmatrix} -\nu\partial_y & 0 & 1 \\ 0 & -\nu\partial_y & 0 \\ 0 & 0 & 0 \end{bmatrix} \begin{bmatrix} u \\ v \\ p \end{bmatrix} = \begin{bmatrix} P_\infty \\ 0 \\ 0 \end{bmatrix},$$

where U_∞, V_∞ are the freestream velocities, while P_∞ is the freestream pressure. Furthermore, since freestream is parallel to the plate, we have that $V_\infty = 0$.

Next, we obtain the energy bound in (7.2) by substituting the homogeneous form of (7.3) into (7.2). The energy rate simplifies to

$$\frac{d}{dt}||V||^2_{\widetilde{I}} + 2\nu||\nabla V||^2_{\widetilde{I}} = -\int_{\Gamma_n} u_{\mathbf{n}}(u^2+v^2)dx - \int_{\Gamma_e} u_{\mathbf{n}}(u^2+v^2)dy, \tag{7.4}$$

which is non-positive since the north and east boundaries are the outflow boundaries (i.e. $u_{\mathbf{n}} > 0$). Further, we note the similarity between (4.53) and (7.4) but with an additional $-\oint_\Gamma u_{\mathbf{n}} v^2 ds$ term. Finally, the temporal integration over a finite time domain leads to an estimate.

7.2 Stability

Next, we present the semi-discrete SBP-SAT approximation of (7.1). We begin by discretizing Ω with $N \times M$ equispaced Cartesian grid as shown in Figure 2.1. The semi-discrete formulation of (7.1) with the weakly imposed boundary conditions is

$$\begin{aligned} \widetilde{\boldsymbol{I}}\mathbf{V}_t + \widehat{\boldsymbol{\mathcal{D}}}(\mathbf{V})\mathbf{V} &= \sum_{k\in\{n,s,e,w\}} \mathbf{P}^{-1}\boldsymbol{\Sigma}_k(I_2 \otimes \mathbb{P}_k)\left(\mathbf{L}_k\mathbf{V} - \widehat{G}_k\right), \\ \widetilde{\boldsymbol{I}}\mathbf{V} &= \widehat{F}_k, \end{aligned} \tag{7.5}$$

where

$$\widehat{\boldsymbol{\mathcal{D}}} = \frac{1}{2}\left[\widetilde{\mathbf{A}}\mathbf{D}_x + \mathbf{D}_x\widetilde{\mathbf{A}} + \widetilde{\mathbf{B}}\mathbf{D}_y + \mathbf{D}_y\widetilde{\mathbf{B}}\right] - \nu\widetilde{\boldsymbol{I}}\left(\mathbf{D}_x^2 + \mathbf{D}_y^2\right),$$

is the differential operator. Here, $\widetilde{\boldsymbol{I}}$, $\widetilde{\mathbf{A}}$, $\widetilde{\mathbf{B}}$ are the discrete versions of $\widetilde{I}$, $\widetilde{A}$, $\widetilde{B}$ in (7.1) while $\mathbf{V}$ is the approximate solution. The terms on the RHS of (7.5) are the weakly imposed boundary conditions. As before, $\boldsymbol{\Sigma}_k$ denotes the penalty coefficients for the kth boundary which must be determined such that (7.5) is stable. The discrete boundary operator and data are respectively denoted by $\mathbf{L}_k$ and $\widehat{G}_k$ while $\widehat{F}_k$ contains initial data evaluated at the grid points. Lastly, it is shown in [21, 77] that a stable imposition of the boundary conditions (7.3) remove the singularities of the nullspace of the operator $\widehat{\boldsymbol{\mathcal{D}}}$ in (7.5).

The discrete energy method applied to (7.5) yields

$$\frac{d}{dt}||\mathbf{V}||^2_{\widetilde{\boldsymbol{I}}} + 2\nu\left(||\mathbf{D}_x\mathbf{V}||^2_{\widetilde{\boldsymbol{I}}} + ||\mathbf{D}_y\mathbf{V}||^2_{\widetilde{\boldsymbol{I}}}\right) = \widehat{\mathbf{BT}}, \tag{7.6}$$

where $\widehat{\mathbf{BT}}$ discretely imitates $\widehat{\mathrm{BT}}$ in (7.2) with additional penalty terms. Further, it reads

$$\begin{aligned}\widehat{\mathbf{BT}} = -\sum_{k\in\{n,s,e,w\}} \Big[&\mathbf{u}^{\mathsf{T}}\mathbb{P}_k \mathrm{diag}(\mathbf{u_n})\mathbf{u} + \mathbf{v}^{\mathsf{T}}\mathbb{P}_k \mathrm{diag}(\mathbf{u_n})\mathbf{v} + 2\mathbf{u_n}^{\mathsf{T}}\mathbb{P}_k\mathbf{p} \\ &- 2\nu(\mathbf{u}^{\mathsf{T}}\mathbb{P}_k(N_x^k\mathbf{D}_x + N_y^k\mathbf{D}_y)\mathbf{u} + \mathbf{v}^{\mathsf{T}}\mathbb{P}_k(N_x^k\mathbf{D}_x + N_y^k\mathbf{D}_y)\mathbf{v}) \\ &+ \mathbf{V}^{\mathsf{T}}\mathbf{\Sigma}_k(I_2\otimes\mathbb{P}_k)(\mathbf{L}_k\mathbf{V} - \widehat{G}_k) + (\mathbf{V}^{\mathsf{T}}\mathbf{\Sigma}_k(I_2\otimes\mathbb{P}_k)(\mathbf{L}_k\mathbf{V} - \widehat{G}_k))^{\mathsf{T}}\Big].\end{aligned}$$

The boundary term above is indefinite since it comprises of the cubic velocity term and the gradients. Therefore, to obtain stability, we must deduce $\mathbf{\Sigma}_k$ such that the penalty terms cancel the indefinite boundary terms in (7.6). Let's consider the following penalty coefficients matrices [31, 84]

$$\mathbf{\Sigma}_w = \begin{bmatrix} \frac{1}{2}\mathrm{diag}(\mathbf{u_n}^w) - \nu D_x^{\mathsf{T}} N_x^w & \mathbf{0} & \mathbf{0} \\ \mathbf{0} & \frac{1}{2}\mathrm{diag}(\mathbf{u_n}^w) - \nu D_x^{\mathsf{T}} N_x^w & \mathbf{0} \\ \mathbf{0} & \mathbf{0} & N_x^w \end{bmatrix}, \quad \mathbf{\Sigma}_e = I_3 \otimes N_x^e, \tag{7.7}$$

$$\mathbf{\Sigma}_s = \begin{bmatrix} \frac{1}{2}\mathrm{diag}(\mathbf{u_n}^s) - \nu D_y^{\mathsf{T}} N_y^s & \mathbf{0} & \mathbf{0} \\ \mathbf{0} & \frac{1}{2}\mathrm{diag}(\mathbf{u_n}^s) - \nu D_y^{\mathsf{T}} N_y^s & \mathbf{0} \\ \mathbf{0} & \mathbf{0} & N_y^s \end{bmatrix}, \quad \mathbf{\Sigma}_n = I_3 \otimes N_y^n.$$

Therefore, by substituting the discrete version of the boundary conditions (7.3) with zero data and (7.7) into (7.6), the energy rate simplifies to

$$\begin{aligned}\frac{d}{dt}||\mathbf{V}||_{\tilde{\boldsymbol{I}}}^2 + 2\nu\left(||\mathbf{D}_x\mathbf{V}||_{\tilde{\boldsymbol{I}}}^2 + ||\mathbf{D}_y\mathbf{V}||_{\tilde{\boldsymbol{I}}}^2\right) = &-\left(\mathbf{u}^{\mathsf{T}}\mathbb{P}_n \mathrm{diag}(\mathbf{u_n}^n)\mathbf{u} + \mathbf{v}^{\mathsf{T}}\mathbb{P}_n \mathrm{diag}(\mathbf{u_n}^n)\mathbf{v}\right), \\ &-\left(\mathbf{u}^{\mathsf{T}}\mathbb{P}_e \mathrm{diag}(\mathbf{u_n}^e)\mathbf{u} + \mathbf{v}^{\mathsf{T}}\mathbb{P}_e \mathrm{diag}(\mathbf{u_n}^e)\mathbf{v}\right),\end{aligned} \tag{7.8}$$

which is discretely identical to (7.4). Moreover, stability is obtained by integrating (7.8) in time over a finite domain.

7.3 Validation

Next, we consider the lid-driven cavity problem [85] as a validation test case for the approximation (7.5) before tackling the boundary layer problem. Similar to the approximation of the IBL equations (5.39), we discretize the temporal term in (7.5) implicitly using Backward Euler method and solve the resulting system using Newton's method. The lid-driven cavity problem modeled with the INS equations has a steady state (experiments-based) solution [85]. The flow geometry for this benchmark problem is illustrated in Figure 7.2. We impose no-slip velocity conditions at the east, west, and south boundaries. At the north boundary, we allow the upper surface (lid) to move horizontally to the right by setting $u = 1$ and $v = 0$. This problem is another classic example of the conflicting boundary conditions. There is discontinuity in u at the top corners where the inflow and wall conditions coincide. It can be shown however that the strong imposition of the homogeneous form of these boundary conditions eliminate the indefinite boundary terms in (7.2) [84], leading to an energy estimate. As mentioned in Chapter 4, we

avoid this conflict when implementing the numerical scheme by imposing boundary conditions weakly using the SAT method.

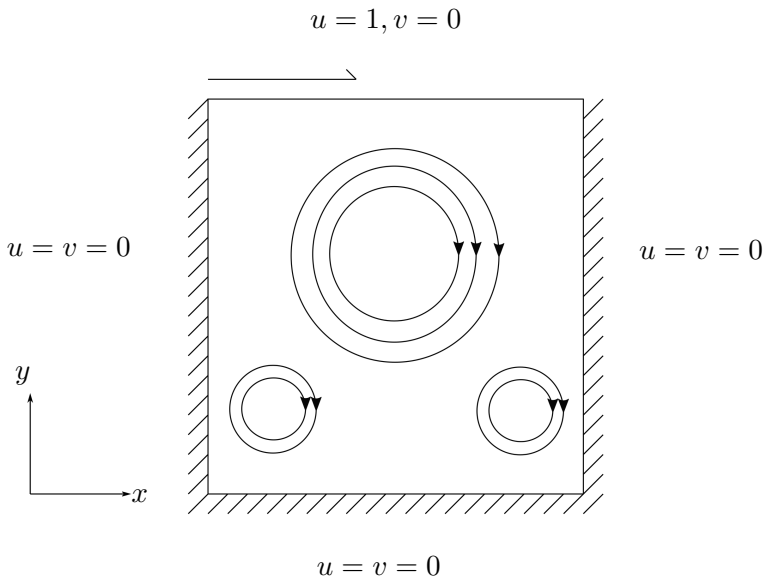

Figure 7.2: The illustration of the lid-driven cavity problem flow geometry. We impose no slip boundary conditions at the east, south, and west boundaries while we allow the lid situated at the north boundary to move horizontally to the right. Rotating vortices form in the internal flow due to wall boundary conditions and the fluid's viscous effects.

Similar to the flat-plate problem in Chapter 6, we resolve the steep velocity gradients near the walls and the top boundary by using stretched mesh grids depicted in Figure 7.3. For this purpose, we specifically use the hyperbolic tangent function since it is asymptotic on both sides of a symmetric interval as shown in Figure 7.3a. Moreover, the coordinates of the stretched domain are given by

$$x(\xi,\eta) = \frac{1}{2}\left(1 + \frac{\tanh(\alpha\xi)}{\tanh(\alpha)}\right), \quad y(\xi,\eta) = \frac{1}{2}\left(1 + \frac{\tanh(\alpha\eta)}{\tanh(\alpha)}\right), \tag{7.9}$$

where α is the stretching factor, and we set it to $\alpha = 4$. Further, $(\xi,\eta) \in [-1,1]^2$ is the isometric domain. The boundary terms in (7.6) have a similar structure for all boundaries. To cancel these indefinite terms using the boundary conditions for the lid-driven cavity problem, we use the form of penalty term matrix for the west or south boundary (Dirichlet-type) in (7.7). It can be shown by setting $u = 0$ at the north boundary that $\widehat{\mathbf{BT}}$ in (7.6) vanishes, resulting in a stable approximation.

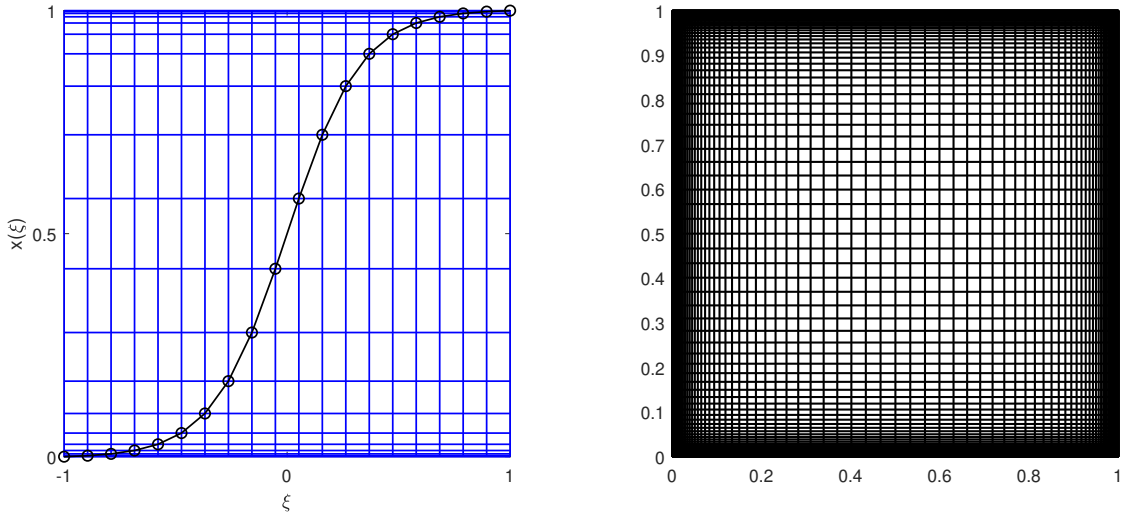

(a) Hyperbolic tangent function used to generate stretched grids

(b) Computational mesh for the lid -driven cavity problem

Figure 7.3: The computational grid for the lid-driven cavity problem is generated by hyperbolic tangent function. The mesh is saturated near the walls where the velocity gradients are the steepest.

To compute the numerical approximation of (7.1), we discretize ξ, η, and hence x, y in (7.9) with $N = M = 121$ points. As before, the spatial derivatives are computed directly on the stretched domain (Figure 7.3b) using the encapsulated SBP operators (2.49). Moreover, we employ 3rd-order SBP operators. The horizontal velocity distribution at steady state for different Reynolds numbers are shown in Figure 7.4 - 7.5. The viscous fluid was initially at rest before the uniform translation of the upper boundary. As a result of this sudden tangential motion, the fluid at the top of the cavity is moving faster compared to the internal flow. This leads to a formation of a layer that resembles the boundary layer i.e. a region that is characterized by steep velocity gradients. Moreover, its thickness decreases as Reynolds numbers increase as shown in Figure 7.4 - 7.5. We further observe the formation of rotating vorticies inside the cavity due to the wall boundary conditions and the fluid's viscous effects. Moreover, the diameter of these vortices increases with the Reynolds numbers.

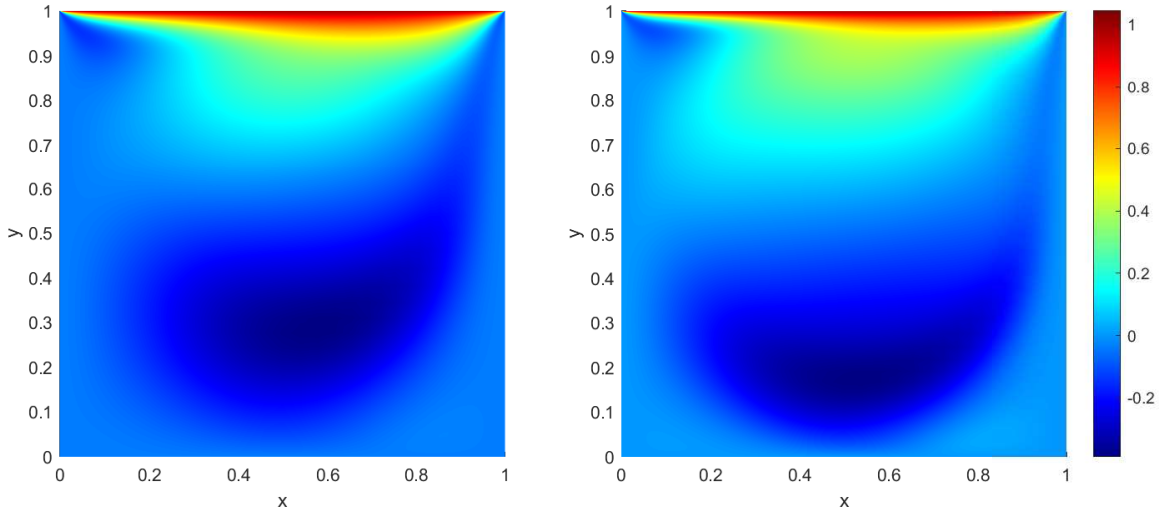

(a) Re = 400 (b) Re = 1000

Figure 7.4: Horizontal velocity distribution of the lid-driven cavity problem with Reynolds number (a) Re = 400 and (b) Re = 1000.

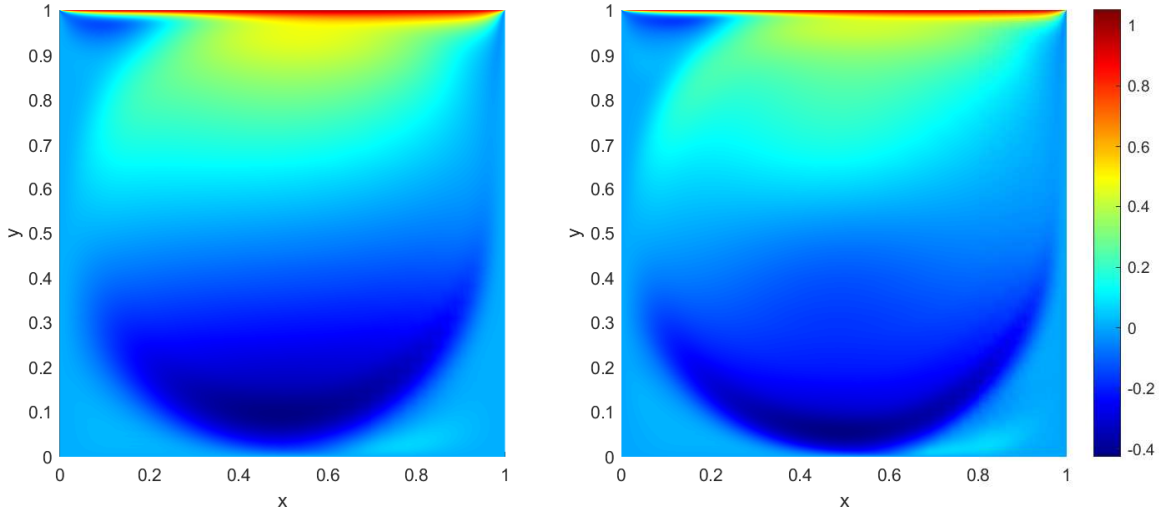

(a) Re = 3200 (b) Re = 5000

Figure 7.5: Horizontal velocity distribution of the lid-driven cavity problem with Reynolds number (a) Re = 3200 and (b) Re = 5000.

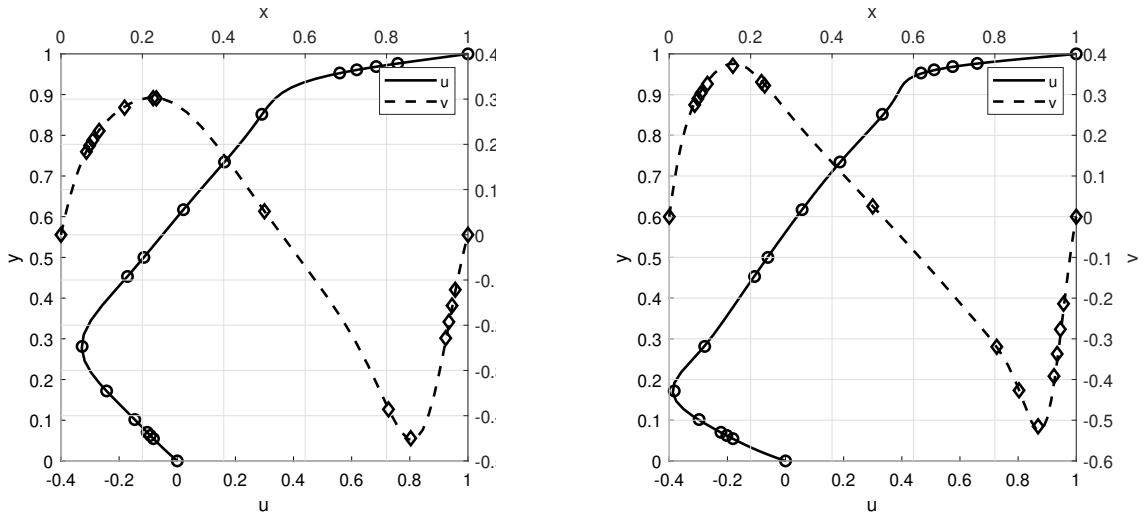

(a) Re = 400 (b) Re = 1000

Figure 7.6: The horizontal and vertical velocity profiles of the lid-driven cavity problem along x- and y-midline compared with the benchmark solution for a) Re = 400 and b) Re = 1000. Benchmark solutions are indicated by symbols.

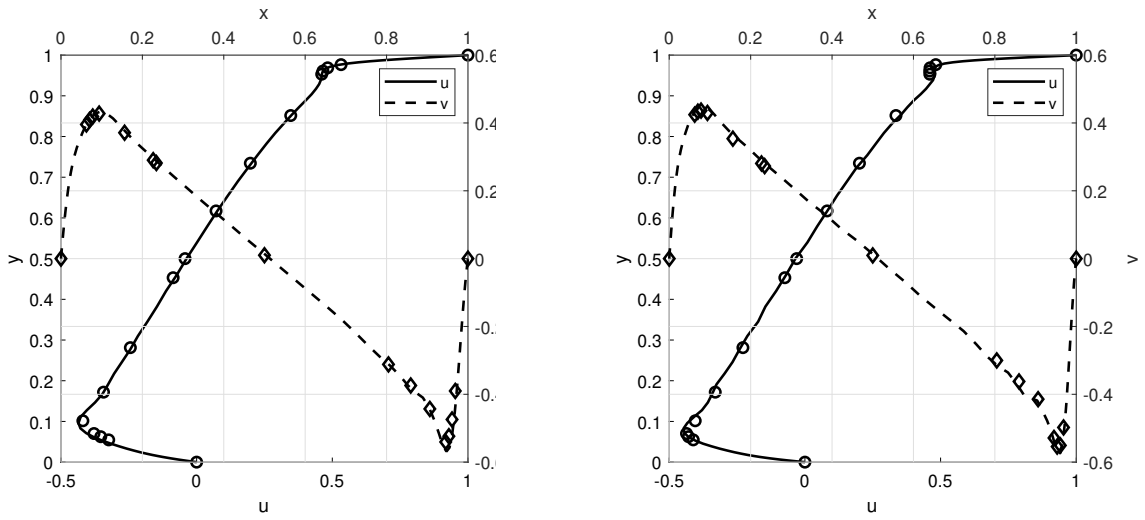

(a) Re = 3200 (b) Re = 5000

Figure 7.7: The horizontal and vertical velocity profiles of the lid-driven cavity problem along x- and y-midline compared with benchmark solution for a) Re = 3200 and b) Re = 5000. Benchmark solutions are indicated by symbols.

Next, we extract the horizontal and vertical velocity distributions along the lines $x = 0.5$ and $y = 0.5$, respectively. We compare these profiles with the benchmark solution [85] along these

lines as shown in Figure 7.6. Both solutions compare well except the slight offset for the case Re = 5000 in Figure 7.7b. This is a mesh size artefact which can be eliminated by refining the mesh for Re $\gg$ 1. The approximation (7.2) is then validated. As mentioned, the scheme has been verified for high-order accuracy in [84]. We then proceed to computing the solution of the flat-plate problem in the next section.

7.4 Flat-plate boundary layer problem

In this section, we revisit the flat-plate boundary layer problem defined on the truncated domain (see Figure 6.6a). We set the length of the domain to $l = 10$, and start the computations at $x_0 = 2$. The flow is modeled using the approximation (7.5) with boundary conditions (7.3). Similar to what we did in Section 6.2.1, we inject the Blasius similarity solution as inflow data U_∞, V_∞ at x_0. At the outflow boundaries, we set $P_\infty = 0$. In the freestream, the flow behaviour is almost inviscid and has a uniform speed. Therefore, we set the velocity gradients in (7.3) at the outflow boundaries to zero as well.

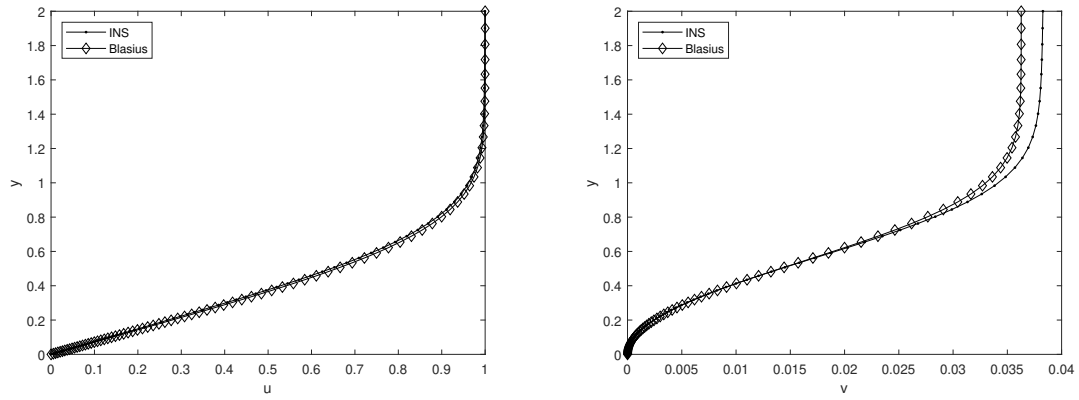

(a) (b)

Figure 7.8: The SBP-SAT approximation for the INS equations compared with Blasius solution along the line $x = 5.63$ on the truncated domain at Re = 1 000 ($\nu = 1\text{e}-02$, $\rho = 1$, $l = 10$). (a) u-velocity profile and (b) v-velocity profile.

In Figure 7.8, we compare the the computed solution with the Blaisus solution along the line $x = 5.63$ for the case Re = 1000. The horizontal velocity profile shown in Figure 7.8a compares well while there is a noticeable difference on the vertical velocity profile in Figure 7.8b. The deviation errors (computed according to (6.3)) are depicted in Figure 7.9. For both velocity profiles, the errors are prominent. Next, we consider Re = 10 000 and compare the solutions along the line $x = 5.63$. As shown in Figure 7.10, both solutions coincide. We further compare the deviation errors for this case in Figure 7.11 and they are significantly less compared to the previous case. We therefore, conclude that the INS numerical solution converges to the Blasius solution for Re $\gg$ 1. This infers that the IBL equation is a good approximation of the INS equations for Re $\gg$ 1 which corrobarate the assumptions we made in Chapter 3.

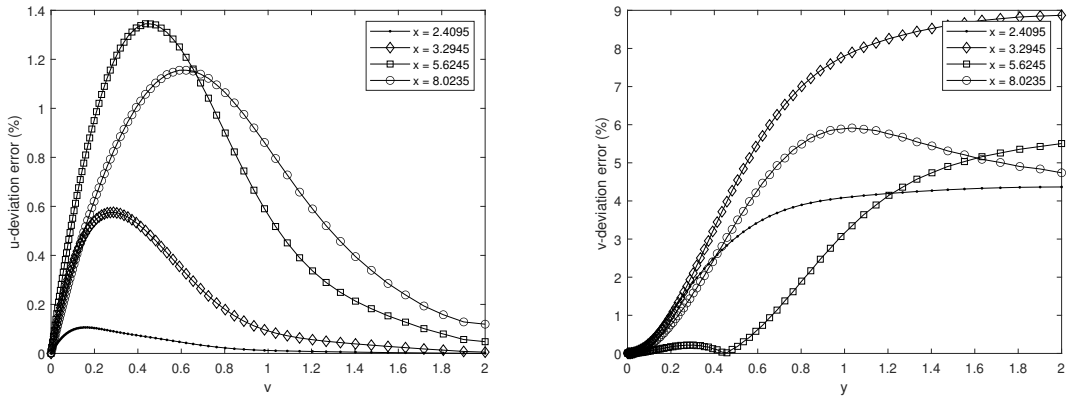

(a) (b)

Figure 7.9: The deviation errors between the SBP-SAT approximation for the INS equations and the Blasius solution at Re = 1 000 ($\nu = 1\text{e}-02$, $\rho = 1$, $l = 10$). We compare the (a) u-velocity and (b) v-velocity at various x on the truncated domain.

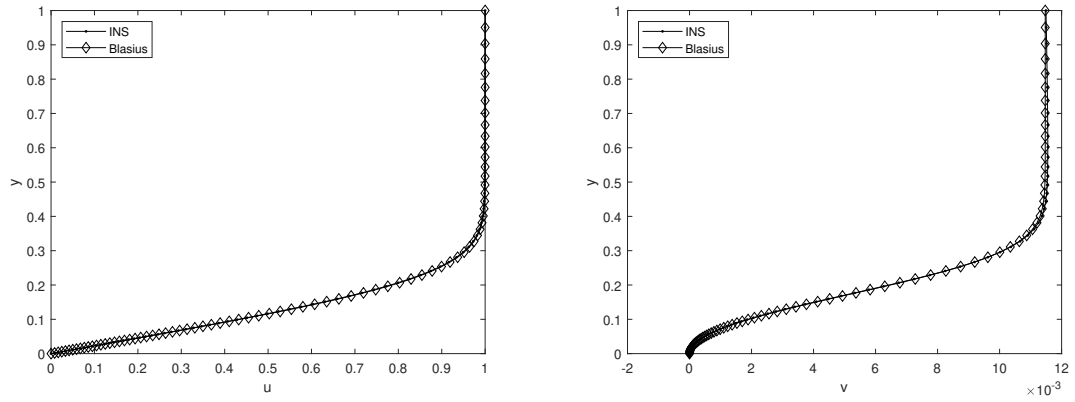

(a) (b)

Figure 7.10: The SBP-SAT approximation for the INS equations compared with Blasius solution along the line $x = 5.63$ on the truncated domain at Re = 10 000 ($\nu = 1\text{e}-03$, $\rho = 1$, $l = 10$). (a) u-velocity profile and (b) v-velocity profile.

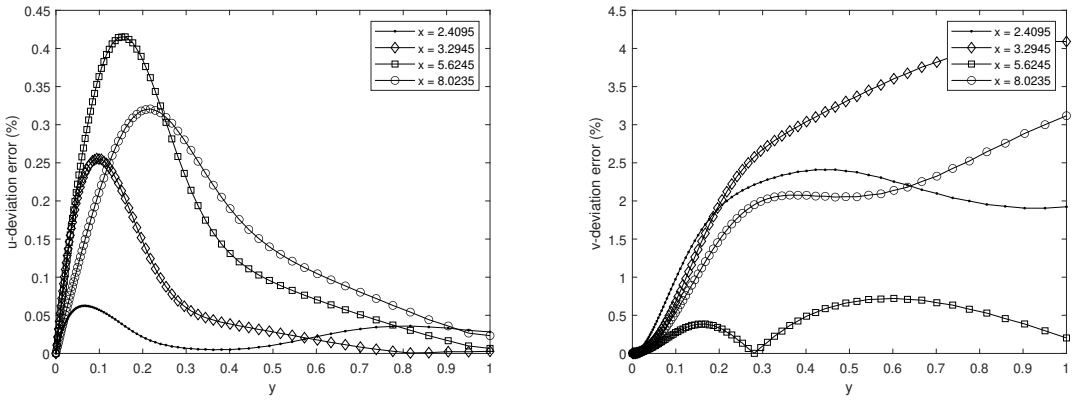

(a) (b)

Figure 7.11: The deviation errors between the SBP-SAT approximation for the INS equations and the Blasius solution at Re = 10 000 ($\nu = 1\text{e}-03$, $\rho = 1$, $l = 10$). We compare the (a) u-velocity and (b) v-velocity at various x on the truncated domain.

7.5 Closing remarks

In this chapter, the SBP-SAT approximation for the INS equations was considered. The scheme was validated using the benchmark lid-driven cavity problem. We revisited the Blasius boundary layer problem defined on the truncated domain and computed the solution using the INS numerical scheme. We then proceeded to computing the deviation errors between the computed and the Blasius solution. We observed that both solution coincide for Re $\gg 1$, thus validating the assumptions made in Chapter 3.

Chapter 8

Conclusions and Future Work

8.1 Conclusion

A stable and high-order accurate finite difference approximation for the IBL equations was developed using the SBP-SAT framework. Notably, the newly developed scheme does not use the augmented density/pressure equations for the continuity equation or upwind the convective terms. Instead, the singularities associated with the differential operator of the incompressible flow equations are eliminated using SAT boundary conditions.

The analysis in this thesis commenced with deriving the IBL equations from the INS equation at $\mathrm{Re} \gg 1$ using dimensional analysis. This was followed by formulating the continuous IBVP. By employing the energy method, the minimal number and form of boundary conditions required for boundedness and hence stability were established. This was done by analysing the indefinite boundary terms emanating from the energy method.

The flat-plate boundary layer problem (also known as the Blasius boundary layer) was considered as a model problem. Subsequently, a new set of energy stable boundary conditions specific for the laminar IBL equations were derived. Further, it was shown that both the weak and strong imposition of these boundary conditions leads to boundedness. A similar procedure was mimicked in the discrete setting to construct a stable approximation. The continuous spatial derivatives were discretized using the finite difference method on SBP form and the boundary conditions were implemented weakly using the SAT method. The discrete energy estimates that resemble the continuous counterparts were obtained, thus proving stability. Further, it was shown that the SAT boundary conditions remove the nullspace of the differential operator. This was achieved by plotting the eigenvalues of the differential operator with and without SAT boundary conditions. It was demonstrated that without including the SAT boundary conditions in the differential operator, the eigenvalues occurred on both sides of the real axis of the complex plane, which could potentially lead to non-physical oscillations (instabilities) in the solution domain. On the other hand, the inclusion of boundary conditions yielded eigenvalues with strictly positive real parts.

The scheme was verified for high-order accuracy using the method of manufactured solution, which was followed by approximating the solution of the Blasius boundary layer problem. It was further validated against the analytical solution (similarity solution). However, by computing the deviation errors between the two solutions, it was observed that the largest errors are prevalent near the plate's leading edge due to what is speculated to be the boundary data

discontinuity artefact. This was circumvented by considering the truncated domain, where the analytical solution was injected at the inflow. The reduction in the magnitude of the errors was notable.

Lastly, the SBP-SAT approximation scheme for the INS equations was considered and it was validated against the lid-driven cavity problem. By revisiting the flat-plate boundary layer problem on a truncated domain and computing the deviation errors between the computed and the similarity solution for different Reynolds numbers, it is concluded that the IBL equations are a good approximation of the INS equations.

8.2 Recommendation for Future Work

The following are suggestions for future research work which could improve some aspects of this work:

- The analysis herein assumed the homogeneous form of boundary conditions when deriving the energy estimates for the IBL equations. Recently, a general procedure for implementing nonlinear boundary conditions with nonzero data for IBVP was developed [86]. Therefore, future work must investigate the energy stability of the IBL equations with nonhomogeneous boundary conditions.

- The conflicting boundary conditions encountered in both the Blasius boundary layer (at the tip of the plate) and lid-driven cavity (at the top corners) problems must be investigated further, with a specific focus on how SAT boundary condition imposition addresses this.

- Different flow configurations that do not have conflicting boundary conditions such as the Hiemenz flow should be considered.

- A comparative study that assess the computational efficiency of the divergence augmentation methods discussed in Chapter 1 and SAT boundary condition imposition can be conducted.

- The energy stable wall modeling introduced in [87] for the INS equations can be extended to IBL equations.

Appendix A

Fully discrete formulation of the advection equation

For space-time coupled PDEs, it is possible to extend the SBP-SAT framework to the time domain [65, 66]. This is analogous to extending SBP operators to multi-dimensional space (see Section 2.7). The initial boundary condition is implemented in the same way as boundary conditions.

A fully discrete approximation of (2.24) is given by

$$\mathbf{D}_t\mathbf{w} + a\mathbf{D}_x\mathbf{w} = \sigma_t(P_t^{-1}E_0 \otimes \mathsf{I}_x)(\mathbf{w}-\mathbf{f}) + \sigma_x(\mathsf{I}_t \otimes P_x^{-1}E_0)(\mathbf{w}-\mathbf{g}), \tag{A.1}$$

where $\mathbf{D}_t \approx \partial_t$, $\mathbf{D}_x \approx \partial_x$ are the 2D SBP operators (2.31a) with $t = y$ leading to implicit time integration. The terms on the RHS of (A.1) are the weakly imposed initial and boundary conditions using the SAT method. Further, they are weighted with the coefficients σ_t and σ_x. In (2.14), we determined $\sigma_x = -a$ which led to the energy estimate for some finite time domain. Therefore, we reuse this result here and only focus on determining σ_t such that (A.1) is bounded.

Next, the discrete energy method applied to (A.1) yields

$$\mathbf{w}^\mathsf{T}(Q_t \otimes P_x)\mathbf{w} + a\mathbf{w}^\mathsf{T}(P_t \otimes Q_x)\mathbf{w} = \sigma_t(E_0 \otimes P_x)(\mathbf{w}-\mathbf{f}) - a(P_t \otimes E_0)(\mathbf{w}-\mathbf{g}). \tag{A.2}$$

By taking the transpose of (A.2), adding to itself and using the SBP property (2.31c), we obtain

$$\begin{aligned}\mathbf{w}^\mathsf{T}\left[(E_M - E_0)\otimes P_x\right]\mathbf{w} + a\mathbf{w}^\mathsf{T}\left[P_t \otimes (E_N - E_0)\right]\mathbf{w} = 2\sigma_t\mathbf{w}^\mathsf{T}(E_0 \otimes P_x)(\mathbf{w}-\mathbf{f}) \\ - 2a\mathbf{w}^\mathsf{T}(P_t \otimes E_0)(\mathbf{w}-\mathbf{g}).\end{aligned} \tag{A.3}$$

Let $||\mathbf{w}||^2_{E_M\otimes P_x} = \mathbf{w}^\mathsf{T}(E_M \otimes P_x)\mathbf{w}$ be the discrete norm at the final time, (A.3) can then be rewritten as

$$\begin{aligned}||\mathbf{w}||^2_{E_M\otimes P_x} = (1+2\sigma_t)\mathbf{w}^\mathsf{T}(E_0 \otimes P_x)\mathbf{w} - 2\sigma_t\mathbf{w}^\mathsf{T}(E_0 \otimes P_x)\mathbf{f} \\ - a\mathbf{w}^\mathsf{T}(P_t \otimes E_N)\mathbf{w} - a\mathbf{w}^\mathsf{T}(P_t \otimes E_0)\mathbf{w} + 2a\mathbf{w}^\mathsf{T}(P_t \otimes E_0)\mathbf{g}.\end{aligned} \tag{A.4}$$

Proposition 14. *The estimate* (A.4) *is bounded by data if* $\sigma_t = -1$.

Proof. Let $\sigma_t = -1$. By adding and subtracting $\mathbf{f}^\mathsf{T}(E_0\otimes P_x)\mathbf{f} + \mathbf{g}^\mathsf{T}(P_t\otimes E_0)\mathbf{g}$ to (A.4), we obtain

$$\begin{aligned}||\mathbf{w}||^2_{E_M\otimes P_x} =& -(\mathbf{w}-\mathbf{f})^\mathsf{T}(E_0 \otimes P_x)(\mathbf{w}-\mathbf{f}) - (\mathbf{w}-\mathbf{g})^\mathsf{T}(P_t \otimes E_0)(\mathbf{w}-\mathbf{g}) \\ & - a\mathbf{w}^\mathsf{T}(P_t \otimes E_N)\mathbf{w} + \mathbf{f}^\mathsf{T}(E_0 \otimes P_x)\mathbf{f} + \mathbf{g}^\mathsf{T}(P_t \otimes E_0)\mathbf{g} \\ \leq& \mathbf{f}^\mathsf{T}(E_0 \otimes P_x)\mathbf{f} + \mathbf{g}^\mathsf{T}(P_t \otimes E_0)\mathbf{g}\end{aligned} \tag{A.5}$$

□

Therefore, the numerical approximation (A.1) is stable. Lastly, (A.1) can be rewritten as a matrix problem with constant coefficient

$$\mathsf{M}\mathbf{w} = \mathbf{r}, \tag{A.6}$$

where

$$\mathsf{M} = \mathcal{D}_t + a\mathcal{D}_x + P_t^{-1}E_0 \otimes \mathsf{I}_x + a(\mathsf{I}_t \otimes P_x^{-1}E_0), \quad \mathbf{r} = (P_t^{-1}E_0 \otimes \mathsf{I}_x)\mathbf{f} + a(\mathsf{I}_t \otimes P_x^{-1}E_0)\mathbf{g}.$$

The approximation $\mathbf{w}$ at all time-levels is obtained by multiplying (A.6) on the left with M^{-1}.

Appendix B

Similarity solution

The streamwise velocity in (3.10) takes form of semi-parabolic profile as shown in Figure 3.1. These profiles are purely advected along the plate in the x-direction due to the absence of the second of derivatives in the x-directions, resulting in self-similar solution [88] (up to scalar multiplication). In this section, we present the Blasius solution method which begins by reducing (3.10) to nonlinear ordinary differential equation.

Consider the similarity variable [88]

$$\eta = y\sqrt{\frac{U_\infty}{\nu x}}, \tag{B.1}$$

which combines variables x and y. Further, consider the stream functions and the associated velocity components

$$\psi = \sqrt{\nu x U_\infty} f(\eta), \quad u = \frac{\partial \psi}{\partial y}, \quad v = -\frac{\partial \psi}{\partial x}, \tag{B.2}$$

where $f(\eta)$ is unknown. In (B.2), the stream functions satisfy the mass conservation equation (3.8c) since

$$\frac{\partial u}{\partial x} + \frac{\partial v}{\partial y} = \frac{\partial^2 \psi}{\partial x \partial y} - \frac{\partial^2 \psi}{\partial y \partial x} = 0. \tag{B.3}$$

By substituting (B.1) and (B.2) with $U_\infty = x^m$ into (3.10), we obtain

$$f'''(\eta) + \frac{1}{2}(m+1) f(\eta) f''(\eta) + m(1 - (f'(\eta))^2) = 0. \tag{B.4}$$

Next, we rewrite (B.4) as a system of nonlinear equations. Let $r_1 = f$, $r_2 = f'$, and $r_3 = f''$, then (B.4) becomes

$$\begin{aligned} \frac{dr_1}{d\eta} &= f' = r_2, \\ \frac{dr_2}{d\eta} &= f'' = r_3, \\ \frac{dr_3}{d\eta} &= f''' = -\frac{1}{2}(m+1) r_1 r_3 - m\left(1 - r_2^2\right), \end{aligned} \tag{B.5}$$

or in compact form as

$$\frac{d\mathbf{r}}{d\eta} = g(\eta, r_1, r_2, r_3),$$

where $\mathbf{r} = (r_1, r_2, r_3)$ and $g = (r_2, r_3, -\frac{1}{2}(m+1)r_1 r_3 - m(1-r_2^2)$. Equation (B.5) is a 3rd-order ODE which require at least one boundary condition for f, f', and f''. We return to (B.2) and simplify u, v as

$$u = U_\infty f'(\eta), \quad v = \frac{1}{2}\sqrt{\frac{\nu U_\infty}{x}}\left(1 - \frac{x}{U_\infty}\frac{dU_\infty}{dx}\right)\left(\eta f'(\eta) - f(\eta)\right). \tag{B.6}$$

By imposing no-slip velocity condition on the plate ($y = \eta = 0$), the first set of boundary conditions satisfying (B.7) are

$$\begin{aligned} u(x,0) &= U_\infty f'(0) = 0, \quad \Rightarrow \quad f'(0) = 0, \\ v(x,0) &= \frac{1}{2}\sqrt{\frac{\nu U_\infty}{x}}\left(1 - \frac{x}{U_\infty}\frac{dU_\infty}{dx}\right)\left(0 f'(0) - f(0)\right) = 0, \quad \Rightarrow \quad f(0) = 0. \end{aligned} \tag{B.7}$$

There is no formulation to determine $f''(0)$. We therefore overcome this by employing the nonlinear shooting method [89] which requires information about f' as $\eta \to \infty$. As alluded before, the outer flow is influenced by the freestream conditions and consequently, the flow velocity approaches the freestream velocity as $y \to \infty$. Therefore, from (B.7) we have

$$u(x, y \to \infty) = U_\infty f'(\eta \to \infty) = U_\infty \quad \Rightarrow \quad f'(\eta \to \infty) = 1. \tag{B.8}$$

Further, using nonlinear shooting method with Secant method, we compute $f''(0) = 0.46966$. Tabulated solution of (B.4) can be found in several fluid mechanics books, for example, see [88].

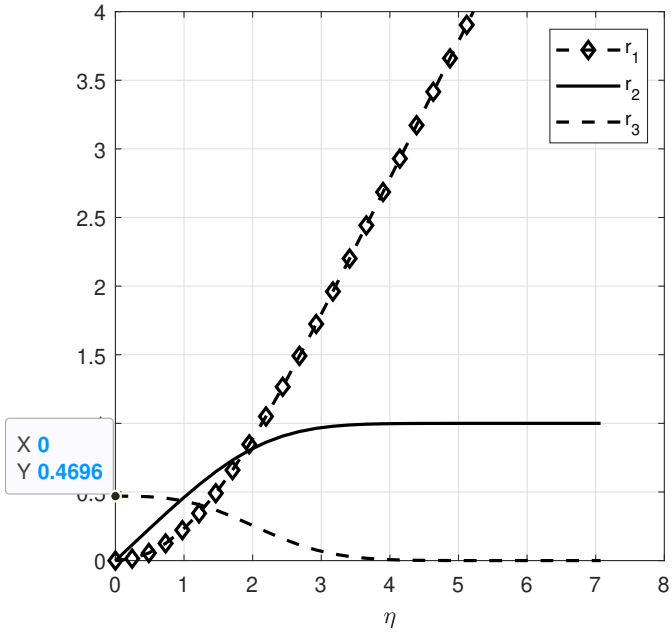

Figure B.1: Blasius similarity solution

Appendix C

Manufactured solution for the IBL equations

We show that the manufactured solution (6.1) satisfies the boundary layer equations (3.10) exactly, yielding a zero forcing function. By starting with restating the solution,

$$u = \cosh(x)\sinh(y)e^{\nu t}, \quad v = -\sinh(x)\cosh(y)e^{\nu t}, \quad p = \frac{1}{2}\sinh^2(x)e^{2\nu t}, \tag{C.1}$$

we compute the following derivatives which will be used later

$$\begin{aligned} u_t &= \nu\cosh(x)\sinh(y)e^{\nu t}, & u_x &= \sinh(x)\sinh(y)e^{\nu t}, \\ u_y &= \cosh(x)\cosh(y)e^{\nu t}, & u_{yy} &= \cosh(x)\sinh(y)e^{\nu t}, \\ v_y &= -\sinh(x)\sinh(y)e^{\nu t}, & p_x &= \sinh(x)\cosh(x)e^{2\nu t}, \\ p_y &= 0. \end{aligned} \tag{C.2}$$

We start with the x-momentum in (3.10) and substitute the derivative above to obtain

$$\begin{aligned} u_t + uu_x + vu_y + p_x - \nu u_{yy} =& \nu\cosh(x)\sinh(y)e^{\nu t} \\ &+ \sinh(x)\cosh(x)\left(\sinh^2(y) - \cosh^2(y)\right)e^{2\nu t} \\ &+ \sinh(x)\cosh(x)e^{2\nu t} - \nu\cosh(x)\sinh(y)e^{\nu t}. \end{aligned} \tag{C.3}$$

The hyperbolic trigonometry identity

$$\cosh^2(x) - \sinh(x)^2(x) = 1, \tag{C.4}$$

simplifies $\sinh^2(y) - \cosh^2(y) = -1$ in (C.3), and therefore leading to total cancellation of the terms on the RHS of (C.3). Next, we turn to the y-momentum equation in (3.10). It is trivial to show that $p_y = 0$ using (C.2). Lastly, the continuity equation in (3.10) is also satisfied since

$$u_x + v_y = \sinh(x)\sinh(y)e^{\nu t} - \sinh(x)\sinh(y)e^{\nu t} = 0. \tag{C.5}$$

Since the velocity no-slip condition is not satisfied at the south boundary because $v \neq 0$, we cannot infer that (C.1) is the exact solution of the IBVP (4.1). However, we can still source the appropriate boundary and initial data from (C.1).

Bibliography

[1] J. Marshall, A. Adcroft, C. Hill, L. Perelman, and C. Heisey, "A finite-volume, incompressible navier stokes model for, studies of the ocean on parallel computers," *Journal of Geophysical Research C: Oceans*, vol. 102, no. C3, pp. 5753–5766, 1997.

[2] L. Dedè, F. Menghini, and A. Quarteroni, "Computational fluid dynamics of blood flow in an idealized left human heart," *International Journal for Numerical Methods in Biomedical Engineering*, vol. 37, no. 11, 2021.

[3] S. Thabet and T. H. Thabit, "CFD Simulation of the Air Flow around a Car Model (Ahmed Body)," *International Journal of Scientific and Research Publications (IJSRP)*, vol. 8, no. 7, 2018.

[4] J. Douglas, J. Gasiorek, J. Swaffied, and L. Jack, "Newtonian and Non-Newtonian Fluids," in *Fluid Mechanics*, 5th ed. Pearson Education, 2005, ch. Fluids and, pp. 6–7.

[5] A. Hennink, M. Tiberga, and D. Lathouwers, "A pressure-based solver for low-Mach number flow using a discontinuous Galerkin method," *Journal of Computational Physics*, vol. 425, p. 109877, 2021. [Online]. Available: https://doi.org/10.1016/j.jcp.2020.109877

[6] C. E. Mungan, L. Huang, Z. Pan, C. Yu, and S. Chakrabarti, "The principle and applications of Bernoulli equation," 2017.

[7] J. Carlson, A. Jaffe, and A. Wiles, *Existence and Smoothness of the Navier-Stokes equation, the millennium prize problems.* Clay Mathematics Institute, Cambridge, Massachussets, 2006. [Online]. Available: http://claymath.org/millennium/Navier-Stokes-Equation

[8] M. Benzi, G. H. Golubt, and J. Liesen, "Numerical solution of saddle point problems," *Acta Numerica*, vol. 14, pp. 1–137, 2005.

[9] F. Verdugo and S. Badia, "The software design of gridap: A finite element package based on the julia jit compiler," *Computer Physics Communications*, vol. 276, p. 108341, 2022. [Online]. Available: https://www.sciencedirect.com/science/article/pii/S0010465522000595

[10] D. Massaro, A. Peplinski, R. Stanly, S. Mirzareza, V. Lupi, T. Mukha, and P. Schlatter, "A comprehensive framework to enhance numerical simulations in the spectral-element code nek5000," *Computer Physics Communications*, vol. 302, p. 109249, 2024. [Online]. Available: https://www.sciencedirect.com/science/article/pii/S0010465524001723

[11] F. H. Harlow and J. E. Welch, "Numerical Calculation of Time-Dependent Viscous Incompressible Flow of Fluid with Free Surface," *The Physics of Fluids*, vol. 8, no. 12, pp. 2182–2189, dec 1965.

[12] A. J. Chorin, "A numerical method for solving incompressible viscous flow problems," *Journal of Computational Physics*, vol. 2, no. 1, pp. 12–26, 1967.

[13] D. G. Merrick, A. G. Malan, and J. A. van Rooyen, "A novel finite volume discretization method for advection–diffusion systems on stretched meshes," *Journal of Computational Physics*, vol. 362, pp. 220–242, 2018. [Online]. Available: https://doi.org/10.1016/j.jcp.2018.02.025

[14] H.-O. KREISS and G. SCHERER, "Finite Element and Finite Difference Methods for Hyperbolic Partial Differential Equations," in *Mathematical Aspects of Finite Elements in Partial Differential Equations*. Elsevier, 1974, pp. 195–212. [Online]. Available: https://linkinghub.elsevier.com/retrieve/pii/B9780122083501500121

[15] B. Gustafsson, *High Order Difference Methods for Time Dependent PDE*, ser. Springer Series in Computational Mathematics. Berlin, Heidelberg: Springer Berlin Heidelberg, 2008, vol. 38. [Online]. Available: http://link.springer.com/10.1007/978-3-540-74993-6

[16] B. Gustafsson, H.-O. Kreiss, and J. Oliger, *Time-Dependent Problems and Difference Methods*. Hoboken, NJ, USA: John Wiley & Sons, Inc., sep 2013. [Online]. Available: http://doi.wiley.com/10.1002/9781118548448

[17] M. H. Carpenter, D. Gottlieb, and S. Abarbanel, "Time-Stable Boundary Conditions for Finite-Difference Schemes Solving Hyperbolic Systems: Methodology and Application to High-Order Compact Schemes," *Journal of Computational Physics*, vol. 111, no. 2, pp. 220–236, apr 1994. [Online]. Available: https://linkinghub.elsevier.com/retrieve/pii/S0021999184710576

[18] J. Nordström, "A Roadmap to Well Posed and Stable Problems in Computational Physics," *Journal of Scientific Computing*, vol. 71, no. 1, pp. 365–385, 2017.

[19] B. Straughan, "Energy Stability for a Solution to Partial Differential Equations," in *The Energy Method, Stability and Nonlinear Convection*. Springer, 2004, ch. Illustrati, pp. 7–18.

[20] J. Nordström and F. Laurén, "The spatial operator in the incompressible Navier–Stokes, Oseen and Stokes equations," *Computer Methods in Applied Mechanics and Engineering*, vol. 363, p. 112857, 2020. [Online]. Available: https://doi.org/10.1016/j.cma.2020.112857

[21] F. Laurén and J. Nordström, "Spectral properties of the incompressible Navier-Stokes equations," *Journal of Computational Physics*, vol. 429, p. 110019, 2021. [Online]. Available: https://doi.org/10.1016/j.jcp.2020.110019

[22] J. Manzanero, G. Rubio, D. A. Kopriva, E. Ferrer, and E. Valero, "A free-energy stable nodal discontinuous Galerkin approximation with summation-by-parts property for the Cahn-Hilliard equation," *Journal of Computational Physics*, vol. 1, p. 109072, 2019. [Online]. Available: http://arxiv.org/abs/1902.08089

[23] J. Chan, "On discretely entropy conservative and entropy stable discontinuous Galerkin methods," *Journal of Computational Physics*, vol. 362, pp. 346–374, 2018. [Online]. Available: https://doi.org/10.1016/j.jcp.2018.02.033

[24] N. K. Yamaleev and M. H. Carpenter, "A family of fourth-order entropy stable nonoscillatory spectral collocation schemes for the 1-D Navier–Stokes equations," *Journal of Computational Physics*, vol. 331, pp. 90–107, 2017. [Online]. Available: http://dx.doi.org/10.1016/j.jcp.2016.11.039

[25] R. Abgrall, J. Nordström, P. Öffner, and S. Tokareva, "Analysis of the SBP-SAT Stabilization for Finite Element Methods Part I: Linear Problems," *Journal of Scientific Computing*, vol. 85, no. 2, 2020. [Online]. Available: https://doi.org/10.1007/s10915-020-01349-z

[26] F. Ham, K. Mattsson, and G. Iaccarino, "Accurate and stable finite volume operators for unstructured flow solvers," *Center for Turbulence Research Annual Research Briefs*, pp. 243–261, 2006.

[27] J. Nordström, K. Forsberg, C. Adamsson, and P. Eliasson, "Finite volume methods, unstructured meshes and strict stability for hyperbolic problems," *Applied Numerical Mathematics*, vol. 45, no. 4, pp. 453–473, 2003.

[28] A. G. Malan, R. W. Lewis, and P. Nithiarasu, "An improved unsteady, unstructured, artificial compressibility, finite volume scheme for viscous incompressible flows: Part I. Theory and implementation," *International Journal for Numerical Methods in Engineering*, vol. 54, no. 5, pp. 695–714, 2002.

[29] A. G. Malan and O. F. Oxtoby, "An accelerated, fully-coupled, parallel 3D hybrid finite-volume fluid-structure interaction scheme," *Computer Methods in Applied Mechanics and Engineering*, vol. 253, pp. 426–438, 2013. [Online]. Available: http://dx.doi.org/10.1016/j.cma.2012.09.004

[30] J. Nordström, K. Mattsson, and C. Swanson, "Boundary conditions for a divergence free velocity–pressure formulation of the navier–stokes equations," *Journal of Computational Physics*, vol. 225, no. 1, pp. 874–890, 2007. [Online]. Available: https://www.sciencedirect.com/science/article/pii/S0021999107000083

[31] F. Laurén and J. Nordström, "Energy stable wall modeling for the Navier-Stokes equations," *Journal of Computational Physics*, vol. 457, p. 111046, 2022. [Online]. Available: https://doi.org/10.1016/j.jcp.2022.111046

[32] J. Nordström and C. La Cognata, "Energy stable boundary conditions for the nonlinear incompressible Navier–Stokes equations," *Mathematics of Computation*, vol. 88, no. 316, pp. 665–690, aug 2018. [Online]. Available: http://www.ams.org/mcom/2019-88-316/S0025-5718-2018-03375-0/

[33] J. Nordström and F. Laurén, "A stable and conservative nonlinear interface coupling for the incompressible Euler equations," *Applied Mathematics Letters*, vol. 132, p. 108171, 2022. [Online]. Available: https://doi.org/10.1016/j.aml.2022.108171

[34] J. Nordström, "A skew-symmetric energy and entropy stable formulation of the compressible Euler equations," *Journal of Computational Physics*, vol. 470, p. 111573, 2022. [Online]. Available: https://doi.org/10.1016/j.jcp.2022.111573

[35] J. Nordström and A. R. Winters, "A linear and nonlinear analysis of the shallow water equations and its impact on boundary conditions," *Journal of Computational Physics*, vol. 463, p. 111254, 2022. [Online]. Available: https://doi.org/10.1016/j.jcp.2022.111254

[36] J. Nordström and S. Ghader, "A new well-posed vorticity divergence formulation of the shallow water equations," *Ocean Modelling*, vol. 93, pp. 1–6, 2015.

[37] B. Gustafsson, "Well-posedness and Stability," in *High Order Difference Methods for Time Dependent PDE*, 1st ed. Springer, 2008, ch. Well-posed, pp. 13–66.

[38] J. Nordström, "A Roadmap to Well Posed and Stable Problems in Computational Physics," *Journal of Scientific Computing*, vol. 71, no. 1, pp. 365–385, apr 2017. [Online]. Available: http://link.springer.com/10.1007/s10915-016-0303-9

[39] ——, "Well posed problems and boundary conditions in computational fluid dynamics," *22nd AIAA Computational Fluid Dynamics Conference*, no. June, 2015.

[40] J. Nordström and M. Svärd, "Well-Posed Boundary Conditions for the Navier–Stokes Equations," *SIAM Journal on Numerical Analysis*, vol. 43, no. 3, pp. 1231–1255, jan 2005. [Online]. Available: http://epubs.siam.org/doi/10.1137/040604972

[41] B. Gustafsson, "Summation By Parts (SBP) Difference Operators," in *High Order Difference Methods for Time Dependent PDE*, 1st ed. Springer, 2008, ch. Boundary T, pp. 130–139.

[42] ——, "SBP Operators and Simultaneous Approximation Term (SAT) Methods," in *High Order Difference Methods for Time Dependent PDE*, 1st ed. Springer, 2008, ch. Boundary T, pp. 147–155.

[43] M. Svärd and J. Nordström, "Review of summation-by-parts schemes for initial-boundary-value problems," *Journal of Computational Physics*, vol. 268, pp. 17–38, 2014. [Online]. Available: http://dx.doi.org/10.1016/j.jcp.2014.02.031

[44] D. C. Del Rey Fernández, J. E. Hicken, and D. W. Zingg, "Review of summation-by-parts operators with simultaneous approximation terms for the numerical solution of partial differential equations," *Computers and Fluids*, vol. 95, pp. 171–196, 2014.

[45] J. Stewart, *Calculus Concepts and Contexts*, 3rd ed., Brooks Cole, Ed., 1995.

[46] J. Nordström and T. M. Hagstrom, "The Number of Boundary Conditions for Initial Boundary Value Problems," *SIAM Journal on Numerical Analysis*, vol. 58, no. 5, pp. 2818–2828, jan 2020. [Online]. Available: https://epubs.siam.org/doi/10.1137/20M1322571

[47] M. Svärd and S. Mishra, "Entropy stable schemes for initial-boundary-value conservation laws," *Zeitschrift fur Angewandte Mathematik und Physik*, vol. 63, no. 6, pp. 985–1003, 2012.

[48] K. Mattsson, "Boundary Procedures for Summation-by-Parts Operators," *Journal of Scientific Computing*, vol. 18, no. 1, pp. 133–153, 2003.

[49] J. Sudirham, J. Van Der Vegt, and R. Van Damme, "A study on Discontinuous Galerkin finite elements methods for elliptic problems," *Memorandum No. 1690, University of Twente, Faculty of EEMCS*, no. 1690, 2003.

[50] D. N. Arnold, F. Brezzi, B. Cockburn, and L. Donatella Marini, "Unified analysis of discontinuous Galerkin methods for elliptic problems," *SIAM Journal on Numerical Analysis*, vol. 39, no. 5, pp. 1749–1779, 2001.

[51] H.-O. KREISS and G. SCHERER, "Finite Element and Finite Difference Methods for Hyperbolic Partial Differential Equations," in *Mathematical Aspects of Finite Elements in Partial Differential Equations*. Elsevier, 1974, pp. 195–212. [Online]. Available: https://linkinghub.elsevier.com/retrieve/pii/B9780122083501500121

[52] B. Strand, "Summation by Parts for Finite Difference Approximations for d/dx," *Journal of Computational Physics*, vol. 110, no. 1, pp. 47–67, jan 1994.

[53] J. E. Hicken and D. W. Zingg, "Summation-by-parts operators and high-order quadrature," *Journal of Computational and Applied Mathematics*, vol. 237, no. 1, pp. 111–125, 2013. [Online]. Available: http://dx.doi.org/10.1016/j.cam.2012.07.015

[54] J. Gong and J. Nordström, "Interface procedures for finite difference approximations of the advectiondiffusion equation," *Journal of Computational and Applied Mathematics*, vol. 236, no. 5, pp. 602–620, 2011.

[55] R. Bodenmann, "Summation by Parts Formula for Noncentered Finite Differences Summation," *Serminar for applied mathematics, ETH Zürish, CH-8092 , Research report 95-07*, no. 95, 1995.

[56] K. Mattsson, "Diagonal-norm upwind SBP operators," *Journal of Computational Physics*, vol. 335, pp. 283–310, 2017. [Online]. Available: http://dx.doi.org/10.1016/j.jcp.2017.01.042

[57] K. Mattsson, M. Almquist, and E. van der Weide, "Boundary optimized diagonal-norm SBP operators," *Journal of Computational Physics*, vol. 374, no. June, pp. 1261–1266, 2018.

[58] R. Burden and D. Faires, "Composite Numerical Integration," in *Numerical Analysis*, 9th ed. Brooks Cole, 2010, ch. Numerical, p. 203.

[59] B. Gustafsson, "High Order Formulas on Standard Grids," in *High Order Difference Methods for Time Dependent PDE*, 1st ed. Springer, 2008, ch. Approximat, p. 81.

[60] K. Mattsson, "Diagonal-norm summation by parts operators for finite difference approximations of third and fourth derivatives," *Journal of Computational Physics*, vol. 274, pp. 432–454, oct 2014. [Online]. Available: http://dx.doi.org/10.1016/j.jcp.2014.06.027

[61] M. H. Carpenter, J. Nordström, and D. Gottlieb, "A Stable and Conservative Interface Treatment of Arbitrary Spatial Accuracy," *Journal of Computational Physics*, vol. 148, no. 2, pp. 341–365, 1999.

[62] K. Mattsson and J. Nordström, "Summation by parts operators for finite difference approximations of second derivatives," *Journal of Computational Physics*, vol. 199, no. 2, pp. 503–540, 2004.

[63] K. Mattsson, "Summation by Parts Operators for Finite Difference Approximations of Second-Derivatives with Variable Coefficients," *Journal of Scientific Computing*, vol. 51, no. 3, pp. 650–682, jun 2012. [Online]. Available: http://link.springer.com/10.1007/s10915-011-9525-z

[64] M. Svärd and J. Nordström, "On the convergence rates of energy-stable finite-difference schemes," *Journal of Computational Physics*, vol. 397, p. 108819, nov 2019. [Online]. Available: https://linkinghub.elsevier.com/retrieve/pii/S0021999119305030

[65] J. Nordström and T. Lundquist, "Summation-by-parts in time," *Journal of Computational Physics*, vol. 251, pp. 487–499, oct 2013.

[66] T. Lundquist and J. Nordström, "The SBP-SAT technique for initial value problems," *Journal of Computational Physics*, vol. 270, pp. 86–104, 2014. [Online]. Available: http://dx.doi.org/10.1016/j.jcp.2014.03.048

[67] J. Nordström and M. H. Carpenter, "High-order finite difference methods, multidimensional linear problems, and curvilinear coordinates," *Journal of Computational Physics*, vol. 173, no. 1, pp. 149–174, 2001.

[68] J. Gong and J. Nordström, "A stable and efficient hybrid scheme for viscous problems in complex geometries," *Journal of Computational Physics*, vol. 226, no. 2, pp. 1291–1309, 2007.

[69] N. A. Petersson and B. Sjögreen, "Wave propagation in anisotropic elastic materials and curvilinear coordinates using a summation-by-parts finite difference method," *Journal of Computational Physics*, vol. 299, pp. 820–841, 2015. [Online]. Available: http://dx.doi.org/10.1016/j.jcp.2015.07.023

[70] O. Ålund and J. Nordström, "Encapsulated high order difference operators on curvilinear non-conforming grids," *Journal of Computational Physics*, vol. 385, pp. 209–224, 2019.

[71] T. Lundquist, A. R. Winters, and J. Nordström, "Encapsulated generalized summation-by-parts formulations for curvilinear and non-conforming meshes," *Journal of Computational Physics*, vol. 498, no. December 2023, p. 112699, 2024. [Online]. Available: https://doi.org/10.1016/j.jcp.2023.112699

[72] J. Nordström, "Conservative finite difference formulations, variable coefficients, energy estimates and artificial dissipation," *Journal of Scientific Computing*, vol. 29, no. 3, pp. 375–404, 2006.

[73] T. C. Fisher, M. H. Carpenter, J. Nordström, N. K. Yamaleev, and C. Swanson, "Discretely conservative finite-difference formulations for nonlinear conservation laws in split form: Theory and boundary conditions," *Journal of Computational Physics*, vol. 234, no. 1, pp. 353–375, 2013. [Online]. Available: http://dx.doi.org/10.1016/j.jcp.2012.09.026

[74] F. White, "The Laminar Boundary Layer Equations," in *Viscous Fluid Flow*, 2nd ed. McGraw-Hill, 1991, ch. Laminar Bo, pp. 227–231.

[75] ——, "The Principle of Dimensional Homogeneity," in *Fluid Mechanics*, 8th ed. McGraw-Hill Education, 2016, ch. Dimensiona, pp. 260–261.

[76] J. Nordström and F. Ghasemi, "The relation between primal and dual boundary conditions for hyperbolic systems of equations," *Journal of Computational Physics*, vol. 401, p. 109032, 2020. [Online]. Available: https://doi.org/10.1016/j.jcp.2019.109032

[77] J. Nordström and F. Laurén, "The spatial operator in the incompressible Navier–Stokes, Oseen and Stokes equations," *Computer Methods in Applied Mechanics and Engineering*, vol. 363, p. 112857, 2020. [Online]. Available: https://doi.org/10.1016/j.cma.2020.112857

[78] B. Kolman, "Diagonalization of Symmetric Matrices," in *Introductory Linear Algebra with Applications*, 6th ed. Prentice Hall, 1997, ch. Eigenvalue, pp. 312–316.

[79] J. Nordström and M. Svärd, "Well-posed boundary conditions for the Navier-Stokes equations," *SIAM Journal on Numerical Analysis*, vol. 43, no. 3, pp. 1231–1255, 2005.

[80] J. Nordström, "Nonlinear Boundary Conditions for Energy and Entropy Stable Initial Boundary Value Problems in Computational Fluid Dynamics," no. January, jan 2023. [Online]. Available: http://arxiv.org/abs/2301.04568

[81] R. Burden and D. Faires, *Numerical Analysis*, 7th ed. Brooks Cole, 2001.

[82] P. J. Roache, "The Method of Manufactured Solutions for Code Verification," in *Computer Simulation Validation. Simulation Foundations, Methods and Applications*, 2019, pp. 295–318. [Online]. Available: http://link.springer.com/10.1007/978-3-319-70766-2{_}12

[83] D. Capatina, D. Capatina, D. Graebling, and D. Trujillo, "Velocity overshoot for incompressible flows past a semi-infinite flat plate," no. October, 2021.

[84] F. Laurén, "Summation-by-parts formulations for flow problems," Ph.D. dissertation, Linköping University, 2022.

[85] U. Ghia, K. Ghia, and C. Shin, "High-Re solutions for incompressible flow using the Navier-Stokes equations and a multigrid method," *Journal of Computational Physics*, vol. 48, no. 3, pp. 387–411, dec 1982. [Online]. Available: https://linkinghub.elsevier.com/retrieve/pii/0021999182900584

[86] J. Nordström, "Nonlinear boundary conditions for initial boundary value problems with applications in computational fluid dynamics," *Journal of Computational Physics*, vol. 498, no. November 2023, p. 112685, 2024. [Online]. Available: https://doi.org/10.1016/j.jcp.2023.112685

[87] F. Laurén and J. Nordström, "Energy stable wall modeling for the Navier-Stokes equations," *Journal of Computational Physics*, vol. 457, p. 111046, 2022. [Online]. Available: https://doi.org/10.1016/j.jcp.2022.111046

[88] F. White, "Similarity Solution for Steady Two-Dimensional Flow," in *Viscous Fluid Flow*. McGraw-Hill, 1991, ch. Laminar Bo, pp. 233–240.

[89] R. Burden and D. Faires, "The Shooting Method for Nonlinear Problems," in *Numerical Analysis*, 7th ed. Brooks Cole, 2001, ch. Boundary-V, pp. 653–659.